The Interaction Between Moist Convection and African Easterly Waves

James O. Russell

ABSTRACT

RUSSELL, JAMES OLIVER HARVEY. The Interaction Between Moist Convection and African Easterly Waves. (Under the direction of Anantha Aiyyer).

This dissertation addresses the relationship between African Easterly Waves (AEWs) and moist convection. AEWs are analyzed in two convection-permitting simulations and in composite averages using two reanalyses. This approach allows us to examine the mesoscale characteristics of moist convection while also investigating the synoptic-scale evolution of the AEW. Potential Vorticity (PV) and its budget in various forms, are used extensively to understand the dynamics of the AEWs.

Over land, moist convection is typically in the form of multiple Quasi-Linear Convective Systems (QLCSs) within the northerlies of the wave. Convective initiation in the northerlies occurs through a superposition of the diurnal cycle with AEW-scale forcing for moisture, ascent, and convective inhibition. The resulting QLCSs are enhanced by larger CAPE and a favorable interaction between the enhanced shear and QLCS cold pools. Over ocean, deep moist convection occurs in the trough associated with enhanced moisture and ascent. The coupling of moist convection with the AEW resembles Mapes et al. (2006) *stretched building block* theory. This manifests in deep moist convection in the northerlies and trailing upper-level stratiform convection in the trough.

The AEW can be described as a system of interconnected moist and dry waves. The dry waves propagate through advection of the background PV gradient. The moist waves propagate via moist convective diabatic PV tendencies. The system as a whole is advected by the background flow associated with the AEJ. Barotropic instability, dry baroclinic instability, and a form of moist instability occur but combined, do not account for the total growth of the AEW. The AEW is destabilized via generation of mid-level moist PV anomalies by trailing stratiform associated with the aforementioned QLCSs. This process is likened to the stratiform instability mechanism of Mapes (2000). The superposition of this moist PV anomaly with the barotropically unstable dry PV allows for the growth of the canonical mid-level southern track AEW. Finally, deep moist convection in the northerlies generates low-level moist PV anomalies which maintains the upright AEW PV column against the effects of background shear. This has implications for tropical cyclogenesis.

The Interaction Between Moist Convection and African Easterly Waves

by
James Oliver Harvey Russell

A dissertation submitted to the Graduate Faculty of
North Carolina State University
in partial fulfillment of the
requirements for the Degree of
Doctor of Philosophy

Marine, Earth, and Atmospheric Sciences

Raleigh, North Carolina
2019

APPROVED BY:

Matthew Parker	Gary M. Lackmann
Carl Schreck	William Boos

Anantha Aiyyer
Chair of Advisory Committee

ACKNOWLEDGEMENTS

Thanks first goes to my girlfriend, Gaby, for always being their whenever I needed someone throughout my degree. She has stuck by me all the way, no matter how stressed I was, and despite the sheer amount of time I spent working instead of spending time with her. I would like to thank my family back in England, especially my parents, Barbara and Nigel, for their lifetime of support getting me to this position in my life. I'd also like to thank all my friends, across the world, who have all, at some point supported me, even if it was as small as a quick conversation. My two dogs, Ghost and Ruby, have also helped me through this, simply through fluffy cuddles and always being happy.

I would like to thank my advisor, Dr. Anantha Aiyyer for his support throughout, and all the wisdom he has imparted to me through countless discussions. Special thanks goes to Dylan White for many long discussions, help with code, and moral support throughout my degree. He never failed to be there when I needed someone to discuss anything. Special thanks also goes to Dr. Gary Lackmann for much advice on the use of the WRF model. Thanks also goes to Drs. Matthew Parker, Bill Boos, and Carl Schreck who all provided useful ideas and discussion throughout my degree.

This research was sponsored by NSF through award #1433763. I thank the staff at the ECMWF, NCEP, and NASA for free access to the ERA-Interim reanalysis, CFSR, and TRMM datasets. I would like to acknowledge high-performance computing support from Cheyenne, Geyser, and Caldera (doi:10.5065/D6RX99HX) provided by NCAR's Computational and Information Systems Laboratory, sponsored by the National Science Foundation. We also acknowledge those at NCAR for the WRF-ARW model. I acknowledge the staff at NASAs Goddard Earth Sciences Data and Information Services Center (GES DISC) for free access to the TRMM dataset.

TABLE OF CONTENTS

LIST OF TABLES

LIST OF FIGURES

CHAPTER

1

INTRODUCTION

1.1 Definition

African Easterly Waves (AEWs) are synoptic-scale waves associated with the African Easterly Jet (AEJ) that move westward across the Sahel region of Africa during the West African Monsoon (WAM) season (July-September; JAS). They have wavelengths of approximately 3000-4000km and periods of 2-10 days (Burpee 1974). Their are two tracks of AEWs; a southern and northern track. The southern track is centered along 10°N while the northern track is centered along 20°N. The peak winds of southern track AEWs are typically observed at approximately 650hPa but they exhibit variability in winds, temperature, and moisture throughout a deep column in the tropopause (Kiladis et al. 2006). In contrast, variability in the northern track is limited below 800hPa. At the West African coast they undergo a transition in structure and dynamics and the two tracks typically merge. They then propagate across the Atlantic and often reach the East Pacific (Molinari et al. 1998).

1.2 Motivations

AEWs are studied for two primary reasons; 1) they are associated with variability in precipitation over the West African continent and the Atlantic (e.g. Reed et al. 1977; Laing et al. 1999; Mathon et al. 2002; Fink and Reiner 2003) and 2) they are the source of a majority of tropical cyclones (TCs) in the Atlantic (e.g. Avila and Pasch 1992). The benefits for West African countries primarily lie in the former while the significance for other countries (such as those in the Caribbean and North America) typically lie in the latter.

Many studies have shown a clear association between AEWs and precipitation or strong mesoscale convective systems (MCSs) over West Africa. Mekonnen et al. (2006) showed that the 2-6 day time scale accounted for 25-35% of the variance of convection over West Africa. Meanwhile Fink and Reiner (2003) showed that around 40% of MCSs in the WAM system are forced by AEWs. Further, Laing et al. (2012) showed that long-lived intense convective events over West Africa occur with a 2-3 day periodicity and then Laing et al. (2011) showed that the modulation of convection by larger scale disturbances is a primary source of variability. These strong convective events and large variations in precipitation affect West African communities through public safety, agriculture, and energy production, just to name a few. Thus the dynamics of AEWs are clearly of importance for West African communities.

A survey of the National Hurricane Center (NHC) TC reports (published in Russell et al. 2017) showed that over 70% of Atlantic TCs have origins related to AEWs. This fraction can be separated into a contribution where AEWs were the incipient disturbance for TCs (genesis fraction; GF) and a contribution where AEWs played a positive role in organizing moist convection but were not the main disturbance (contribution fraction; CF). Figure 1.1a shows the GF (red) and CF (blue) for all surveyed years. The average GF is 0.61 and the average contribution fraction is 0.11. This indicates that 61% of TCs form directly from AEWs, while AEWs contribute positively to the formation of a further 11% of TCs. This equates to approximately 13 TCs per season where AEWs played a positive role in their formation (Figure 1.1c). These fractions and the corresponding numbers (genesis number and contribution number; GN and CN respecitvely) are also slightly higher for hurricanes (figures 1.1b and 1.1d) and even higher for major hurricanes (Landsea 1993). In addition, non-developing easterly waves propagate into the north Pacific Ocean where they often become precursors for TCs (Molinari et al. 2000).

The effects on life, infrastructure, and property from Hurricanes spawned by AEWs is perhaps best displayed by the 2017 hurricane season. During late August and September of

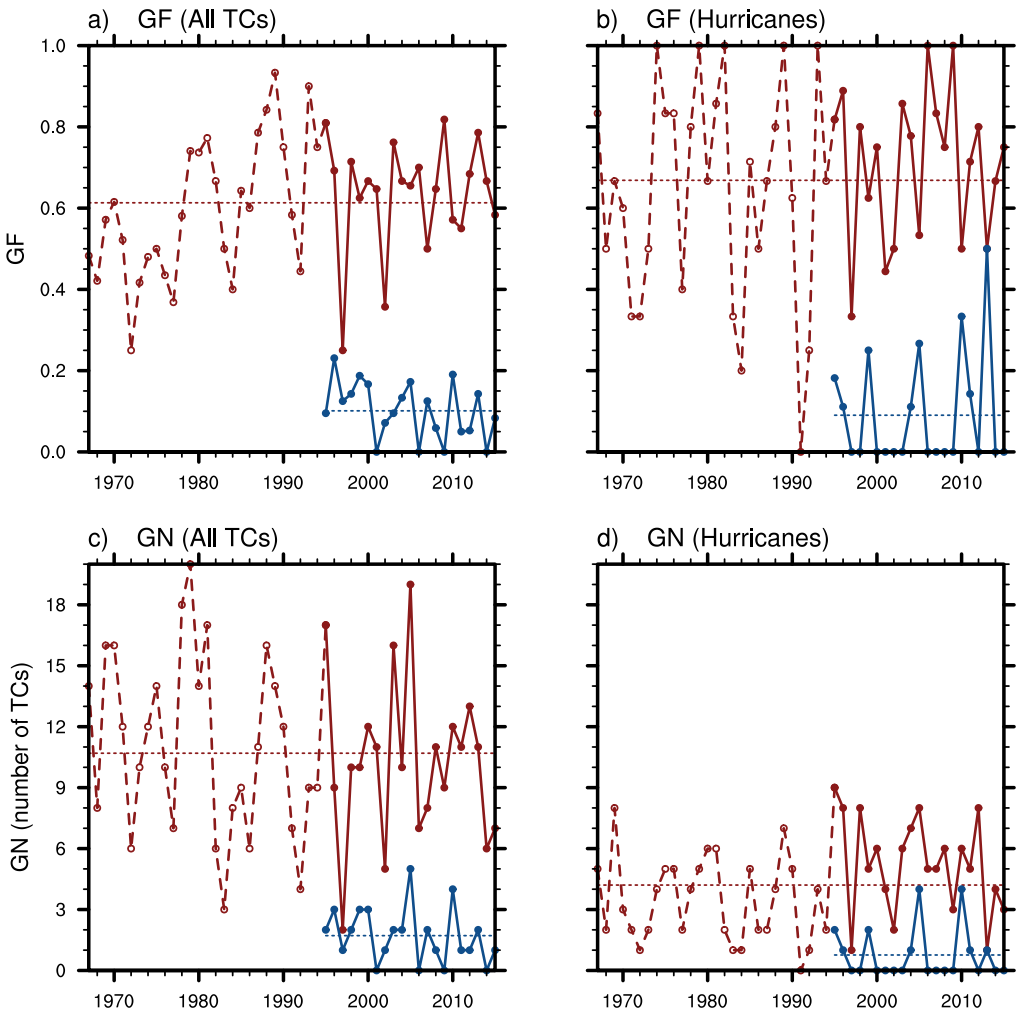

Figure 1.1: Time-series (by year) of the a) GF and CF of TCs, b) GF and CF of hurricanes, c) GN and CN of TCs, and d) GN and CN of hurricanes. Red is for GN or GF and blue is for CN and CF. Solid lines indicate time periods surveyed by our study. Dashed lines indicate time periods surveyed by Avila et al. (2000). Horizontal lines represent 1967-2015 averages.

2017, three major hurricanes (Harvey, Irma, and Maria) caused significant loss of life, as well as multi-billions of dollars in damage, across the Caribbean islands and the United States.

The first of these hurricanes, Harvey, formed from an AEW in the tropical Atlantic, tracked westward across the lesser Antilles as a tropical storm and dissipated in the southern Caribbean sea, before reforming in the Gulf of Mexico, and rapidly intensifying into a major hurricane. Harvey made landfall in southern Texas as a Category 4 Hurricane and resulted in up to 60 inches of rainfall falling around the Houston area causing unprecedented flooding. Harvey resulted in 69 fatalities and an estimated $125 billion dollars in damage (Blake and Zelinsky 2018).

Irma formed near the Cape Verde Islands from an AEW and rapidly intensified into a Category 5 hurricane, maintaining major hurricane strength for the longest of any major hurricane in the Atlantic basin. Irma caused 139 deaths across the Caribbean Islands and caused multi-billions of dollars in damage across the region, destroying up to 95% of structures on some islands (Cangialosi, Latto, and Berg 2018).

Maria formed from an AEW in the tropical Atlantic, rapidly intensified into a Category 5 hurricane, and made two landfalls in Dominica and Puerto Rico, both as a Category 5 hurricane. The official death toll in Puerto Rico is now reported to be well into the thousands including many indirect deaths as a result of the severe damage to the islands infrastructure. The total cost on all islands effected is estimated to be around $100 billion (Pasch, Penny, and Berg 2018). Combined, these three hurricanes demonstrate the severe effects on life, infrastructure, and economies that originate from AEWs.

The link between AEWs and TCs is inherently related to the moist convection associated with AEWs. Hopsch et al. (2010) analyzed composite developing and non-developing AEWs and found that the developing AEWs exhibited more convection and a stronger low-level circulation over West Africa and the Guinea highlands. This is corroborated by our work that correlates AEW EKE with GN over 36 years (1980-2015; published in Russell et al. 2017). Figure 1.2 shows the statistically significant correlations for EKE between 30°W-30°E (Figure 1.2a) and at various longitudes across Africa (Figures 1.2b-f). Notably there is no significant correlation at the peak mid-level EKE but there is significant correlation in the in the low-levels in association with the southern track AEW. Thus studies of the relationship between AEWs and moist convection are of benefit to TC forecasting. Without understanding the two-way link between AEWs and moist convection, it is extremely difficult to understand which AEWs will develop and which won't.

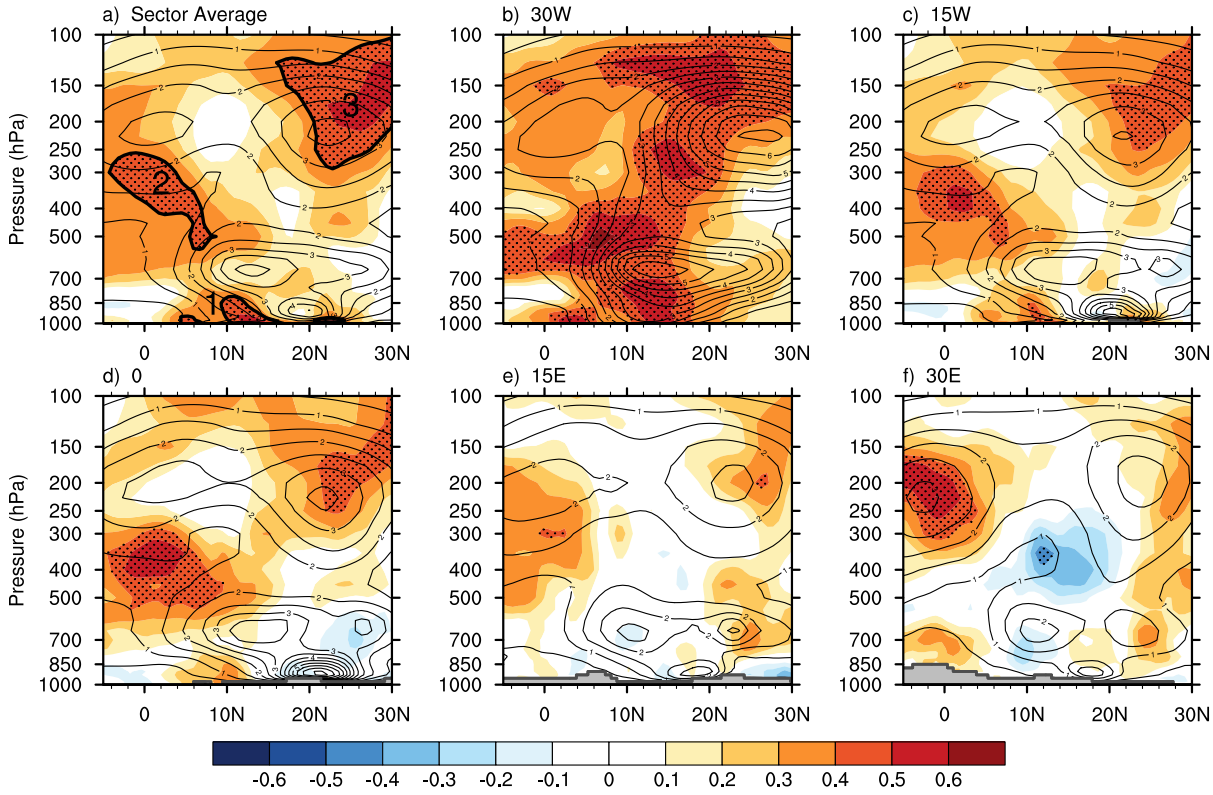

Figure 1.2: Latitude-height cross-sections of the correlation between GN and seasonal mean EKE (filled) for a) 30°W-30°E, b) 30°W, c) 15°W, d) 0°, e) 15°E, and f) 30°E. Contours represent the seasonal mean EKE (J/kg) and stippling represents statistical significance of 95% for the correlations. Outlined areas with numbers represent specific statistically significant areas of correlation discussed in the text.

1.3 Dry Dynamics of AEWs

The focus of early research on the growth and maintenance of AEWs was primarily on the dynamical instability of the AEJ (Carlson 1969; Burpee 1974; Reed et al. 1977; Norquist et al. 1977). These studies suggested that AEWs grow through the baroclinic and barotropic extraction of energy from the AEJ. This conclusion was based on the fact that the background state over West Africa met the conditions for such instabilities presented by Charney and Stern (1962); a reversal in the meridional gradient of background potential vorticity (PV). These and later studies (e.g. Thorncroft and Hoskins 1994) essentially described AEWs as growing Rossby waves (RWs), with the AEJ as the source of energy and the waveguide.

In dry idealized simulations with a basic state characterized by a simple easterly jet, Thorncroft and Hoskins (1994) produced waves that resembled the synoptic features observed in AEWs. The major difference was in the vertical velocity that was too weak and produced an unrealistic pattern. In this system, they showed that the dynamics are dominated by the interaction between waves on the positive and negative potential vorticity (PV) gradients associated with the background flow. The conclusion of Thorncroft and Hoskins (1994) was consistent with Burpee (1972), who first recognized the potential for mixed barotropic-baroclinic instability of the AEJ from observations.

Since then, a number of studies have shown that dry barotropic and baroclinic instabilities of the AEJ are insufficient to explain the growth and maintenance of AEWs (e.g. Hsieh and Cook 2005; Hall et al. 2006). In particular Hall et al. (2006) showed that given a modest amount of damping with an idealized AEJ, the normal modes of the AEJ were effectively neutralized. This suggests that some other process must exist that allows for the maintenance and growth of AEWs as observed.

1.4 Influence of AEWs on Convection

A strong relationship between AEWs and convection was detailed by Payne and McGarry (1977). Later, Duvel (1990) used Meteosat data and ECMWF analyses to show that the strongest deep convection occurs at, and ahead of, the wave trough over land, before transitioning into the trough over the East Atlantic. He also noted that convection coincided with synoptic scale divergence in the upper-levels and variations in the thermodynamic profile on scales similar to the AEW. This work hinted at the possibility that AEWs produce forcing for ascent resulting in moist convection.

In section 1.2 we discussed a number of studies that document the link between moist

convection and AEWs. These studies highlight the possibility for convection to have strong interactions with AEWs. Many other studies have also associated convection with AEWs (e.g. Diedhiou et al. 1999; Gu et al. 2004). These studies noted that convection primarily occurs in the northerlies and trough over land, and the trough over ocean, as in Duvel (1990). Combined, these studies present clear evidence that AEWs have an organizing effect on convection.

However, this organizing effect very rarely produces moist convection that is linearly coupled to the AEW. Diedhiou et al. (1999) and Gu et al. (2004), showed that convection often moves through the wave as it crosses west Africa. Further Laing et al. (2008) showed that the distribution of propagation speeds of observed cold cloud episodes (e.g. MCSs) does not well match the phase speeds of AEWs tracked in the National Center for Environmental Prediction (NCEP) Global Final Analysis. Further, Cifelli et al. (2010) used data from the AMMA and NAMMA field campaigns to examine one particular AEW during 2006. They found that convection was not significantly impacted with the passage of this AEW. These studies highlight the fact that the relationship between AEWs and MCSs is complex.

Thorncroft and Hoskins (1994) showed that in an idealized adiabatic wave, there are clear ascent and descent regions. Later, Kiladis et al. (2006) used modified Q-vectors in composite ERA-40 reanalysis waves to show that AEWs produce adiabatic forcing for ascent ahead of the trough. While the Quasi-geostrophic (QG) forcing for ascent broadly coincided with fields of vertical motion and outgoing long wave radiation (OLR), there was a slight phase lag between the forcing for ascent and the response. Furthermore, they found that the QG forcing was not uniformly successful in accounting for the vertical motion and precipitation in the wave.

The influence of AEWs on convection is perhaps examined in most detail by Janiga and Thorncroft (2016) who used TRMM and the ERA-Interim reanalysis. They also found that over land, the northerlies are characterized by enhanced adiabatic forcing for ascent while the southerlies are characterized by forcing for descent. Janiga and Thorncroft (2016) also found that over land, there is enhanced shear and convective available potential energy (CAPE) between the northerlies and the ridge with reduced CAPE and shear between the trough and southerlies. Finally, Tomassini et al. (2017) presented another method through which AEWs may enhance convection. This study showed that there is convergence of moisture ahead of the AEW trough in the low-to-mid levels of the atmosphere. They theorized that this is then the main forcing for convection in the AEW. The overall influence of AEWs on convection is summarized nicely by Janiga and Thorncroft (2016) (shown in Figure 1.3).

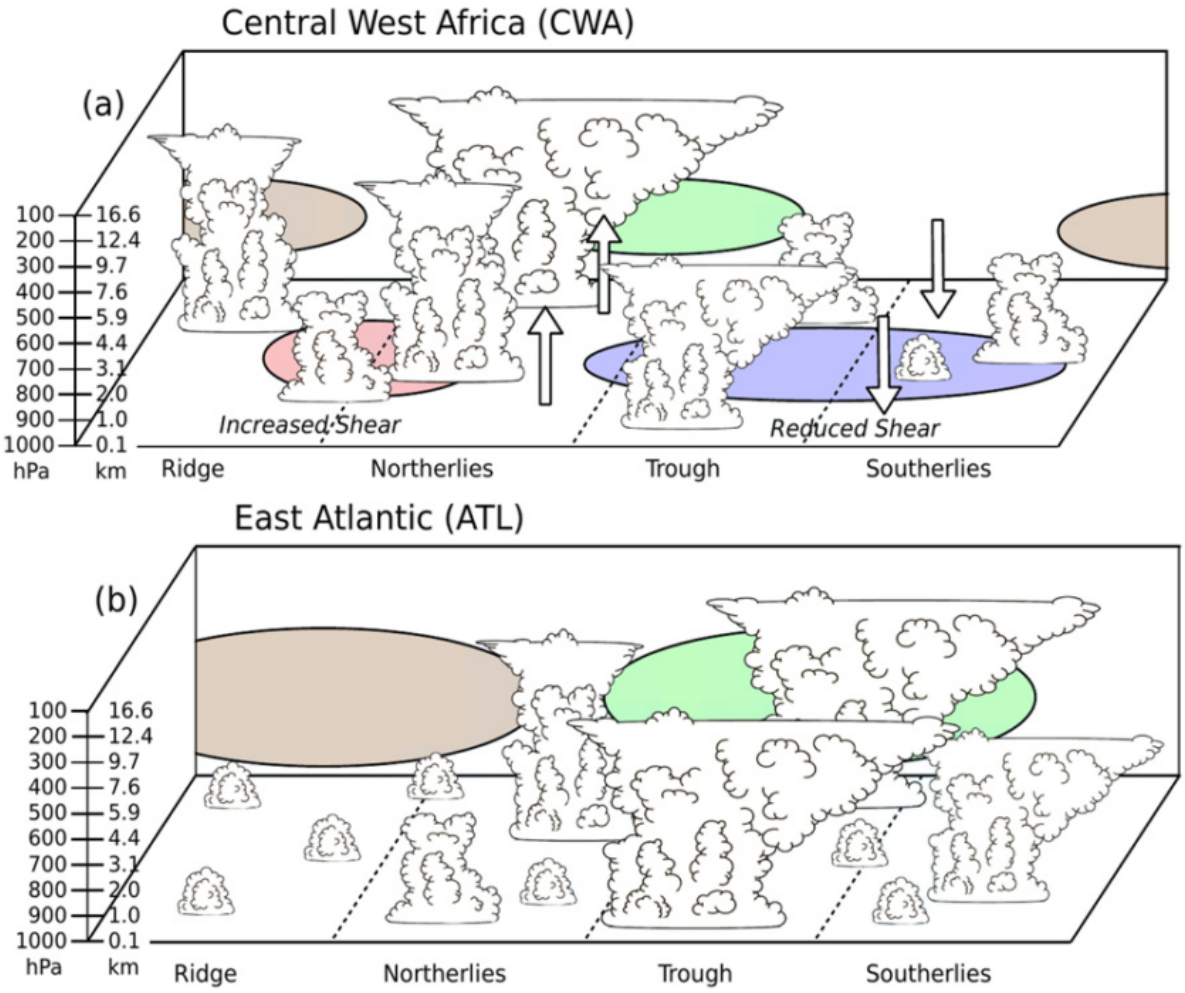

FIG. 17. Schematic of the AEW–convection relationship over (a) central West Africa (CWA) and (b) the east Atlantic (ATL). This schematic presents an exaggerated view of the amount and type of convection in each phase. Green (brown) circles indicate positive (negative) moisture anomalies. Red (blue) circles indicate regions of warm (cool) low-level temperatures and increased (reduced) CAPE. Arrows indicate the adiabatic forcing for ascent or descent.

Figure 1.3: Janiga and Thorncroft (2016) Figure 17.

1.5 Influence of Convection on AEWs

Norquist et al. (1977) suggested that latent heating produced by convection can be a dominant factor for the growth and maintenance of AEWs over West Africa. Using a vorticity budget for a composite AEW from the GATE experiment, Shapiro (1978) found that without a simple parameterization for cumulus the vorticity source in AEWs may be underrepresented. Thorncroft and Hoskins (1994) investigated the role of diabatic effects in a linear model of AEWs. With a simple parameterization of latent heat release, the most unstable modes became less dominated by barotropic energy conversions and the growth rates were increased. Further, the vertical velocities were found to better match observed patterns and magnitudes. They concluded that the role of latent heating is important in increasing the baroclinic energy conversions, and also in determining the synoptic structure. These studies were the first to show that convection was important for the growth and maintenance of AEWs.

However, the exact mechanism through which convection enhances AEWs is still a debated topic. An analysis of one simulated AEW by Berry and Thorncroft (2005) indicated that convection has notable effects on the AEW at multiple stages during its growth and maintenance. They argued that PV generated by convection coupled with the AEW supports the growth of the AEW via baroclinic processes. Then, convection near the west African coast maintains the AEW after dry baroclinic processes have weakened. More recently, Berry and Thorncroft (2012) produced an ensemble of simulations to demonstrate that convection is important for the maintenance of AEWs. An energy budget that computed diabatic (convective) and adiabatic (instability) forcing, concluded that the two were of the same order of magnitude. Comparison of the results with a dry simulation (convective parameterization switched off) showed that the AEW weakened substantially. These results are consistent with those of Schwendike and Jones (2010), Janiga and Thorncroft (2014), and Poan et al. (2014) who showed that convection acts to enhance vorticity, PV, and momentum respectively in the low-to-mid levels over West Africa. All in all, these studies support the idea that convection enhances low-to-mid level rotation through moist baroclinic processes.

1.6 Convection and Synoptic Systems

Convection has been shown to interact with other synoptic scale disturbances to produce growth of the overall system. Some examples include Diabatic Rossby Waves (DRWs) and convectively coupled equatorial waves (CCEWs). Here we will review the mechanisms

involved in DRWs and CCEWs, with a view to applying these to AEWs later.

A DRW is a wave for which the diabatic (convective) generation of low-level PV, governs the evolution in a manner similar to advection of PV in Rossby waves (e.g. Raymond and Jiang 1990). A majority of research (Parker and Thorpe 1995; Moore and Montgomery 2005) on DRWs has focused on the mid-latitudes and the genesis and maintenance of Diabatic Rossby Vortices (DRVs) (a closed circulation counterpart to the DRW). As defined by Shih (2012), a DRV is a diabatically dominated, moist baroclinic disturbance, in the absence of discernible upper tropospheric forcing. A depiction of the DRV in mid-latitude mean westerlies is shown in Figure 1.4. The specific propagation mechanism can be described as follows. A positive PV anomaly generates a balanced circulation with southerlies to its east. In a moist-baroclinic zone with isentropes sloping upward to the north, these southerlies generate dry adiabatic ascent which then triggers moist convection. The associated latent heating generates a low-level positive PV anomaly to the east of the previous PV anomaly. This propagates the system eastward.

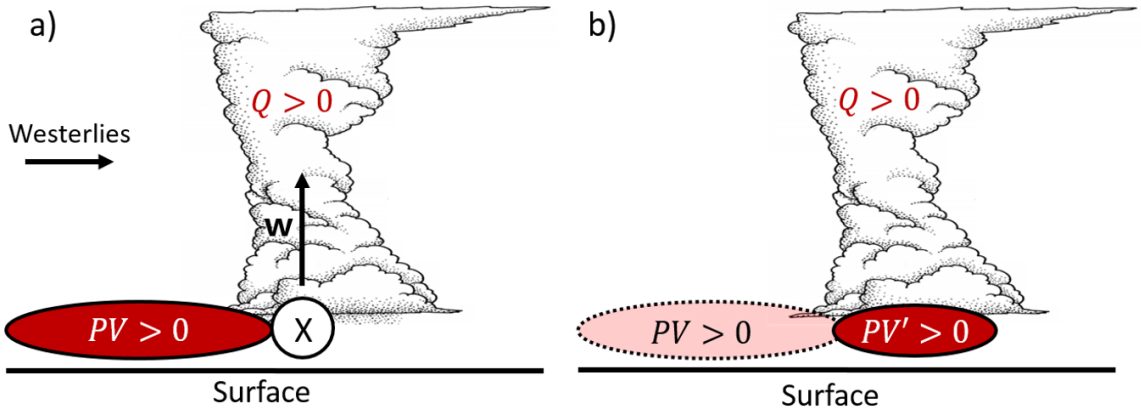

Figure 1.4: A schematic of a DRV in mean westerlies adapted from Parker and Thorpe (1995). a) depicts a current time and b) depicts a later time. Current positive PV (solid red circles), past positive PV (dashed pink circle), southerlies (X), ascent (w), and diabatic heating (Q) are shown in association with the cloud distribution.

The destabilization of the DRW in the presence of mixed baroclinic-barotropic instability is a more complex problem. De Vries et al. (2009) and Cohen and Boos (2016) summarized this process and provided a conceptual framework to understand moist baroclinic instability from the perspective of phase locked counter propagating waves. Figure 1.5, taken from Cohen and Boos (2016), depicts a four layer model with upper and lower dry and moist

layers. Interactions between the PV anomalies on various upper and lower layers produce baroclinic instability when they exhibit a favorable upshear tilt. It is of interest to adapt this framework to the case of the mid-level AEJ and the attendant dry and moist components associated with the AEW.

A number of studies have speculated that the process through which AEWs interact with convection is representative of a DRW (e.g. Moore and Montgomery 2005; Berry and Thorncroft 2005, 2012; Tomassini et al. 2017). These studies have, however, not provided any analysis to support their claim. It is possible that the DRW model is applicable to AEWs since part of their life cycle is spent in a region of relatively large (for the tropics) meridional temperature gradient, they induce adiabatic ascent ahead of the trough, and that a balanced response to moist convection is possible at the latitude of the AEWs.

Another model for coupling of synoptic scale waves to convection is stratiform instability (Mapes 2000). This is typically used for convectively coupled equatorial waves but some aspects may be of some relevance for AEWs. The schematic in Figure 1.6 illustrates a highly simplified version of the process for an eastward propagating wave, illustrating some of the properties that may be pertinent to AEWs. As the wave propagates eastward it's thermodynamic structure enhances CAPE, priming the thermodynamic environment in favor of convection. As congestus builds, developing convection slowly removes the convective inhibition (CIN) (Figure 1.6b). Deep convection then forms once CIN has been removed and the first phase of the wave has passed. This leaves a region of trailing stratiform cloud in the next phase of the wave (Figure 1.6c). Finally, the second-baroclinic structure of heating, as a result of the stratiform cloud, heats the upper-levels and cools the lower-levels. This further enhances the thermodynamic structure of the wave (Figure 1.6d).

Kuang (2008) presented a modified version of the stratiform instability mechanism that couples moist convection to the wave through moisture convergence, rather than through the removal of CIN. This is referred to as the moisture-stratiform instability. The mechanism for enhancement of the wave by convection (i.e. heating and cooling from stratiform cloud) remains the same here.

1.7 Open Questions and Theories

In this section I will present the open questions on the one-directional effects and two-directional interaction between the AEW and convection. I will also present theories based on prior literature (documented in the previous section) that will be investigated in order

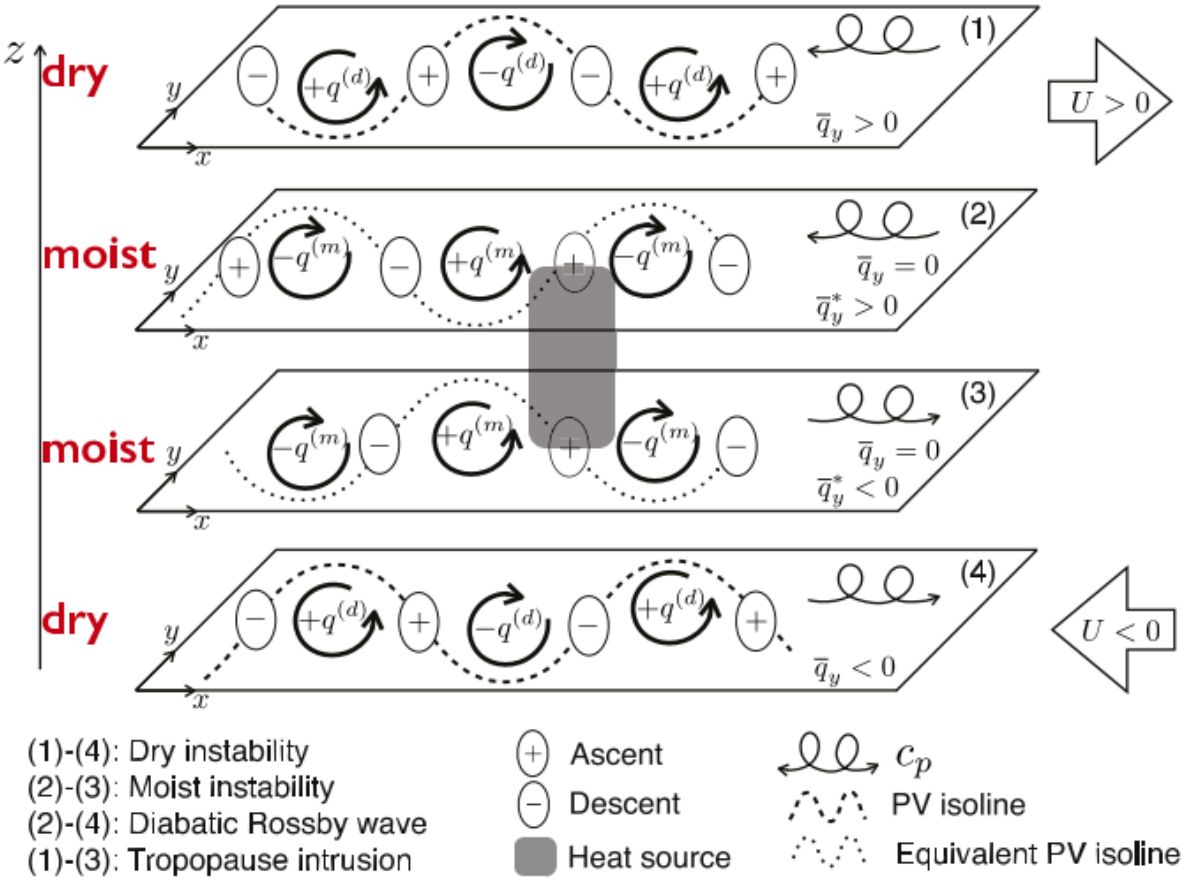

FIG. 3. Schematic of dry and moist PV components in counterpropagating Rossby waves. Four vertically stacked, horizontal layers on an f plane are shown in a basic state with positive vertical shear $\overline{u}_z > 0$. In each layer a wave train of cyclones and anticyclones is shown with the corresponding perturbation PV (dashed and dotted lines are isolines of total dry and moist PV, respectively). Perturbations are assumed to be normal modes and to be accompanied by vertical motions in accordance with the quasigeostrophic omega equation (ellipses enclosing positive and negative signs represent ascent and descent, respectively). Moist convective diabatic heating is shown as a vertical gray rectangle. The direction of zonal propagation relative to the basic-state flow is shown by the curly arrows. The four possible unstable interactions are noted in the bottom left.

Figure 1.5: Cohen and Boos (2016) Figure 3.

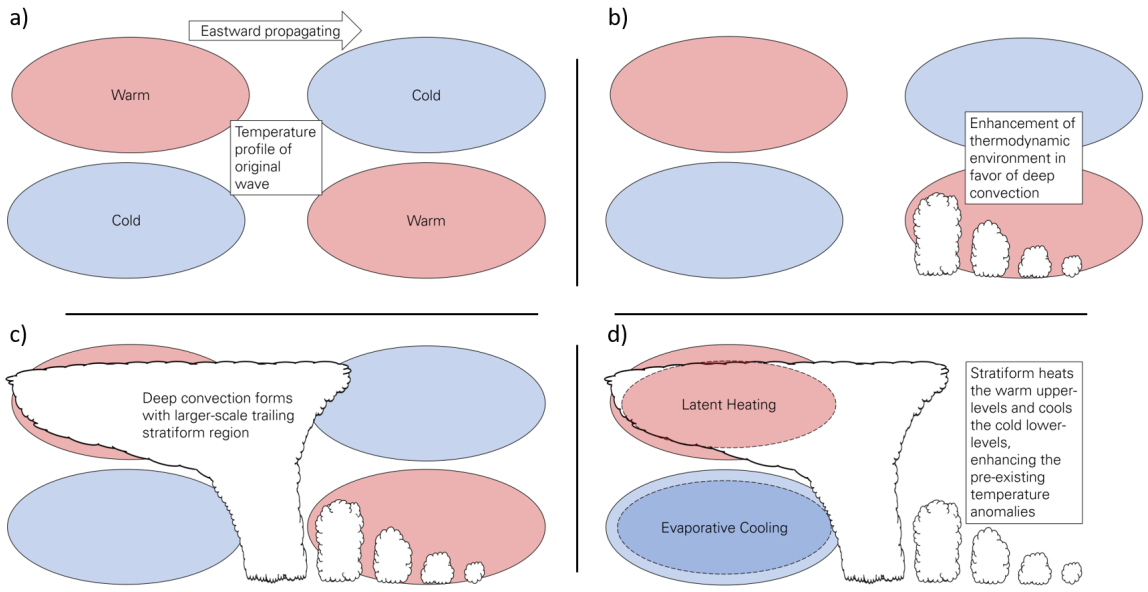

Figure 1.6: Vertical cross-sections (x-z) illustrating key properties of the stratiform instability process.

to answer these questions. Each section will conclude by summarizing the questions I aim to answer.

1.7.1 Influence of AEWs on Convection

As noted earlier in this chapter, and highlighted by the studies of Diedhiou et al. (1999), Gu et al. (2004), Laing et al. (2008), and Cifelli et al. (2010) moist convection is rarely linearly coupled to the AEW. Thus a first step toward understanding their interrelationship is better characterizing the moist convection present within the AEW envelope. We therefore need to establish the overall structure, motion, and dynamics of moist convection. This will include understanding how it is initiated and maintained. Once moist convection has been characterized, it is then possible to relate it to the AEW and interpret how factors influenced by the AEW, may enhance moist convection.

There are essentially four processes (adiabatic lift, thermodynamic enhancement, enhancement via shear, and moisture convergence) that have previously been documented and should be considered when examining how the AEW modifies convection. Until recent studies by Janiga and Thorncroft (2016) and Tomassini et al. (2017) the only one of these processes that had been considered was that of adiabatic forcing for ascent. A complete un-

derstanding of how AEWs force moist convection needs to examine whether the initiation of moist convection such as MCSs, can be directly attributed to dry adiabatic ascent.

Exactly why there is a variation in CAPE and moisture associated with the AEW is unclear. Two possibilities arise. The first is that the AEW directly enhances CAPE and moisture. These could occur through advection of warm and moist surface air. In such a case, the temperature and moisture distribution of the background environment plays an important role. The second is that this variation in CAPE and/or moisture is a biproduct of the coupled convection. For example, CAPE is reduced as it is consumed by convection. Thus, in the wake of long-lived MCSs (i.e. those that last longer than a diurnal cycle) it may take a couple of days for CAPE to recover. Long-lived MCSs are often observed coincident with the AEW (Laing et al. 2008). To gain a complete picture of how the thermodynamic and moisture environments of the AEW affect moist convection we need to understand whether these are a product of the AEW or the convection.

In summary we will attempt to address the following questions with regard to the role AEWs play in modifying convection:

1. What are the characteristics of moist convection within the AEW envelope and how do they relate to the AEW?

2. Are the thermodynamics and moisture a result of the AEW or a biproduct of the convection?

3. Which factors influenced by the AEW (e.g. moisture convergence, thermodynamic priming and kinematic priming of the environment, and adiabatic forcing for ascent) are important in initiating and maintaining moist convection?

1.7.2 Influence of Convection on AEWs

Examinations of the role that convection plays in modifying the AEW have been focused on understanding how convection may enhance the energetics, vorticity, or PV in the AEW. PV is arguably the best variable through which to quantify this since a source of PV can be directly attributed to diabatic effects. Despite this, it's not been explicitly shown that PV is generated by moist processes in and ahead of the AEW at mid-levels. Most studies have implied this generation through other means. The theory put forward by a variety of studies (e.g. Berry and Thorncroft 2005, 2012; Janiga and Thorncroft 2013) is that the PV tendency from latent heating will lead the AEW to the west. This theory will be directly tested here.

When considering PV sources, deep convection typically enhances PV in the low-levels where the vertical latent heating gradient is strongest. Thus a question that remains is how convection enhances PV in the mid-levels. Janiga and Thorncroft (2016) showed that there are elevated stratiform cloud fractions in the trough of AEWs over West Africa and Janiga and Thorncroft (2013) showed that there is mid-level generation of PV. A number of studies have shown that MCSs are often associated with mesoscale convective vortices (MCVs) in the mid-levels (Velasco and Fritsch 1987; Menard and Fritsch 1989; Laing and Fritsch 1993; Skamarock et al. 1994). Fritsch et al. (1994) and Davis and Weisman (1994) showed that MCVs occur due to the mid-level generation of PV by stratiform cloud regions associated with MCSs. Our expectation is therefore that it is the statiform cloud, not the deep convection, that leads to enhancement of the AEW PV anomaly. However, a direct link between stratiform cloud, the PV generation associated with MCVs, and the maintenance and propagation of AEWs is yet to be shown.

Further, Berry and Thorncroft (2012) found that adiabatic and diabatic sources of energy in AEWs were comparable. This quantitative difference can arguably be better understood using PV. To understand the importance of moist convective processes, PV tendencies as a result of latent heating need to be put into context relative to other diabatic (i.e. radiative and surface processes), adiabatic, and frictional sources. Here, we expect that the sources of PV from advection and latent heating will be comparable in magnitude.

Finally, very few studies have examined AEWs in simulations where moist convection is limited to various degrees. Such an experiment may help explain how convection modifies AEWs. If an AEW can be maintained in some form after the convection has ceased then the wave is not completely reliant on diabatic processes. Thorncroft and Hoskins (1994) examined waves on an idealized AEJ with and without a simple convective parameterization. The biggest difference they found was that the vertical velocity pattern varied between the two. Meanwhile, Berry and Thorncroft (2012) used full physics simulations with the Weather Research and Forecasting model (WRF) to examine an AEW with and without parameterized convection. They found that the AEWs mid-level signature weakened considerably after the convective parameterization was switched off. However, they only focused on the mid-level AEW signature and neglected to examine the entire wave structure. These studies present contrasting views and such studies need to be analyzed in detail. We hypothesize that the AEW can be maintained by adiabatic processes but will have weaker low-to-mid level perturbations.

In summary we will attempt to address the following questions with regard to the role convection plays in modifying AEWs:

1. What is the structure of diabatic PV tendencies relative to the AEW? And how do they compare to adiabatic PV tendencies in an AEW?

2. How does the structure of convection lead to mid-level rotation on the scale of the AEW?

3. Does an AEW exist without convection present? And if so, what is the difference in AEW structure and why?

1.7.3 A Complete Model for AEW-Convection Interaction

Describing the AEW-convection interaction with a detailed conceptual model is the ultimate goal of this study. To present this model, the answers to the previous questions will need to be combined with current understanding and examples of other convectively coupled waves.

As previously discussed, the DRW mechanism has been suggested as one such mechanism for the AEW-convection interaction. While AEWs exist in a similar moist baroclinic environment, the DRW mechanism must be adapted for a mid-level wave in easterly shear. There are a number of issues here. The first two are the mechanism coupling convection to AEWs and the mechanism generating PV in the mid-levels. Both issues have been discussed in the previous sections.

Another major issue with the applicability of the DRW mechanism to AEWs is the scale separation between convection and AEWs. How are PV anomalies on the scale of the AEW generated by deep convection? In the mid-latitudes, DRWs are typically smaller in scale than their dry counterparts, primarily because they are driven by smaller scale convective processes. However, AEWs are much larger than individual convective systems over West Africa. Typically over West Africa there is more than one convective system present at any given time. It's therefore possible that the combination of all the convective systems ahead of the trough at any given time generates a PV anomaly on the scale of the AEW. This, however, is yet to be shown.

In this study, we expect that the dry dynamics of easterly waves are modified by a process akin to that occurring in DRWs. Our hypothesis is that the generation of new PV anomalies by convection combines with dry dynamics to produce the observed structure of AEWs. We also expect that there are transitions during AEW life cycles between a primarily dry AEW and an AEW that can be described as more of a DRW. This idea may be extended further to include DRVs when the AEW becomes a closed circulation, and then hurricanes when

convection transitions from sheared MCSs over Africa to hot towers in the trough over the Atlantic.

Stratiform instability is a mechanism for the coupling of convection to, and subsequent enhancement of convectively coupled equatorial waves. AEWs are typically likened more to QG Rossby waves evolving in a baroclinic atmosphere. Thus stratiform instability is not a mechanism through which we could completely explain the AEW-convection interaction. However, as can be seen on examination of the average thermodynamic and convective structure of an AEW (e.g. Kiladis et al. 2006, Figure 11) over West Africa, the AEW exhibits a very similar thermodynamic and convective structure to that presented in Figure 1.6. This raises the possibility that some aspects of the stratiform instability may be applied to AEWs.

The mechanism coupling convection to the wave in stratiform instability is the wave's variability of CIN and CAPE. In the DRW the coupling mechanism is adiabatic forcing for ascent. If, on the other hand, AEWs organize convection via horizontal moisture convergence, as presented by Tomassini et al. (2017), the coupling mechanism for moisture-stratiform instability (Kuang 2008) may be relevant for AEWs. This study will introduce and discuss whether some aspects of stratiform instability may be applied to the AEW-convection interaction.

In summary we will attempt to combine the knowledge gained in this study into a complete conceptual model of AEW-convection interaction by addressing the following questions:

1. What aspects of the DRW mechanism and/or stratiform instability are present in AEWs?

2. Can we combine aspects of these processes into a model for AEW-convection interaction?

CHAPTER

2

METHODS

2.1 Data

2.1.1 Representation of AEWs

When examining the AEW-convection relationship we have three broad categories of datasets available. These are observations (either in-situ or remote), simulations or reanalyses with parameterized convection, or high-resolution simulations with explicit convection.

Typically, in-situ observations over Africa are not able to provide high enough temporal and spatial resolution to study a relationship with convection. For certain variables such as precipitation, satellite-borne measurements such as the National Aeronautics and Space Administration (NASA) Tropical Rainfall Measurement Mission (TRMM; Huffman et al. 2007) or the Global Precipitation Mission (GPM) do some work toward filling in the gaps. On short temporal scales field programs such as AMMA also provide more data. However, none of these platforms provide a detailed enough picture, either in space, time, or in variables (i.e. thermodynamic, moisture, and kinematic variables) to assess the complete AEW-convection interaction.

Reanalyses or simulations on the other hand, present gridded, dynamically consis-

tent datasets, that can be analyzed in detail. However, they do not always replicate reality appropriately. Janiga and Thorncroft (2016) aptly summarized the issues with recent examinations of AEWs that primarily employ simulations or reanalyses with parameterized or superparameterized convection. Such models typically underestimate the rain rate in the northerlies and overestimate the rain rate in the trough and southerlies (e.g. Skinner and Diffenbaugh 2013; McCrary et al. 2014; Crétat et al. 2015). These representations also fail to resolve MCSs which account for a majority of the convection over West Africa (Janiga and Thorncroft 2014). An accurate representation of MCSs is important to diagnose differences in vertical profiles of heating and the level of PV generation.

Simulations with explicit convection (i.e. convection-permitting at 4km or lower grid-spacing) are able to represent MCSs. Pearson et al. (2014) also showed that convection-permitting simulations are much better at simulating the diurnal cycle over West Africa. Since MCSs are strongly modulated by the diurnal cycle (Laing and Fritsch 1993), convection-permitting simulations are important for both the initiation and intensity of MCSs. The only study that uses convection-permitting simulations to examine convection in relation to AEWs is Schwendike and Jones (2010). In this study they examined just two MCSs, only resolving convection for a limited period of the lifetime of an AEW and this study is therefore limited in scope.

Our approach in this study will be to use all three types of datasets in conjunction with each other where and when possible. We expect that explicit representation of MCSs may be required to correctly represent the phase relationship between AEWs and convection and the correct structure of heating profiles in MCSs. Thus we will make heavy use of high resolution simulations.

2.1.2 Reanalyses and Precipitation

The reanalyses used in this study are the European Center for Medium Range Weather Forecasting's (ECMWF) ERA-Interim reanalysis (ERAI; Dee et al. 2011) and the National Center for Environmental Prediction's (NCEP) Climate Forecast System reanalysis (CFSR; Saha et al. 2010). These reanalysis products are used to provide a best estimate of typical atmospheric variables such as temperature, winds, and moisture. The use of two reanalyses is not to provide a detailed comparison between the two. Rather, two reanalyses are used in order to note which features are independent of the various dynamics, parameterizations, and data assimilation schemes used in the reanalyses. The utility of using multiple reanalyses for examination of AEWs is highlighted in Janiga and Thorncroft (2013) since

parameters such as heating rates can be highly sensitive to the various parameterizations. The grid-spacing of the datasets are approximately 0.8° for ERAI and 0.5° for CFSR. Both will sufficiently resolve synoptic-scale features such as the AEW but will not resolve mesoscale features such as Mesoscale Convective Systems (MCSs).

Precipitation is represented by the TRMM Multi-Satellite Precipitation Analysis (TMPA-RT) dataset. All results in this study are based on these datasets from the period 1998-2010. This period is chosen since this is the only period for which all the above datasets (ERAI, CFSR, and TRMM) overlap temporally.

2.1.3 Convection Permitting Simulations

Control Simulations

Simulations are performed using the Weather Research and Forecasting model (WRF-ARW version 3.9.1.1; Skamarock et al. 2005). The domain setup is shown in Figure 2.1. A 36 km grid-spacing outer domain is used with inner domains of 12 km and 4 km grid-spacing. This setup is used to down-scale the initial conditions, the ERAI, with a grid-spacing of approximately 80 km, to a convection-allowing resolution. Two different AEWs are simulated, one from 2010 between the 19th-28th August (that lead to the genesis of Hurricane Earl) and one from 2007 between 6th-17th September (that did not lead to the genesis of a TC).

The focus of this study will be on the 4 km domain since this best resolves moist convection. While 4 km grid spacing is not sufficient to capture distinct convective cellular structures (Bryan et al. 2003), it sufficiently represents mesoscale aspects of MCSs such as trailing stratiform cloud regions and the associated MCVs (Weisman et al. 1997), which are of most interest here, and negates the need for cumulus parameterization. Parameterization schemes used are documented in Table 2.1. The Tiedtke cumulus scheme, which runs only on the 12 and 36 km domains, is utilized for its inclusion of convective momentum adjustment, which has been shown important for simulations of hurricanes, and therefore possibly AEWs (Tiedtke 1989; Zhang et al. 2011). The Thompson microphysics scheme provides double moment representation of ice, which is important for an accurate representation of the heating profile created by stratiform cloud regions. The Shin-Hong boundary layer scheme is utilized for its adaptive representation of the planetary boundary layer (PBL), deemed important because of the vast changes in the Saharan PBL on a diurnal scale (Shin and Hong 2015). Finally the RRTMG radiation schemes are chosen for their

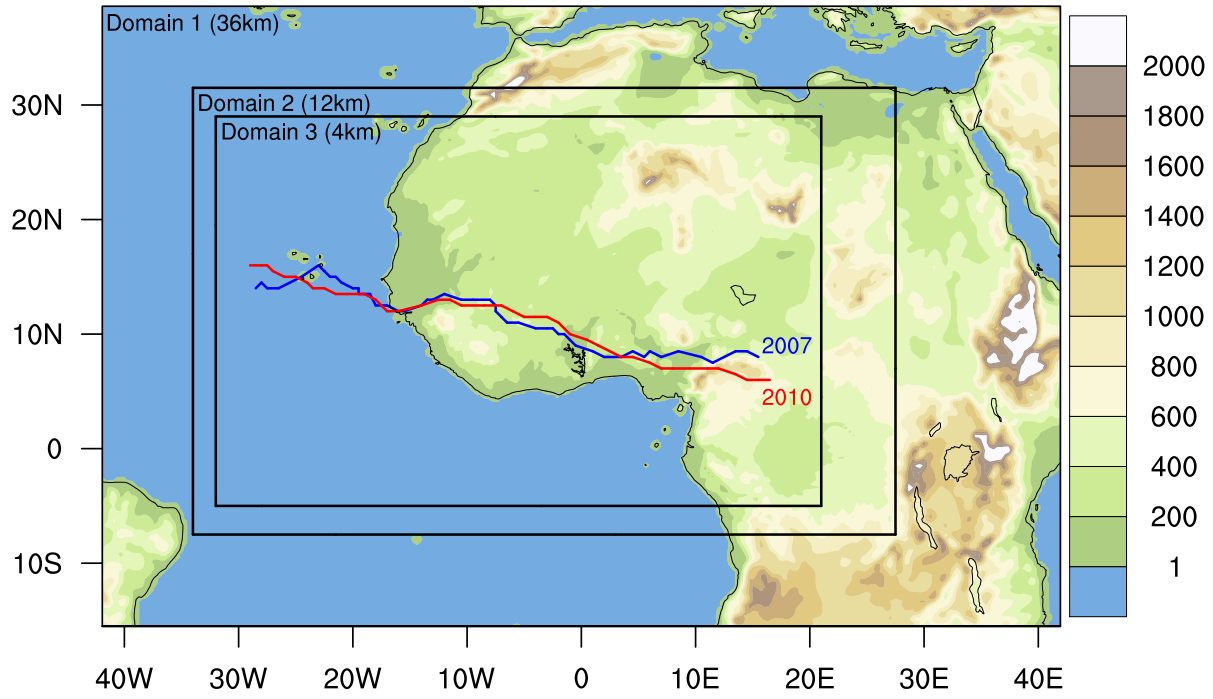

Figure 2.1: WRF domain setup for all simulations with model terrain height (m) shaded. Manually defined AEW tracks following the positive vorticity center and meridional wind minima (i.e. the trough) in the control simulations are shown. The blue track is for the 2007-CTRL AEW (09/06 00Z to 09/17 00Z) and the red track is for the 2010-CTRL AEW (8/19 00Z to 8/27 12Z).

advanced interactions with clouds (Price et al. 2014). The simulations are initialized with a Dolph digital filter run backward and forward two hours to remove initial imbalances in the model initial conditions. It is found that this combination of filtering and parameterization schemes produces the best representation of the AEWs, as represented by ERAI and TRMM data. Filtering also allows for the initial conditions, especially those that are adjusted in sensitivity studies that will be described, to be balanced prior to the simulation start.

Table 2.1: Parameterization schemes used in the 2007 and 2010 simulations.

Parameterization	Scheme	WRF Option
Cumulus	Modified Tiedtke	6
Microphysics	Thompson	8
Boundary Layer	Shin-Hong	11
Surface Layer	Revised MM5	1
Land Surface	Noah LSM	2
Radiation (SW & LW)	RRTMG	4

A control simulation is run for each AEW (hereafter referred to as CTRL). Time-longitude diagrams of 650hPa meridional winds and precipitation from the CTRL simulations are shown in Figures 2.2c and 2.2d for the 2007 and 2010 AEWs respectively. To provide a valid comparison we regrid the simulations to the ERAI and TRMM grids for winds and precipitation respectively. CTRL simulations are favorably comparable to the "observed" AEWs. All the AEWs follow similar tracks as can be seen by comparing the CTRL tracks to the ERAI meridional winds. Further, meridional winds intensify and decay at similar times between the CTRL simulations and ERAI observations. Finally TRMM and CTRL precipitation is similar with consistent precipitation in the northerlies of each AEW and weaker, if any, precipitation in the southerlies of each AEW. The only qualitative differences are slightly faster AEWs in the ERAI compared to the CTRL, especially over the ocean. While it is helpful to have a simulation that very closely matches reality, the goal of the study is not to recreate the AEW exactly, but to simulate an AEW that is appropriately realistic and examine it's relationship with convection. Given this, we believe these simulations suitably recreate the AEWs.

A third control simulation with some different parameters is also used for analysis in Chapter 3. The simulation is between 3rd-12th August 2017, also performed using the

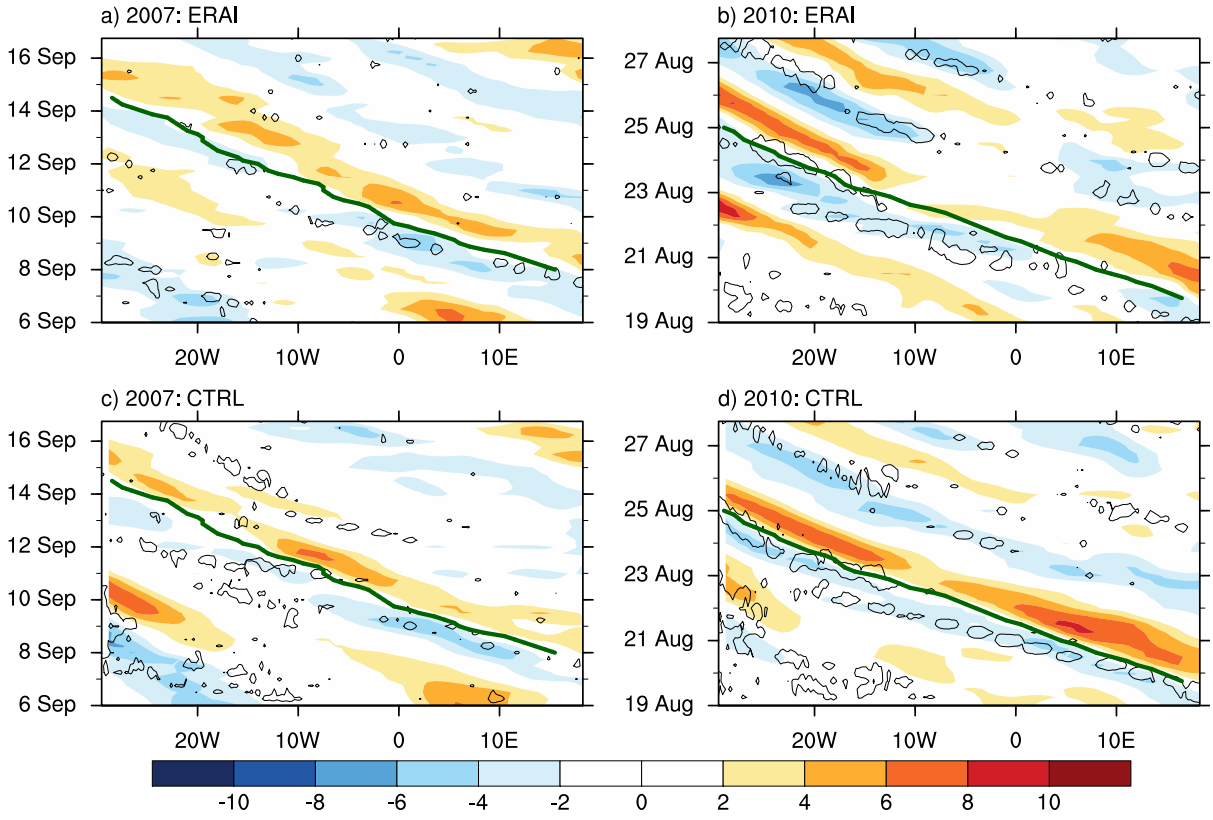

Figure 2.2: Time-longitude plots of 5-20°N averaged 650hPa meridional winds (m/s, filled) and precipitation (mm/hr, only 1mm/hr contour shown) for the a) 2007 AEW in ERAI, b) AEW in 2007-CTRL, c) 2010 AEW in ERAI, and d) AEW in 2010-CTRL. a) and c) use the TRMM 3B42 product to represent precipitation. For comparison all model data is regridded to the ERAI and TRMM grids for winds and precipitation respectively. The analyzed track of the control simulation for each year is represented by the thick green lines.

WRF. This simulation utilizes an outer domain with 12km grid spacing similar to the 36km domain in Figure 2.1, and an inner domain with 4km grid spacing similar to the 4km domain in Figure 2.1. Initial and boundary conditions were provided by the 1/4° Global Forecast System (GFS) at forecast hour 0. The only other difference from other simulations is the use of WDM6 microphysics instead of Thompson. This simulation also favorably replicates the AEW in question, relative to ERAI and GFS analyses (not shown). Unfortunately, for data storage reasons, this simulation could not be retained and the information gleaned from it is only used in a limited manner in Chapter 3 with the purpose of supporting data from the other simulations.

Sensitivity Studies

A series of sensitivity studies are performed to examine the difference between AEWs with and without the effects of convection. Two different sensitivity studies are carried out. The first removes the condensational heating produced by the microphysics scheme. Such simulations are denoted NOMH hereafter. Since there is no active convection scheme in the 4 km domain this represents a removal of any and all condensational heating. These simulations produce close to zero precipitation. This lack of precipitation can be explained through parcel theory. Assuming a rising parcel, once a parcel reaches the lifting condensation level (LCL) in normal atmospheric conditions it would begin rising at the moist adiabatic lapse rate (MALR) due to the release of heat by condensation. However, since there is no condensational heating in these simulations, rising parcels continue to rise at the dry adiabatic lapse rate (DALR). Since the DALR is much steeper than that of the MALR, rising parcels would be much cooler than the environment in most cases. Thus rising parcels in these simulations are typically stable to convective motions. Since most precipitation over West Africa in the summer originates from deep convection, precipitation is therefore vastly reduced in the simulations.

The second type of sensitivity study involves varying the moisture in the initial conditions. In these studies the relative humidity and surface moisture in the initial and boundary condition are modified by a factor of 0.5. This is accomplished by editing the WRF model input meteorological files produced after running the WRF Pre-processing System (WPS). Hereafter these simulations are denoted HLFM. These simulations are designed to limit most moist convection. From the parcel theory perspective, this method of limiting convection is less severe than the previous method. Release of latent heat by condensational processes is still possible here and thus so is moist convection. In these studies, by limiting

Table 2.2: Summary of all simulations. M represents all mixing ratio variables and MP stands for microphysics. Times are in UTC.

Abbreviation	Date and Time	Modification
CTRL-2007	6/9 00Z – 17/9 00Z	None
HLFM-2007	8/9 12Z – 17/9 00Z	M reduced 50% at first time
NOMH-2007	8/9 12Z – 17/9 00Z	Zero temperature tendency in MP scheme
CTRL-2010	19/8 00Z – 28/8 00Z	None
HLFM-2010	20/8 12Z – 28/8 00Z	M reduced 50% at first time
NOMH-2010	20/8 12Z – 28/8 00Z	Zero temperature tendency in MP scheme
CTRL-2017	3/8 00Z – 13/8 00Z	None

relative humidity and surface moisture, the dew point is lower, and LCLs are higher. As a result, it is harder for convection to realize convective available potential energy (CAPE) through moist convection, although not impossible. This leads to much less precipitation. This is especially prevalent later in the simulations when some moisture has been reintroduced by evaporation and transpiration from the land surface scheme. Multiple factors were tested (0.9, 0.7, 0.5, 0.25, 0) but an examination of these showed that 0.5 presented the best way to limit convection while at the same time maintaining an environment that reflected reality.

While both sensitivity studies are flawed in that they modulate the overall environment, they do not represent the same change to the environment; one essentially completely stabilizes the environment to any deep convection whilst the other severely reduces the moisture but still allows some moist convection. Further, by using a 4km domain we do not have completely unrealistic large scale overturning circulations as with shutting off the convection scheme in a much larger grid-spacing simulation. It is therefore expected that these simulations produce a much more "realistic" removal of deep moist convection than switching off the convection scheme. In reality there is no perfect way to limit convection in a simulation and therefore results from these simulations should be thought of as supplementing those from the sensitivity study presented in Berry and Thorncroft (2012) rather than replacing or improving upon them.

Analysis of Simulations

In order to discern characteristics of the AEWs from these high resolution simulations, we utilize a number of techniques in order to better represent AEWs. To obtain data representative of the AEW, variables are first smoothed in space using a 500 km wide Gaussian weighted window. This provides us with variables that are smoothed to an effective resolution of 3000-4000 km (the AEW scale). In this case variables on the scale of convection should have been smoothed out. From this we then calculate time-mean averages defined as the mean of all output times over the whole simulation at any given location. We then define perturbations as the difference between any filtered variable and its time mean filtered variable at any given location. This allows for the removal of the background features (such as the AEJ) from perturbation variables. Since AEWs are the dominant synoptic scale pattern in the region, this gives us our best estimate of the variables that represent the AEW.

2.2 Potential Vorticity

PV is a useful quantity with which to analyze AEWs as it combines both thermodynamic and kinematic properties of the wave into one variable. More specifically a PV tendency equation or budget as we shall describe it herein, directly links diabatic heating (or more accurately the gradients of diabatic heating) to generation of PV (Hoskins et al. 1985). Through PV we can therefore directly quantify the contribution of convection to the AEW. Further, given an appropriate balance condition (such as quasi-geostrophic or nonlinear balance), PV can be inverted to obtain the balanced wind and mass fields. Thus PV also describes the balanced part of the circulation, and by understanding it's sources and sinks, it is possible to describe the balanced dynamics of AEWs.

Many approaches to understand the role of convection in modifying AEWs have used energy budgets to understand AEW growth (e.g. Hsieh and Cook 2007; Berry and Thorncroft 2012; Poan et al. 2014). However, energy budgets do not cleanly separate the adiabatic and diabatic processes. Moist convective and dry baroclinic energy sources are typically pooled into the baroclinic term, making it difficult to understand whether the growth is through dry or moist baroclinic processes. Thus an analysis of PV in the AEW represents a useful addition to the current understanding strongly focused on energetics.

A number of studies have examined PV in AEWs. Janiga and Thorncroft (2013) showed that there is on average diabatic PV generation in the mid-levels over West Africa and Tomassini et al. (2017) showed that latent heating at and slightly ahead of the AEW trough

reinforces the AEW through diabatic PV generation between 500-800 hPa. Given that there are distinct diabatic sources of PV in the low-mid levels of AEWs it is important to put these in context with their adiabatic counterparts, as was discussed in the introduction.

2.2.1 Isobaric analysis

Here we derive a potential vorticity (PV) budget in the presence of non-conservative effects of diabatic heating. For such an analysis, isentropic coordinates are typically used since PV takes a relatively simpler form and diabatic heating is directly related to the cross-isentropic pseudo-vertical motion. However, here we use isobaric coordinates for the analysis for a variety of reasons. First, isentropes in the vicinity of the AEW track have steep slopes relative to geometric or isobaric surfaces. This is a result of the intense heating of the surface layer over the Sahara Desert and relatively cooler air over the Gulf of Guinea. Steeply sloping isentropes lead to two main problems. First comparing AEW PV to well understood and well documented features in the vicinity of AEWs is difficult as these features are typically defined on isobaric surfaces. Second, when isentropes intersect the surface there are now sources of PV on isentropes. Furthermore, since we desire to examine the full 3-D structure of the wave, including near the surface, the choice of a vertical co-ordinate does not make a major difference in practice.

2.2.2 Fundamental Equations

The primitive equations on isobaric coordinates (Vallis 2006, pg. 79, eqn. 2.153) are:

$$\frac{D\vec{V}}{Dt} = -f\hat{k}\times\vec{V} - \vec{\nabla}\Phi + \vec{F}, \tag{2.1}$$

$$\frac{D\theta}{Dt} = \frac{J\theta}{c_p T} = Q, \tag{2.2}$$

$$\vec{\nabla}\cdot\vec{U} = \vec{\nabla}\cdot\vec{V} + \frac{\partial\omega}{\partial p} = 0, \tag{2.3}$$

$$\frac{\partial\Phi}{\partial p} = -\alpha \tag{2.4}$$

where $\vec{V} = u\hat{i} + v\hat{j}$, $\vec{U} = u\hat{i} + v\hat{j} + \omega\hat{k}$, $\vec{\nabla} = \hat{i}\frac{\partial}{\partial x} + \hat{j}\frac{\partial}{\partial y} + \hat{k}\frac{\partial}{\partial p}$, $\frac{D}{Dt} = \frac{\partial}{\partial t} + \vec{U}\cdot\vec{\nabla}$, J is the diabatic heat, Q is the diabatic heating rate, and all other variables have their typical meteorological meanings. Equation 2.1 is the horizontal momentum equation, equation 2.2 is the thermodynamic equation, equation 2.3 is the continuity equation, and equation

2.4 is hydrostatic balance.

2.2.3 Derivation of an Isobaric Vorticity budget

If we separate equation 2.1 into its zonal and meridional components we obtain:

$$\frac{\partial u}{\partial t} + u\frac{\partial u}{\partial x} + v\frac{\partial u}{\partial y} + \omega\frac{\partial u}{\partial p} = fv - \frac{\partial \Phi}{\partial x} + F_x, \tag{2.5}$$

and:

$$\frac{\partial v}{\partial t} + u\frac{\partial v}{\partial x} + v\frac{\partial v}{\partial y} + \omega\frac{\partial v}{\partial p} = -fu - \frac{\partial \Phi}{\partial y} + F_y, \tag{2.6}$$

We can define a hydrostatic absolute vorticity in isobaric coordinates as:

$$\vec{\eta} = f - \hat{i}\frac{\partial v}{\partial p} + \hat{j}\frac{\partial u}{\partial p} + \hat{k}\left(\frac{\partial v}{\partial x} - \frac{\partial u}{\partial y}\right) \tag{2.7}$$

We can form a three dimensional vorticity equation by taking $-\frac{\partial}{\partial p}$(2.6) for the $\hat{i}$ component, $\frac{\partial}{\partial p}$(2.5) for the $\hat{j}$ component, and $\frac{\partial}{\partial x}(2.6)-\frac{\partial}{\partial y}$(2.5) for the $\hat{k}$ component. Further, also using equation 2.3 we obtain:

$$\frac{D\vec{\eta}}{Dt} = \frac{\partial \vec{\eta}}{\partial t} + (\vec{U}\cdot\vec{\nabla})\vec{\eta} = (\vec{\eta}\cdot\vec{\nabla})\vec{U} + \vec{\nabla}\times\vec{\nabla}_p\Phi + \vec{\nabla}\times\vec{F} \tag{2.8}$$

where $\vec{\eta}$ is the absolute vorticity vector. This equation is our vorticity budget in isobaric coordinates.

2.2.4 Derivation of an Isobaric Potential Vorticity Budget

Now we wish to combine the vorticity equation we have obtained with the thermodynamic information we have, in order to obtain a PV equation. Operating $\vec{\nabla}\theta\cdot$ on equation 2.8 gives:

$$\begin{aligned}\vec{\nabla}\theta\cdot\frac{D}{Dt}\vec{\eta} &= \vec{\nabla}\theta\cdot(\vec{\eta}\cdot\vec{\nabla})\vec{U} + \vec{\nabla}\theta\cdot(\vec{\nabla}\times\vec{\nabla}_p\Phi) + \vec{\nabla}\theta\cdot\vec{\nabla}\times\vec{F} \\ &= (\vec{\eta}\cdot\vec{\nabla})\vec{U}\cdot(\vec{\nabla}\theta) + \vec{\nabla}\theta\cdot\vec{\nabla}\times\vec{F}\end{aligned} \tag{2.9}$$

It's not immediately clear here why the solenoidal term vanishes. We can write:

$$\vec{\nabla}_p\Phi = \vec{\nabla}\Phi - \hat{k}\frac{\partial \phi}{\partial p} = \vec{\nabla}\Phi - \hat{k}\alpha \tag{2.10}$$

and then the solenoidal term becomes:

$$\begin{aligned}\vec{\nabla}\theta\cdot(\vec{\nabla}\times\vec{\nabla}_p\Phi) &= \vec{\nabla}\theta\cdot\vec{\nabla}\times\vec{\nabla}\Phi-\vec{\nabla}\theta\cdot\vec{\nabla}\times\hat{k}\alpha=-\vec{\nabla}\theta\cdot\vec{\nabla}\times\hat{k}\alpha \\ &= \vec{\nabla}\theta\cdot\hat{k}\times\vec{\nabla}\alpha=\frac{\partial\theta}{\partial y}\frac{\partial\alpha}{\partial x}-\frac{\partial\theta}{\partial x}\frac{\partial\alpha}{\partial y}\end{aligned} \tag{2.11}$$

since $\nabla\times\nabla=0$. θ and α can both be expressed as functions of temperature, $T(x,y,p)$ and pressure, p. But we are holding pressure fixed in the partial differentials. This means that both θ and α are only a function of temperature on an isobaric surface. Thus the solenoidal term should be identically zero. This can be confirmed by using the expressions for θ and α as:

$$\theta = T\frac{p_0}{p}^{\frac{R}{c_p}} \tag{2.12}$$

and

$$\alpha=\frac{RT}{p} \tag{2.13}$$

and then the solenoidal term becomes:

$$\frac{R}{p}\frac{p_0}{p}^{\frac{R}{c_p}}\left(\frac{\partial T}{\partial y}\frac{\partial T}{\partial x}-\frac{\partial T}{\partial y}\frac{\partial T}{\partial x}\right)=0 \tag{2.14}$$

Now operating $\vec{\eta}\cdot\vec{\nabla}$ on the thermodynamic (equation 2.2) gives:

$$\vec{\eta}\cdot\vec{\nabla}\frac{D\theta}{Dt}=\vec{\eta}\cdot\vec{\nabla}Q \tag{2.15}$$

Using the product rule, we can write the left hand side of equation 2.15 as:

$$\begin{aligned}\vec{\eta}\cdot\vec{\nabla}\frac{D\theta}{Dt} &= \vec{\eta}\cdot\vec{\nabla}\left(\frac{\partial\theta}{\partial t}+\vec{U}\cdot\vec{\nabla}\theta\right) \\ &= \vec{\eta}\cdot\frac{\partial}{\partial t}\vec{\nabla}\theta+\vec{\eta}\cdot\vec{\nabla}(\vec{U}\cdot\vec{\nabla}\theta) \\ &= \vec{\eta}\cdot\frac{\partial}{\partial t}\vec{\nabla}\theta+\vec{\eta}\cdot(\vec{U}\cdot\vec{\nabla})(\vec{\nabla}\theta)+(\vec{\eta}\cdot\vec{\nabla})\vec{U}\cdot(\vec{\nabla}\theta) \\ &= \vec{\eta}\cdot\frac{D}{Dt}\vec{\nabla}\theta+(\vec{\eta}\cdot\vec{\nabla})\vec{U}\cdot(\vec{\nabla}\theta)\end{aligned} \tag{2.16}$$

Substituting equation 2.16 in to equation 2.15 gives:

$$\vec{\eta}\cdot\frac{D}{Dt}\vec{\nabla}\theta = -(\vec{\eta}\cdot\vec{\nabla})\vec{U}\cdot(\vec{\nabla}\theta)+\vec{\eta}\cdot\vec{\nabla}Q \tag{2.17}$$

Adding equations 2.17 and 2.9 gives a combined vorticity and thermodynamic equation:

$$\begin{aligned}\vec{\eta}\cdot\frac{D}{Dt}\vec{\nabla}\theta+\vec{\nabla}\theta\cdot\frac{D}{Dt}\vec{\eta} &= \frac{D}{Dt}(\vec{\eta}\cdot\vec{\nabla}\theta)\\ &= -(\vec{\eta}\cdot\vec{\nabla})\vec{U}\cdot(\vec{\nabla}\theta)+(\vec{\eta}\cdot\vec{\nabla})\vec{U}\cdot(\vec{\nabla}\theta)+\vec{\eta}\cdot\vec{\nabla}Q\\ &+\vec{\nabla}\theta\cdot(\vec{\nabla}\times\vec{\nabla}_p\Phi)+\vec{\nabla}\theta\cdot\vec{\nabla}\times\vec{F}\\ &= \vec{\eta}\cdot\vec{\nabla}Q+\vec{\nabla}\theta\cdot\vec{\nabla}\times\vec{F}\end{aligned} \tag{2.18}$$

Multiplying through by gravity:

$$\frac{D}{Dt}(-g\vec{\eta}\cdot\vec{\nabla}\theta) = -g\vec{\eta}\cdot\vec{\nabla}Q-g\vec{\nabla}\theta\cdot\vec{\nabla}\times\vec{F}. \tag{2.19}$$

and defining P, the isobaric PV as:

$$P = -g(\vec{\eta}\cdot\vec{\nabla}\theta), \tag{2.20}$$

Equation 2.18 then becomes the PV budget:

$$\boxed{\frac{DP}{Dt} = -g\vec{\eta}\cdot\vec{\nabla}Q-g\vec{\nabla}\theta\cdot\vec{\nabla}\times\vec{F}} \tag{2.21}$$

This equation states that isobaric PV is conserved under adiabatic, frictionless, and hydrostatic flow. We can expand equation 2.21 by stating that the relative vorticity vector is $\vec{\zeta} = \vec{S}+\zeta$ where S is the horizontal components of vorticity (the shear) and ζ represents the vertical component (in isobaric coordinates):

$$\underbrace{\frac{\partial P}{\partial t}}_{\text{A}} = \underbrace{-\vec{V}\cdot\vec{\nabla}P}_{\text{B}}\underbrace{-\omega\frac{\partial P}{\partial p}}_{\text{C}}-g\Big[\underbrace{\vec{S}\cdot\vec{\nabla}Q}_{\text{D}}+\underbrace{(\zeta+f)\frac{\partial Q}{\partial p}}_{\text{E}}\Big]\underbrace{-g\vec{\nabla}\theta\cdot\vec{\nabla}\times\vec{F}}_{\text{F}}. \tag{2.22}$$

Here term A is the local PV tendency, terms B and C are the horizontal and vertical advection of PV respectively, terms D and E represent the generation of PV by diabatic heating gradients in the horizontal and vertical respectively, and term F represents the effects of friction in dissipating or generating PV.

2.3 Diabatic Heating Rates

A key variable required for our analyses is the diabatic heating rate, Q. Since ERAI does not provide diabatic heating rates, this is estimated using the thermodynamic residual (Yanai et al. 1973; Hagos et al. 2010):

$$Q_1 = \frac{D\theta}{Dt} = \frac{\partial\theta}{\partial t} + u\frac{\partial\theta}{\partial x} + v\frac{\partial\theta}{\partial y} + \omega\frac{\partial\theta}{\partial p}. \tag{2.23}$$

CFSR and WRF do provide heating rates as output from the various parameterization schemes. The sum of all diabatic heating from the parameterization schemes is denoted H. We will also examine the role of diabatic heating sources from the sum of all convective (shallow and deep) and microphysical processes (denoted H_L), the sum of both longwave and shortwave radiative schemes (denoted H_R), and the boundary layer scheme (denoted H_B). In the case of our WRF simulations H_L is simply the microphysical heating rate since there is no cumulus scheme active in our 4km domain of interest. CFSR provides these heating rates on a 1° grid. A bilinear interpolation is used to interpolate these to the same 0.5° grid as the rest of the CFSR variables.

2.4 Perturbation PV Budget

Returning to the PV budget (equation 2.22), the source terms can be further separated by splitting variables into their time-mean and perturbation components (e.g. $V = \bar{V} + V'$). This yields a perturbation PV equation where source terms are separated into products of time-mean and perturbation variables:

$$\begin{aligned}\frac{\partial P'}{\partial t} = &-\bar{V}\cdot\nabla P' - V'\cdot\nabla\bar{P} - V'\cdot\nabla P' - \left[\omega\frac{\partial P}{\partial p}\right]' \\ &-\left[g\vec{\eta}\cdot\vec{\nabla}Q\right]' - \left[g\vec{\nabla}\theta\cdot\vec{\nabla}\times\vec{F}\right]'.\end{aligned} \tag{2.24}$$

The advantage of this separation of terms is in the interpretation of the equation. The first term on the right hand side (RHS) of equation 2.24 is an advection of the perturbation PV by the background flow. The second term on the RHS can be interpreted through RW dynamics. From the perspective of propagation, the advection of background PV by perturbation winds is the process driving the background flow relative phase speed of a RW. This is the beta-effect. From the perspective of growth, this process is representative of baroclinic

and barotropic instability since, from the PV perspective, these growth mechanisms are driven by perturbation advections of background PV (e.g. Eady 1949; Kuo 1949). The third term on the RHS is a nonlinear advection while the fourth term is perturbation vertical advection. When using only the heating from cloud and precipitation processes in the fifth term, this can be interpreted as contributions to the growth and propagation of a DRW. Thus this separation yields useful physical insight for the AEW, as we can separate RW dynamics from that of diabatic processes. This equation is used extensively in Chapter 5 where we examine the dynamics of AEWs in the high-resolution simulations.

2.5 Filtering

In Chapters 3 and 4 we examine the dynamics of AEWs in the reanalyses. There, we obtain perturbations representative of AEWs by filtering fields for AEW scales. Filtering is applied using wavenumber-frequency techniques as discussed in Hayashi (1982) and as implemented in Wheeler and Kiladis (1999).

Figure 2.3 shows the power spectrum of TRMM precipitation between 5-15°N and 30°W-30°E (the peak region of AEW activity). We choose to focus on precipitation here as our main goal is to examine the convectively coupled systems over Africa. A clear region of power on the westward side of the spectrum is continuous from high wavenumbers and diurnal-scale frequencies to low wavenumbers and 8 day periods. This indicates a continuum from spatially large, diurnally varying mesoscale convective systems (MCSs), through AEWs, to planetary scale disturbances with longer periods. We filter variables for 2-8 day periods, 6-26 wavenumbers (approximately 1500-6500 km wavelength assuming an Earth circumference of approximately 40,000 km), and only westward propagating signals. These ranges are selected to encompass the typical range of AEW wavelengths and periods. The strongest power occurs within the filter region shown with a solid box.

For our AEW-scale filtering, a 2 day period and 1500 km wavelength are chosen to minimize the influence of mesoscale precipitation features such as MCSs. An 8 day period and 6500 km wavelength are chosen since this is the maximum conceivable wavelength for an AEW (the width of Africa at 10°N is approximately 6000 km). From here on, any variable that is filtered in this manner is referred to as an AEW-scale variable and is denoted X_w where X is an arbitrary variable and subscript w denotes the variable has been filtered.

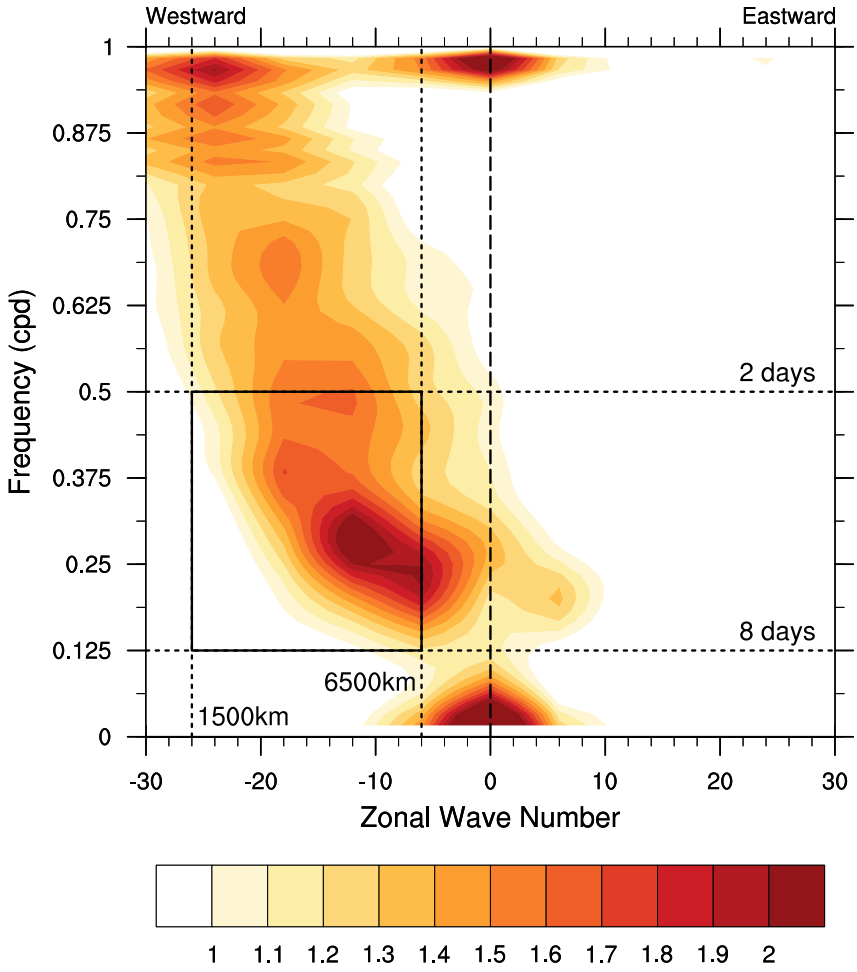

Figure 2.3: Wavenumber-frequency power spectrum of the TRMM precipitation for July-September 1998-2010, averaged from 5°N to 15°N, plotted as the ratio of the raw precipitation spectrum against a smooth red noise background. Solid box represents a region for AEW-scale filtering. Dashed lines represent various periods and wavelengths for reference.

2.6 Wave PV Budget

We now wish to separate the terms in the isobaric PV budget (Equation 2.22) budget such that we can isolate the contributions on the AEW scale.

2.6.1 Derivation

If we define the variables involved in the PV budget as the sum of their time-mean, AEW-scale, and residual components:

$$X = \bar{X} + X_w + X_r \tag{2.25}$$

where the $\bar{X}$ represents a July-August-September (JAS) time-mean, and X_r represents the residual of X once the AEW-scale and time-mean components are subtracted from the full variable X. This residual therefore encompasses any eastward propagating anomalies (e.g. equatorial Kelvin Waves, mid-latitude disturbances) and any processes on a diurnal time scale (e.g. afternoon convection). Neglecting friction in equation 2.22 and applying a filter for the AEW-scale, we obtain:

$$\begin{aligned}\left(\frac{\partial P}{\partial t}\right)_w &= -(\vec{V}\cdot\vec{\nabla}P)_w - \left(\omega\frac{\partial P}{\partial p}\right)_w - g\left(\vec{S}\cdot\vec{\nabla}Q + (\zeta+f)\frac{\partial Q}{\partial p}\right)_w \\ \frac{\partial P_w}{\partial t} &= \underbrace{-(\vec{V}\cdot\vec{\nabla}P)_w}_{\text{A}} \underbrace{-\left(\omega\frac{\partial P}{\partial p}\right)_w}_{\text{B}} \underbrace{-g(\vec{S}\cdot\vec{\nabla}Q)_w}_{\text{C}} \underbrace{-g\left((\zeta+f)\frac{\partial Q}{\partial p}\right)_w}_{\text{D}}\end{aligned} \tag{2.26}$$

Using term B here as an example, we can expand each term by separating the variables into their time-mean and perturbations (e.g. $\omega = \bar{\omega} + \omega'$ and $P = \bar{P} + P'$) such that:

$$\omega\frac{\partial P}{\partial p} = \bar{\omega}\frac{\partial \bar{P}}{\partial p} + \omega'\frac{\partial \bar{P}}{\partial p} + \bar{\omega}\frac{\partial P'}{\partial p} + \omega'\frac{\partial P'}{\partial p} \tag{2.27}$$

and then applying an AEW-scale filter, term B will become:

$$\left(\omega\frac{\partial P}{\partial p}\right)_w = 0 + \omega_w\frac{\partial \bar{P}}{\partial p} + \bar{\omega}\frac{\partial P_w}{\partial p} + \left(\omega'\frac{\partial P'}{\partial p}\right)_w. \tag{2.28}$$

If we now define $\omega' = \omega_w + \omega_r$ and $P' = P_w + P_r$, equation 2.28:

$$\left(\omega' \frac{\partial P'}{\partial p}\right)_w = \left(\omega_w \frac{\partial P_w}{\partial p}\right)_w + \left(\omega_w \frac{\partial P_r}{\partial p}\right)_w + \left(\omega_r \frac{\partial P_w}{\partial p}\right)_w + \left(\omega_r \frac{\partial P_r}{\partial p}\right)_w \tag{2.29}$$

then term B becomes:

$$\left(\omega \frac{\partial P}{\partial p}\right)_w = \omega_w \frac{\partial \bar{P}}{\partial p} + \bar{\omega} \frac{\partial P_w}{\partial p} + \left(\omega_w \frac{\partial P_r}{\partial p}\right)_w + \left(\omega_r \frac{\partial P_w}{\partial p}\right)_w + \left(\omega_w \frac{\partial P_w}{\partial p}\right)_w + \left(\omega_r \frac{\partial P_r}{\partial p}\right)_w \tag{2.30}$$

If we do this for all terms in equation 2.26, the AEW-scale PV budget becomes:

$$\begin{aligned} \underbrace{\frac{\partial P_w}{\partial t}}_{\text{A}} = &\underbrace{-\vec{U}_w \cdot \vec{\nabla}\bar{P}}_{\text{B}} \underbrace{-\bar{U} \cdot \vec{\nabla} P_w}_{\text{C}} \underbrace{-(\vec{U}_w \cdot \vec{\nabla} P_r)_w}_{\text{D}} \underbrace{-(\vec{U}_r \cdot \vec{\nabla} P_w)_w}_{\text{E}} \underbrace{-(\vec{U}_w \cdot \vec{\nabla} P_w)_w}_{\text{F}} \\ &\underbrace{-\vec{\bar{\eta}} \cdot \vec{\nabla} Q_w}_{\text{G}} \underbrace{-\vec{\zeta}_w \cdot \vec{\nabla}\bar{Q}}_{\text{H}} \underbrace{-(\vec{\zeta}_w \cdot \vec{\nabla} Q_r)_w}_{\text{I}} \underbrace{-(\vec{\zeta}_r \cdot \vec{\nabla} Q_w)_w}_{\text{J}} \underbrace{-(\vec{\zeta}_w \cdot \vec{\nabla} Q_w)_w}_{\text{K}} + residual \end{aligned} \tag{2.31}$$

In addition, we can partition all the above sources of PV into their horizontal and vertical components. For example term G becomes:

$$\vec{\bar{\eta}} \cdot \nabla Q_w = \bar{S} \cdot \nabla Q_w + (\bar{\zeta} + f)\frac{\partial Q_w}{\partial p}. \tag{2.32}$$

2.6.2 Physical Interpretation

Equation 2.31 states that the local AEW-scale PV tendency is comprised of advective and diabatic terms, as well as a term that encompasses friction and other non-AEW scale, residual advective and diabatic processes. The utility of this form of the PV budget is in the scale-interactions it represents. These include interactions between the mean state and AEW-scale perturbations (terms B, C, G, and H in equation 2.31), interactions with residual scale variables (terms D, E, I, and J in equation 2.31), and non-linear interactions (terms F and K in equation 2.31). Some of these scale interaction and non-linear terms are negligible compared to the leading advective and diabatic terms as shown in Chapter 4.

To demonstrate the utility of this equation we will briefly discuss the meaning of a few relevant terms. Term B represents the advection of AEW-scale PV by the background flow. Since this acts on an already present PV anomaly, this will only contribute to propagation

of the AEW. The horizontal component of term C is the advection of background PV by the AEW-scale winds. This source will add PV wherever the AEW winds cross a gradient of PV. Thus from the perspective of a wave in a background flow with significant background PV gradients present, this essentially represents RW dynamics of both growth and propagation. For propagation, this is the beta-effect. For growth, this is barotropic or baroclinic instability. Therefore, these two terms will describe the parts of the dynamics of AEWs that are primarily related to dry RWs.

Term H involves the interaction of AEW-scale circulation with the mean diabatic heating. This is likely of importance within the ITCZ. The vertical gradient of mean diabatic heating is often the leading contributer here. Thus, we can write term H as:

$$-\vec{\zeta}_w \cdot \nabla \bar{Q} \approx -\zeta_w \frac{\partial \bar{Q}}{\partial p} \tag{2.33}$$

Since AEW-scale PV and vorticity anomalies have the same sign, this term will act to damp (amplify) the anomalies when the mean vertical heating gradient is positive (negative). This can be viewed as the vortex stretching term.

Terms G, J, and K all include the AEW-scale diabatic heating. These include moist convection, boundary layer, and radiative processes coupled to the AEW. From the perspective of propagation, if we assume Q is dominated by H_L (the heating associated with moist convective processes), this represents the mechanism of propagation for a DRW. In addition, PV growth can occur via moist baroclinic instability or, as shown in subsequent chapters, by direct addition of PV by diabatic processes within an existing PV anomaly. To illustrate further, the leading contribution from term G is expected to be from the imprint of wave-scale vertical heating gradient on the vertical component of the mean-state absolutely vorticity. That is, term G becomes:

$$\bar{\vec{\eta}} \cdot \nabla Q_w \approx \bar{\zeta} \frac{\partial Q_w}{\partial p} \approx f \frac{\partial Q_w}{\partial p} \tag{2.34}$$

If wave-scale diabatic heating occurs predominantly within the northerlies, then this is equivalent to a dry RW within a positive background meridional PV gradient. Thus, this term can be interpreted as arising due to an equivalent PV gradient due to the vertical gradient of diabatic heating (e.g., Snyder and Lindzen 1991; Cohen and Boos 2016).

2.7 Composite Analysis

In Chapter 3 and 4, average AEWs are generated using a composite analysis technique. Base points for the composite AEWs are selected by examining the AEW storm-tracks, shown in Figure 2.4, represented by the variance of AEW-scale PV and average AEW-scale EKE. Here, AEW-scale EKE is defined as:

$$EKE = \frac{u_w^2 + v_w^2}{2}. \tag{2.35}$$

Two distinct tracks of AEWs can be seen: a low-level northern track (Figures 2.4c, d, g, and h) and a mid-level southern track (Figures 2.4a, b, e, and f). The mid-level southern track of AEWs is the most active with respect to moist convection. Hence, our base points are selected using 650hPa EKE and PV. These are shown in Figure 2.4a. The tracks in ERAI and CFSR are similar enough that the same base points are used for both datasets.

At each base point we average the AEW-scale meridional wind in a volume 5° latitude by 2.5° longitude over the layer 550-750 hPa. Using the resulting time-series the date and time of maxima in northerly winds are selected. A threshold of $1 ms^{-1}$ is used to filter out weak or noisy signals. If two maxima are within 2 days of each other then the largest is assumed to be the main passage of the AEW. This method is demonstrated in Figure 2.5. We chose to focus on the northerlies here as this is often the location of the strongest moist convection in AEWs (e.g. Janiga and Thorncroft 2016) and our main goal is to establish the role of diabatic heating in AEW dynamics. Over the period July-September 1998-2010, this yields about 200-300 AEWs depending on the base point. The base points we focus on are those for the Atlantic (15°N, 30°W), West Africa (10°N, 0°), and East Africa (11°N, 30°E) since these represent three distinct regimes of the AEW; the growing AEW over East Africa, a mature AEW over West Africa, and an AEW over ocean. We then analyze the mean AEW at each base location.

For analyses using this composite method, statistical significance of the anomalies is checked using a 1- or 2-sided Student's T-test with a 95% confidence interval with respect to zero. For simplicity, statistical significance is not shown in figures. But anomalies shown and discussed are all tested and pass the significance tests.

2.8 Tracking of AEWs and MCSs

In Chapters 3 and 5 AEWs and MCSs are manually tracked in the simulations. The AEW trough is analyzed every hour in Chapter 3 and every three hours in Chapter 5. This is done

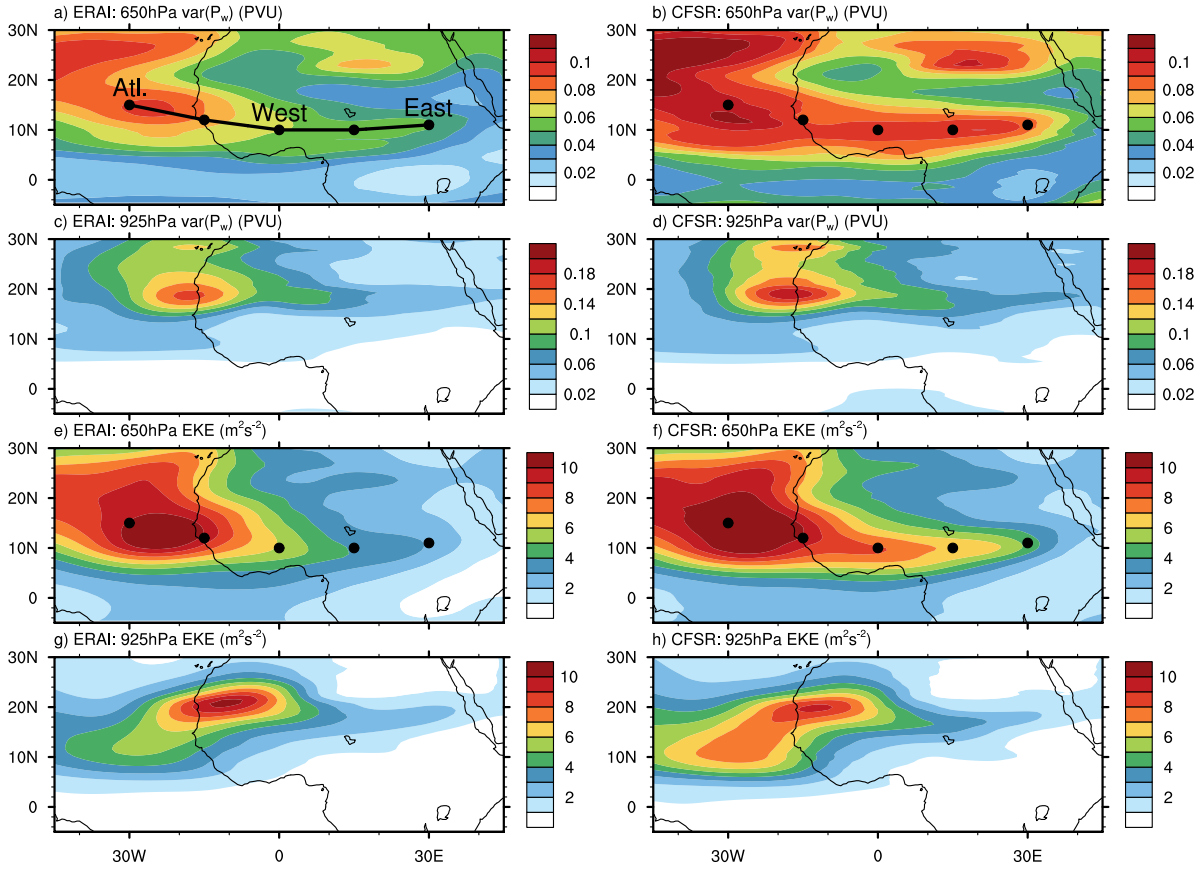

Figure 2.4: a) and b) variance of 650hPa AEW-scale PV, c) and d) variance of 925hPa AEW-scale PV, e) and f) average 650hPa AEW-scale EKE, g) and h) average 925hPa AEW-scale EKE. a), c), e), and g) are for ERAI and b), d), f), and h) are for CFSR. The black line in a) depicts the southern track of AEWs. Black dots and labels indicate composite locations and the names of those locations as referred to in the text.

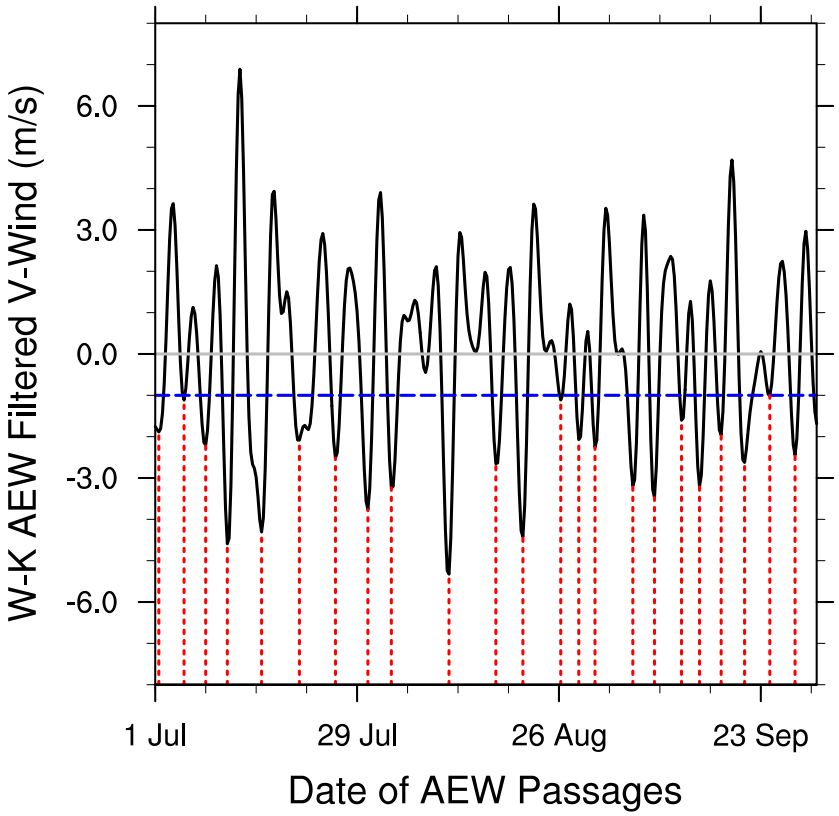

Figure 2.5: Time series of AEW-filtered meridional winds at the base point 10°N latitude, 0° longitude, and 650hPa, between July and September 2010, demonstrating the operation of the composite analysis method. The blue horizontal dashed line depicts the cut off for noise of $1 m s^{-1}$. The vertical red dashed lines depict the identified passage of each AEW as its northerlies pass the base point.

by co-locating the minimum in meridional wind with the maximum in vorticity using maps of 500 hPa meridional winds and vorticity at any given time. Thus the tracks follow the trough. To ensure it is the AEW being tracked (and not smaller-scale convectively associated vorticity maxima), those variables are smoothed using a Gaussian distribution of weights spread over 500km, as described in Section 2.1.3. This leads to variables with an effective resolution much larger than the scale of mesoscale convective systems (MCSs), but similar to that of AEWs. The importance of this scale-separation in tracking AEWs is discussed in Zawislak and Zipser (2010). The tracks are checked against the hovmollers in Figure 2.2 for accuracy (track represented by green lines). Using these tracks an AEW-relative framework is defined by centering a domain on the center of the analyzed track at any time. In this domain, we can then define locations at zonal and meridional distances from the trough.

MCSs are also manually tracked using maps of outgoing longwave radiation (OLR) and maximum radar reflectivity. The center of the MCS is analyzed as the strongest reflectivity within the OLR region and it's start and end points are defined in latitude and longitude and relative to the AEW. These are then checked against hovmollers of precipitation for accuracy (not shown). Whilst manually tracking these features is subjective, every effort was made to stay consistent with the above conditions. Further, the vorticity of the AEW and radar signatures of the MCSs are very difficult to track objectively using tracking algorithms since the features are extremely transient. Thus a manual approach was useful in the simulations, where it is possible with a relatively small sample size.

CHAPTER

3

MOIST CONVECTION IN THE AEW

In this chapter we focus on how the AEW influences moist convection; the research questions discussed in Section 1.7.1. This section is structured as follows. We first characterize the moist convection within the AEW envelopes in our control simulations to gain insight into the behavior of moist convection and how these characteristics relate to the AEW. With this information to guide us, we examine the AEW-relative spatial structure of factors that vary with the AEW and are conducive for moist convection. To do this we utilize both composite average AEWs in reanalyses and the tracked AEWs in our simulations. We then examine whether the thermodynamics of the AEW are driven by the AEW or a bi-product of the coupled convection. Finally, we combine the results of these previous sections to understand how the AEW may influence moist convective initiation and maintenance of mesoscale convective systems (MCSs). This multi-faceted approach allows us to understand the role of the synoptic-scale AEW in the variability of mesoscale convection. When discussing moist convection in this chapter, it is referred to as convection for brevity, not to be confused with dry convection which will not be discussed here.

3.1 Characteristics of Moist Convection

Most of the convection in our simulations can be characterized as MCSs with some degree of self-organization. We separate these MCSs into two different categories. The first is Quasi-Linear Convective Systems (QLCSs) that clearly exhibit an organization around a convective outflow (i.e. a cold pool) with a distinct line of deep moist convection present in simulated radar reflectivity. An example of such a convective system is MCS-2 in the 2010-CTRL simulation shown in Figure 3.1b or MCS-4 in the 2007 simulation shown in Figure 3.1a. The second is what we refer to as disorganized regions of moist convection that do not appear to organize around a convective feature, but tend to be organized into a concentrated area of deep moist convection by some other means, be it surface features such as orography, synoptic scale features such as the AEW trough, or some other means. An example of such convection is MCS-7 in the 2007-CTRL simulation shown in Figure 3.1a or MCS-8 in the 2010-CTRL simulation shown in Figure 3.1f. Table 3.1 summarizes 33 MCSs that occurred within the AEW wavelength (ridge to ridge) in the three simulations documented in Section 2.1.3.

From Table 3.1 we can see that there are between 8 and 15 distinct MCSs present within an AEW wavelength (in our three simulations). These occur over a period of 6-7 days, as the AEWs move across West Africa and the eastern Atlantic; the typical region of peak AEW intensity. A majority of these MCSs are QLCSs but 9 of the 33 MCSs are characterized as disorganized regions of deep moist convection. QLCSs are the predominant type of MCS over land (24 of 28 MCSs are characterized as a QLCS) while disorganized MCSs are the predominant type over ocean (5 of 5 MCSs are characterized as disorganized MCSs). This is consistent with the literature on the topic (e.g. Cifelli et al. 2010; Schwendike and Jones 2010; Janiga and Thorncroft 2014, 2016). When a mature QLCS transitions from land to ocean it typically retains it's linear structure for a while before dissipating (e.g. MCS-5 in Figure 3.1f). In some cases over land, the trough can favor MCSs that are disorganized (e.g. MCS-11 in Figure 3.1c or MCS-13 in Figure 3.1e). This appears to occur when there is a strong surface circulation associated with the AEW.

The MCSs in these simulations have ground relative speeds that vary from $3.3 m s^{-1}$ to $18.4\ m s^{-1}$ with an average of $11.8 m s^{-1}$. This is consistent with the distribution of observed MCSs shown in Laing et al. (2008) (specifically in their Figure 13). This indicates that our simulated MCSs exhibit similar characteristics to those observed by satellite, giving us confidence in the realism of these simulations. The direction of MCS motion has a westward component in all except 1 of our 33 MCSs. This is consistent with the typical

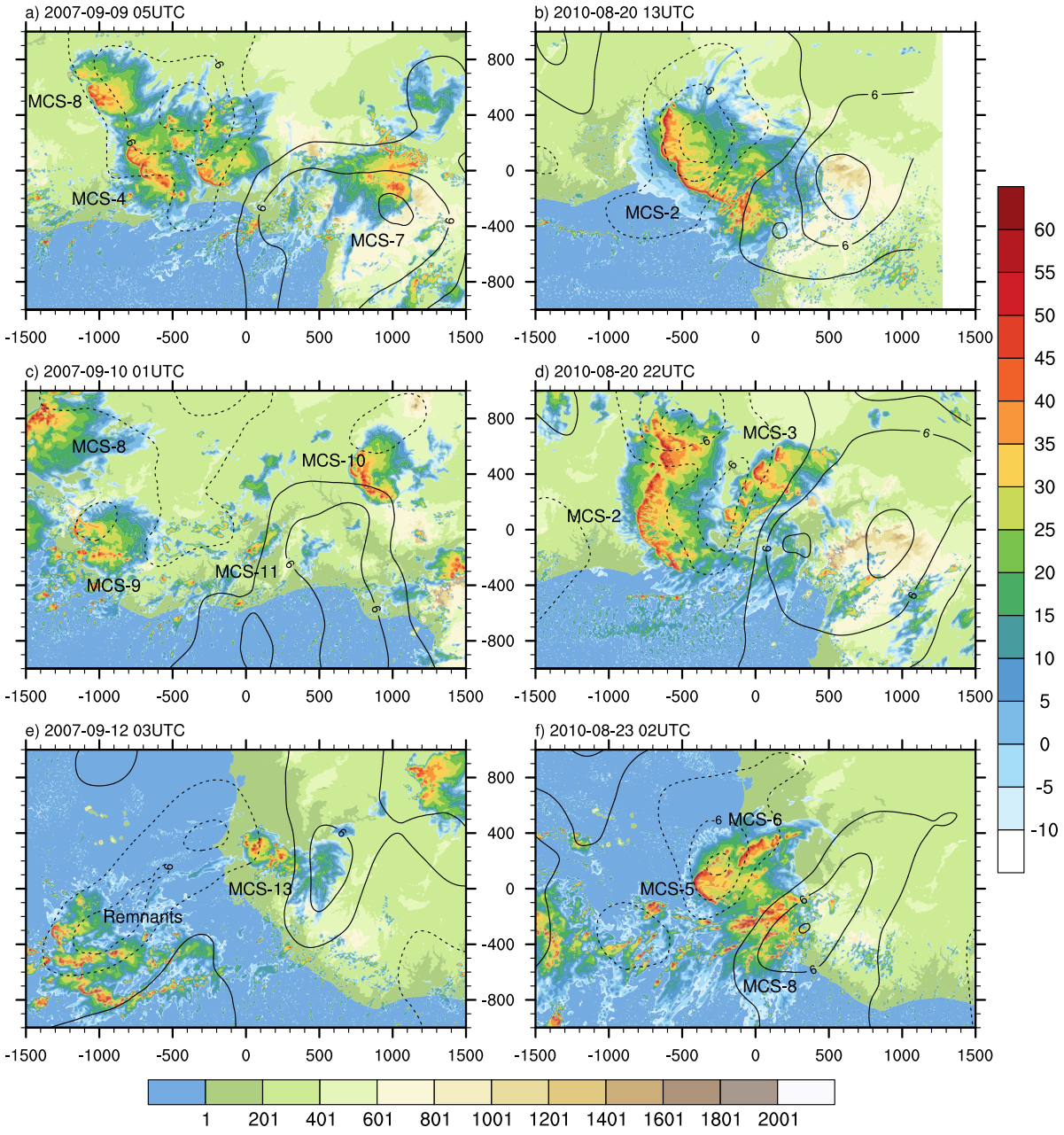

Figure 3.1: AEW-relative maps of terrain (m; earth colored shades), simulated radar reflectivity (dBz; rainbow shades), and perturbation meridional wind (ms^{-1}; contours) at various times in the a,c,e) 2007 simulation and b,d,f) 2010 simulation. Axes are in km from the AEW trough.

Table 3.1: Summary of MCSs. L = Land, O = Ocean. Duration is in hours. Speed is in ms^{-1}. Direction of motion is given by compass abbreviation (e.g. westward motion is W).

MCS	Date & Time	(UTC)	Duration	Surface	Structure	Spd.	Dir.
	Start	End					
2007-1	9/07 11Z	9/08 19Z	32	L	QLCS	12.5	SW
2007-2	9/07 15Z	9/08 10Z	19	L	QLCS	15.1	SW
2007-3	9/07 14Z	9/08 13Z	23	L	QLCS	8.5	WSW
2007-4	9/08 11Z	9/09 21Z	31	L	QLCS	15.2	WSW
2007-5	9/08 14Z	9/09 17Z	27	L	QLCS	9.7	WSW
2007-6	9/08 15Z	9/10 00Z	33	L	Disorganized	9.1	W
2007-7	9/08 17Z	9/09 12Z	19	L	Disorganized	3.3	N
2007-8	9/08 16Z	9/10 10Z	42	L	QLCS	13.7	W
2007-9	9/08 23Z	9/10 09Z	34	L	QLCS	15.4	WSW
2007-10	9/09 13Z	9/11 21Z	56	L	QLCS	18.4	W
2007-11	9/09 12Z	9/11 12Z	44	L	Disorganized	6.8	WNW
2007-12	9/10 15Z	9/12 16Z	49	L to O	QLCS	12.6	WSW
2007-13	9/11 13Z	9/12 10Z	23	L	Disorganized	7.7	NW
2007-14	9/11 14Z	9/13 13Z	47	L	QLCS	14.5	W
2007-15	9/13 19Z	9/14 11Z	16	O	Disorganized	5.6	W
2010-1	8/19 09Z	8/22 02Z	65	L	QLCS	16.4	W
2010-2	8/19 00Z	8/20 02Z	26	L	QLCS	10.9	SW
2010-3	8/20 17Z	8/21 10Z	21	L	QLCS	17.5	W
2010-4	8/21 16Z	8/22 12Z	20	L	QLCS	17.8	W
2010-5	8/22 00Z	8/23 12Z	36	L to O	QLCS	15.3	W
2010-6	8/22 23Z	8/23 10Z	35	L to O	QLCS	12.4	WSW
2010-7	8/23 22Z	8/24 10Z	12	O	Disorganized	9.2	NW
2010-8	8/23 22Z	8/25 17Z	39	O	Disorganized	5.2	WSW
2017-1	8/04 12Z	8/05 17Z	30	L	QLCS	9.5	WSW
2017-2	8/04 12Z	8/06 06Z	42	L	QLCS	15.5	W
2017-3	8/04 15Z	8/06 06Z	39	L	QLCS	13.5	W
2017-4	8/05 11Z	8/06 21Z	34	L	QLCS	10.2	WSW
2017-5	8/05 23Z	8/06 20Z	20	L to O	QLCS	9.6	W
2017-6	8/06 13Z	8/06 22Z	9	L	QLCS	9.9	W
2017-7	8/06 21Z	8/06 10Z	13	L	QLCS	14.6	WNW
2017-8	8/07 19Z	8/08 13Z	18	L	QLCS	13.3	WSW
2017-9	8/06 13Z	8/08 01Z	35	O	Disorganized	12.2	W
2017-10	8/08 02Z	8/09 14Z	37	O	Disorganized	8.3	W

easterly background flow acting as the main steering current for MCSs (e.g. see Figure 4.2).

These simple statistics tell us a number of different things about the AEW and it's relation with moist convection. First, the fact that multiple MCSs exist within the AEW envelope indicates that the AEW cannot simply be characterized as a vorticity signature of one MCS, nor is there just a single MCS coupled to a specific phase of the AEW. Further evidence for this is in the duration of MCSs. These vary between 9 and 65 hours, all shorter than the lifetime of the AEW. Therefore any systematic interaction between the AEW and moist convection occurs because of the action of multiple MCSs, as is the case in many tropical synoptic scale systems (e.g. Mapes et al. 2006). Second, the difference in the number of MCSs within each AEW shows that the behavior of moist convection is not consistent between AEWs. For a 2 day period, the 2010 case is dominated by a single large QLCS that appears to suppress other convective activity (e.g. Figure 3.1b). Other MCSs only form once the large MCS propagates far enough ahead of the northerlies and trough (e.g. Figure 3.1d). Meanwhile, over the same region of West Africa, the 2007 AEW has multiple smaller MCSs present at the same time (Figure 3.1a). Thus, there is clearly no consistent behavior as to the size and number of MCSs in an AEW.

3.2 MCS Characteristics Relative to the AEW

Table 3.2 expands on Table 3.1 by relating the MCSs to the AEW. The second column shows the phase or phases of the AEW that each MCS spends time in. 20 of the 33 MCSs only spend time in the trough and/or northerlies. A further 7 MCSs spend some part of their lifetime in those phases, leaving only 6 MCSs that do not spend any time in the northerlies or trough. This table therefore highlights the fact that MCSs are more prevalent in the northerlies and trough than the southerlies and ridge. Further, the average duration of AEWs in the northerlies and trough in these simulations is around 30 hours. While there are too few MCSs in the southerlies or ridge in our simulations to compute an accurate average for duration of MCSs, we can compare this number to the typical diurnal cycle and past literature. Laing et al. (2008) examined the duration of MCSs in this region of Africa, finding the average to be less than those in our study, around 25 hours. Further this 30 hour duration is obviously much larger than an MCS tied to a typical diurnal cycle. The increased lifespan of MCSs in these phases of AEWs therefore hints at some mechanism for enhanced maintenance of MCSs.

There is evidence that the AEW phase influences meridional MCS motion. 13 of the

Table 3.2: Summary of MCSs relative to AEW. AEW phase is given with the following abbreviations; T = Trough, R = Ridge, S = Southerlies, N = Northerlies. Positive zonal motion is faster than the AEW trough (ms^{-1}). Positive meridional motion is moving northward relative to the AEW (ms^{-1}).

MCS	Phase(s)	AEW Rel. Zonal Spd.	AEW Rel. Meridional Spd.
2007-1	N	0.0	-8.8
2007-2	N	2.8	-5.6
2007-3	T	-2.1	2.1
2007-4	N,R	2.7	-5.4
2007-5	N,T	-3.1	-6.2
2007-6	N,T	-1.7	-2.5
2007-7	S	-7.3	4.4
2007-8	N,R	4.7	0.0
2007-9	N,R	9.0	-5.7
2007-10	S,T,N	9.7	-4.9
2007-11	T	-1.3	-0.6
2007-12	N,R	3.4	-5.1
2007-13	T	-2.4	6.0
2007-14	R,S,T	8.3	1.8
2007-15	T	0.0	1.7
2010-1	T,N	4.5	-1.5
2010-2	T	-6.9	-10.4
2010-3	T,N	-1.3	-5.3
2010-4	N,R	11.1	-16.6
2010-5	T,N	3.9	-3.9
2010-6	T	1.6	-7.9
2010-7	T	0.0	4.6
2010-8	T	1.6	1.1
2017-1	T	0.0	
2017-2	S,T,N	4.7	
2017-3	N	2.1	
2017-4	R,S	0.0	
2017-5	N	-4.2	Not
2017-6	S	-6.2	Recorded
2017-7	S	2.1	
2017-8	R,S	7.7	
2017-9	N	0.8	
2017-10	S	-0.8	

MCSs exhibit a southward component to their motion, with 11 of these in the trough or northerlies. Further, of the 5 MCSs that have a northward component to their motion, 2 are in the southerlies, and the other three are disorganized MCSs coupled to the trough as it moves northward. To better understand MCSs relative to the AEW we tracked their AEW relative motion (columns 3 and 4 of Table 3.2). The meridional motion relative to the AEW is, similar to the northward and southward motion of the MCS, related to the AEW phase. A majority of the QLCS MCSs in the northerlies move southward relative to the AEW, with two of those in the southerlies moving northward relative to the AEW. Disorganized MCSs in the trough have relatively small AEW-relative meridional motion since they appear to be coupled to the AEW (MCS 2007-11 for example). On examination of the zonal relative motion, 14 MCSs have relative zonal speeds at least $2ms^{-1}$ faster than the AEW, 7 MCSs have relative zonal speeds at least $2ms^{-1}$ slower than the AEW, and 12 MCSs have relative zonal speeds within $2ms^{-1}$ of the AEWs. While a fraction move with the AEW, this clearly indicates that the majority of MCSs are not coupled to a certain phase of the AEW, and that they obey their own dynamics.

A key point to glean here is that the AEW is not simply coupled to a single MCS. Neither is there a region of cloud that is fixed in a single phase of the AEW. This is in contrast to the canonical model for DRWs, which typically generate broad regions of moist convection through upslope isentropic motion in a specific phase. Instead, the AEWs control on moist convection is more complex since multiple individual MCSs, that obey their own dynamics, are present in an AEW. This leads to the idea that precipitation is favored in the northerlies or trough through preferential initiation and/or maintenance of MCSs. Such a convective coupling is more similar to the mechanisms proposed for stratiform instability. In stratiform instability Mapes (2000) proposed that convective coupling occurred through a process of convective inhibition (CIN) removal and convective available potential energy (CAPE) build up, while Kuang (2008) showed that the coupling is driven more by moisture convergence. In both cases these processes promote the proliferation of MCSs. In AEWs we also have adiabatic forcing for ascent as a potential mechanism to support the initiation of MCSs. In the next section we will therefore assess which factors that support initiation and maintenance of MCSs, are present in the AEW.

3.3 Controls on Moist Convection

As documented by Kiladis et al. (2006), Janiga and Thorncroft (2016), and Tomassini et al. (2017) the AEW typically exhibits a variety of factors including quasi-geostrophic-like forcing for vertical motion, shear, temperature, and moisture variations that lead to factors like enhanced CAPE (see Figure 1.3). Here we review these forcings and introduce others present in composite average ERAI and CFSR AEWs first, and then in the 2007 and 2010 simulations.

3.3.1 Over Land

Figures 3.2a-c and 3.3a-c show AEW-scale TRMM precipitation and meridional winds in composite ERAI and CFSR AEWs. Over East Africa, the peak precipitation slightly leads the peak northerlies in both ERAI and CFSR. Over West Africa the peak precipitation slightly lags the peak northerlies in ERAI but is directly in phase with the northerlies in CFSR. Nearly all the AEW-scale precipitation falls between 5-15°N. Thus our focus on convective parameters will be on how moist convection is enhanced in the northerlies, suppressed in the southerlies, and which factors are of considerable magnitude between 5-15°N.

Convective Inhibition (CIN)

Figures 3.2e,f and 3.3e,f show AEW-scale convective inhibition (MCIN) associated with the maximum value of CAPE (MCAPE) in the column. For CIN, there is significant disagreement between ERAI and CFSR. Over East Africa in ERAI, CIN anomalies are very small, not exceeding 8 J/kg on average, but in CFSR, are larger and typically situated in the ridge. Over West Africa in ERAI, CIN is strongest (south of 15°N) in and to the east of the ridge, while in composite CFSR AEWs, CIN peaks in the northerlies. Nonetheless it seems that, with the exception of over East Africa in ERAI, there is significant CIN slightly leading the peak in precipitation. This suggests that the decay of anomalously high values of CIN in the AEW may be important for moist convection.

Vertical Motion

These Figures also show 1000-700 hPa AEW-scale vertical motion. In the 1000-700 hPa layer, where isentropes are strongly sloped (e.g. see Figure 4.2), vertical motion represents adiabatic ascent, as has been shown by Kiladis et al. (2006) and Janiga and Thorncroft (2016). Ascent (negative values of ω) is strongest between the peak of the northerlies and

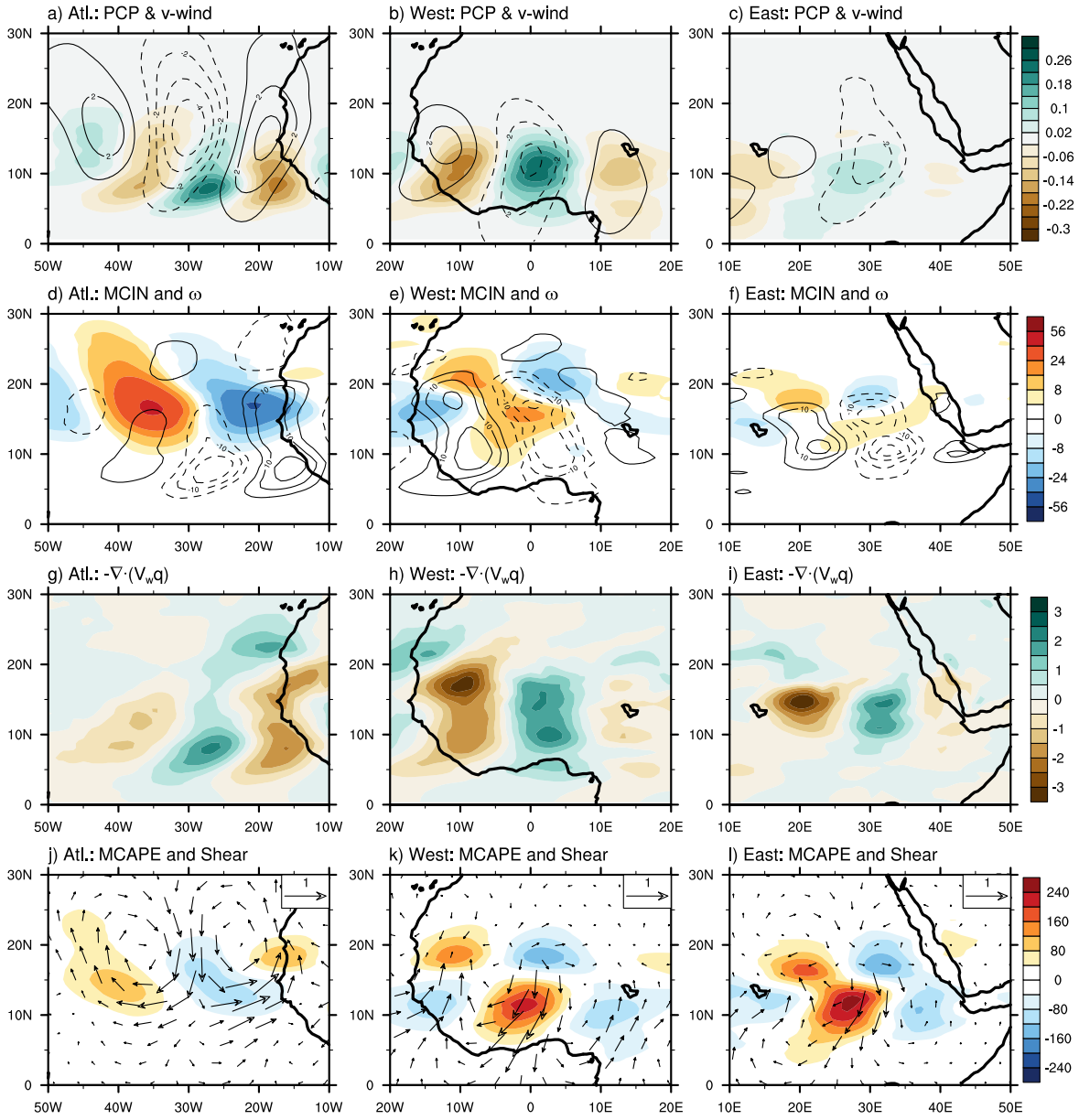

Figure 3.2: Composite average ERAI a,b,c) precipitation rate (mm/hr; shaded) and 650hPa meridional winds (ms^{-1}; contours), d,e,f) maximum CIN (J kg^{-1}; shaded) and 1000-700hPa vertical motion (hPa day^{-1}; contours), g,h,i) 1000-700hPa moisture flux convergence (g kg^{-1} day^{-1}) and 2m temperature (K; contours), and j,k,l) maximum CAPE (J kg^{-1}; shaded) and 1000-700hPa shear vectors (ms^{-1}). Figures are for base points in the a,d,g,j) Atlantic, b,e,h,k) West Africa, and c,f,i,l) East Africa.

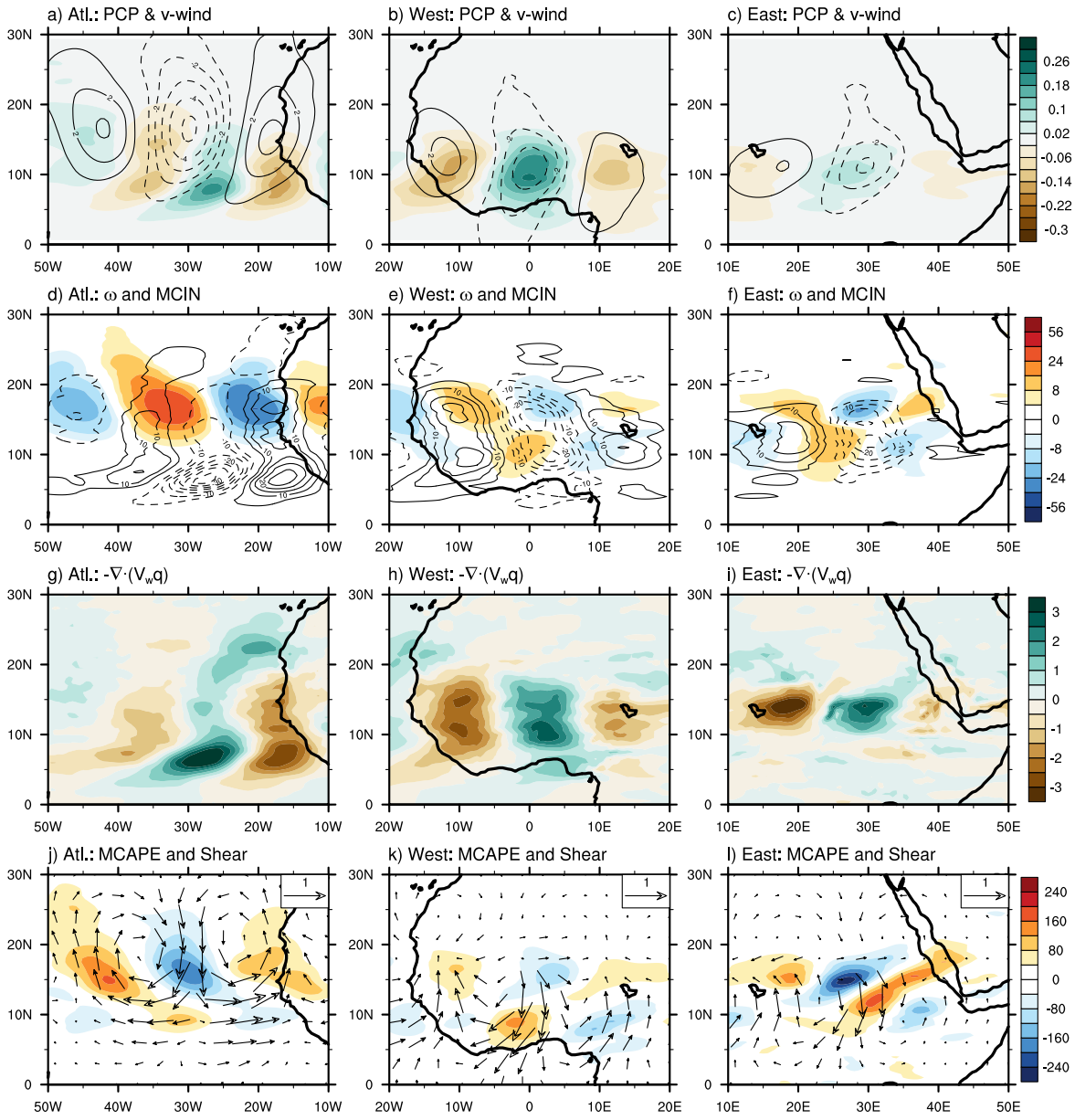

Figure 3.3: As in Figure 3.2 but for CFSR.

the trough. Thus the peak ascent tends to lag the peak precipitation slightly in both ERAI and CFSR. Further the ascent is not particularly large in magnitude, with rising motion of no more than 30 hPa per day. Given that the average LFCs are 2-3km (approximately 800-700 hPa) and there is no variability in LFC height with the AEW (not shown), adiabatic ascent is not sufficient to initiate surface based convection alone. This may indicate that ascent is not as important for convection as other factors. Alternatively it may simply be that only a small amount of anomalous rising motion is required to support other factors in raising parcels to their LFC. We will discuss this more in section 3.5.

Moisture

Another factor that can play a role in the initiation and maintenance of convection is moisture convergence. Increased low-level moisture can decrease the amount of dry air entrainment for a rising plume, allowing parcels to maintain positively buoyant, moist ascent for longer (e.g. Markowski and Richardson 2011, section 7.3, pages 195-196). Figures 3.2h,i and 3.3h,i show the moisture convergence, calculated as the specific humidity flux convergence by the AEW-scale winds, for composite AEWs in ERAI and CFSR respectively. Using AEW-scale horizontal winds allows us to assess the moisture convergence due to the AEWs flow only.

The moisture convergence closely follows the ascent by slightly lagging the northerlies and precipitation in both reanalyses. Over West Africa, as with ascent, the moisture convergence lags the northerlies and precipitation more to the south than to the north. This may again favor earlier initiation to the north. While it seems that this lag in ascent and moisture convergence relative to precipitation would indicate that these factors are less important for precipitation, this is likely not the case. In fact, given that over half of MCSs in our simulations have a positive zonal motion relative to the AEW (Table 3.2), if we assume these factors support convective initiation (CI), then we would expect these factors to lag precipitation. More explicitly, MCSs on average propagate faster than the AEW, and thus will produce precipitation in a location relative to the AEW, that is westward of where they were initiated relative to the AEW. This may be an indication that these two factors are most important in supporting CI in the AEW.

Convective Available Potential Energy

The availability of CAPE to maintain vigorous buoyant motions once parcels have reached the LFC is essential for CI and the maintenance of MCSs. Figures 3.2k,l 3.3k,l show AEW-scale

MCAPE anomalies. CAPE varies significantly between the two datasets. Over East Africa CAPE anomalies are around 250 Jkg^{-1} in ERAI and co-located with the peak in precipitation, but in CFSR CAPE anomalies are weaker and lag the precipitation. Due to this variability between reanalyses, it is therefore difficult to judge the role of the AEW in CAPE modulation.

Over West Africa, between 5-15°N the strongest CAPE anomalies are in and just to the west of the northerlies which slightly leads the precipitation. The magnitudes vary considerably between ERAI and CFSR though. Considering the time-mean MCAPE is around 1000 Jkg^{-1} over West Africa (not shown), in ERAI this equates to time-mean MCAPE in the northerlies of 1200 Jkg^{-1} as opposed to 800 Jkg^{-1} in the southerlies. In CFSR this equates to 1100 Jkg^{-1} in the northerlies and 900 Jkg^{-1} in the southerlies. These anomalies therefore produce a 20-50% difference between the AEW phases. While the two reanalyses are quite different, even a 20% increase in CAPE could support stronger moist convection. Therefore it is expected that this variability in CAPE will play a significant role in manipulating moist convection between AEW phases.

Wind Shear

Figures 3.2k,l and 3.3k,l also show 1000–700-hPa AEW-scale wind shear vectors. We focus on the low-level shear here since there is little basic state shear above 700 hPa, except over East Africa where the tropical easterly jet (associated with the Asian monsoon) is strong and extends over Africa. In addition, the AEW-scale mid and upper-level shear is relatively small (not shown). The AEW exhibits an increased shear of 1 ms^{-1} 100 hPa^{-1} in the south to south-westward direction where the peak anomalous precipitation is present. As shown in Table 3.1, MCS motion in the northerlies is most often to the WSW. Since the overall shear magnitude is typically around 3 ms^{-1} 100 hPa^{-1} in the westward direction, it's expected that in the northerlies, the AEW adds a relatively large amount of shear in the typical direction of motion for MCSs. In contrast, anomalous shear in the southerlies is toward the north or north-east. In the southerlies, the AEW will therefore reduce the shear in the typical direction of MCS motion.

3.3.2 Over Ocean

Over ocean, these factors are quite different. Precipitation extends further to the north, but with a peak further south, between 5°N and 10°N (Figures 3.2a and 3.3b). Further, the precipitation peaks in the trough, rather than in the northerlies. Precipitation over ocean is directly in phase with moisture convergence and ascent. In this case, there is little adiabatic

ascent over the ocean since isentropes are not strongly sloped (Janiga and Thorncroft 2016). Thus the ascent pattern here is likely due to low-level convergence in the trough and divergence in the ridge. CIN tends to be small where the precipitation is strong over the ocean but is large between 15°N and 20°N where there are small precipitation anomalies. Thus it may play some role to the north but it plays little role overall. Over ocean, CAPE anomalies are out of phase with the precipitation and given that convection is typically disorganized and coupled to the AEW trough, it's not expected that enhanced CAPE in other phases of the AEW will have a role in enhancing the precipitation.

This analysis highlights that moisture convergence and ascent are the key factors for forcing moist convection over the ocean in the AEW, consistent with past studies such as Janiga and Thorncroft (2016). Other factors affecting moist convection such as the level of free convection, surface temperature, and surface moisture do not exhibit statistically significant anomalies over ocean or land.

3.3.3 Simulations

In the next sections we will further examine individual MCSs to understand if some of the factors connected to the AEW are enhancing those MCSs. First though we need to know that our simulations are producing similar variability of these convective factors to what was seen in the composite AEWs.

Figures 3.4 and 3.5 show these convective factors for the 2007 and 2010 case studies, averaged over the first 3 days of the AEWs track, while over land. In our simulations, much like in Figures 3.2b and 3.3b, precipitation is primarily in the northerlies, while the southerlies tend to be dry. While it is difficult to judge a number of the factors in our convection resolving simulations due to the fact that we have active convection in our simulations, most convective factors match those in the composite AEWs from the reanalyses. CIN, upward ascent, and moisture convergence all have peaks in the northerlies. Similar to ERAI, CIN perturbations are all on the northern side of the AEW. Further there is sinking motion and dry air convergence in the southerlies. Further CAPE is largest ahead of the northerlies, while it is lowest in and to the east of the trough. Shear is southwestward in the northerlies, while it is toward the northwest in the southerlies. These all match the composite AEWs reasonably well.

These analyses confirm that we have a number of factors, including CIN, low-level vertical motion, and low-level moisture convergence that will likely favor CI in the northerly phase of the AEW. In addition, enahnced CAPE indicates a favorable environment for the

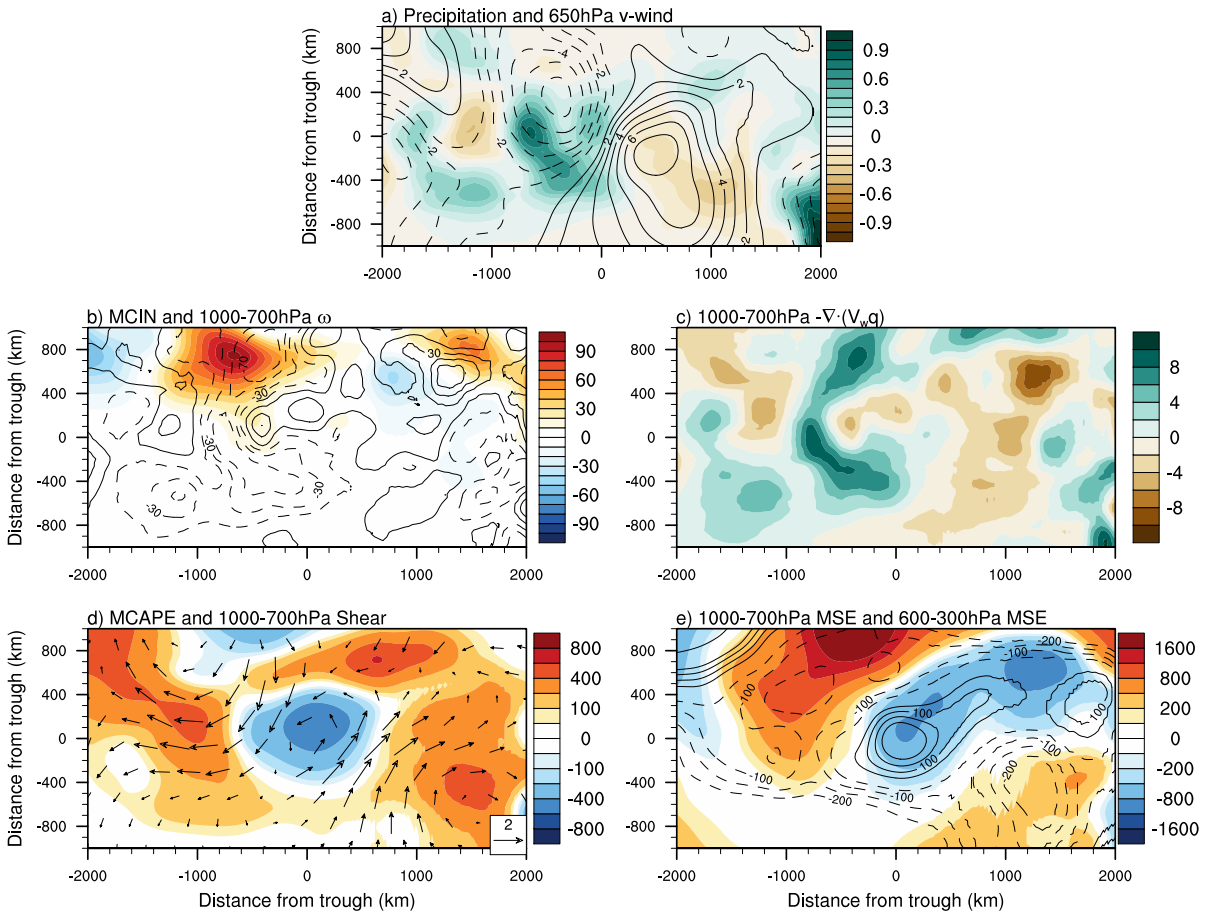

Figure 3.4: Horizontal cross-sections of perturbation variables affecting moist convection, following the 2007 AEW for the first three days of it's track (the period it is over land). Axes are zonal and meridional distance (km) from analyzed vorticity center. Variables are a) precipitation (mm/hr; shaded) and 650hPa meridional wind (ms^{-1}; contours), b) maximum CIN (Jkg^{-1}; shaded) and 1000-700hPa average vertical motion (hPa day^{-1}; contours), c) 1000-700 specific humidity flux divergence (g kg^{-1} day^{-1}), d) maximum CAPE (Jkg^{-1}; shades) and 1000-700hPa vertical shear vectors ($ms^{-1}100hPa^{-1}$; vectors), and e) 1000-700hPa average MSE (J; shades) and 600-300hPa average MSE (J; contours).

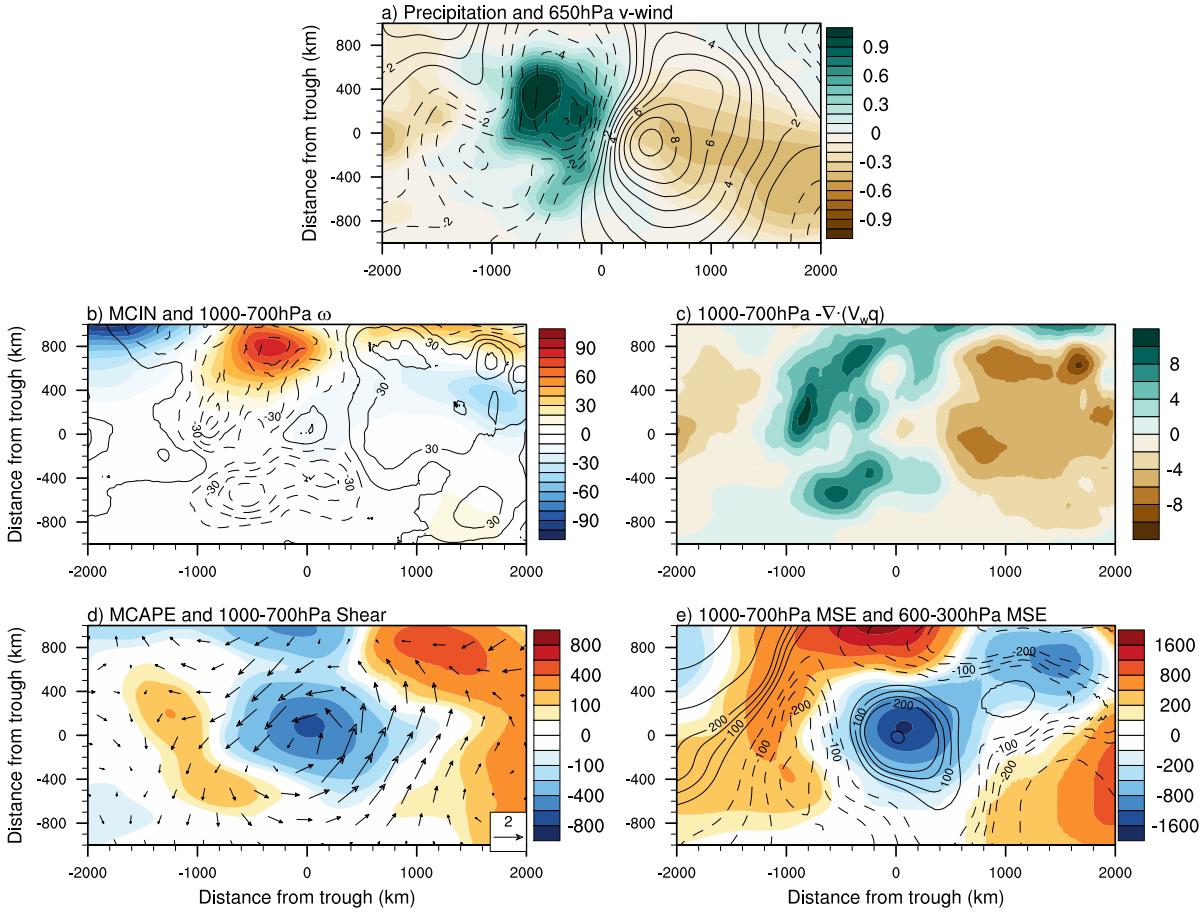

Figure 3.5: As in Figure 3.4 but for the 2010 AEW.

initiation and maintenance of the AEW in the northerlies. Further, there is an enhancement of shear that may help to support the continued maintenance of MCSs along the cold pool edge in the northerlies. These factors are all present in the composite AEWs, as well as in AEWs in our high resolution simulations.

3.4 What controls the distribution of CAPE and CIN?

As discussed in the introduction (Section 1.7.1) the temperature and moisture fields in the AEW could be a result of the AEW itself or a biproduct of the coupled convection. To understand whether these fields support moist convection, we therefore need to answer this question. To do this, we examine moist static energy (MSE) defined as:

$$h = c_p T + gZ + l_v q \tag{3.1}$$

where c_p is the specific heat at constant pressure, T is the temperature, g is gravitational acceleration, Z is geopotential height, l_v is the latent heat of vaporization, and q is the specific humidity. MSE is a useful measure to understand the temperature and moisture fields in the AEW since it encompasses the energy from both. Further it is analogous to equivalent potential temperature which is often used to understand the combined effects of temperature and moisture in convective situations. Figure 3.6 shows the vertical structure of AEW-scale MSE. Over land, MSE is tilted eastward with height such that in the low-levels of the northerlies, there is high MSE and in the mid-to-upper levels, there is lower MSE.

We examine the flux convergence of MSE by AEW winds to gauge whether the MSE structure is a product of the AEWs dynamics. Here we can see that, to first order, differential advection by the AEW-scale winds control the vertical structure of MSE. At most levels, flux convergence of MSE is in quadrature with the AEW-scale MSE. Due to a change in the background gradient of MSE over land (not shown) the flux convergence of MSE flips sign around 700 hPa, controlling the vertical tilt of MSE. The only exception to this is in the low-levels over the Atlantic. Here it is expected that the low-levels are driven more by surface fluxes and convective processes than the horizontal advection, therefore driving the change to a more vertically stacked column. Further evaluation of the MSE is not in the scope of this study but a full MSE budget (not shown) does confirm that horizontal advection is the main driver of temperature and moisture fields in the AEW.

This MSE structure explains the increase in CAPE in and ahead of the northerlies, as shown in the sub-figures. Further, weaker MSE anomalies in CFSR explain the weaker

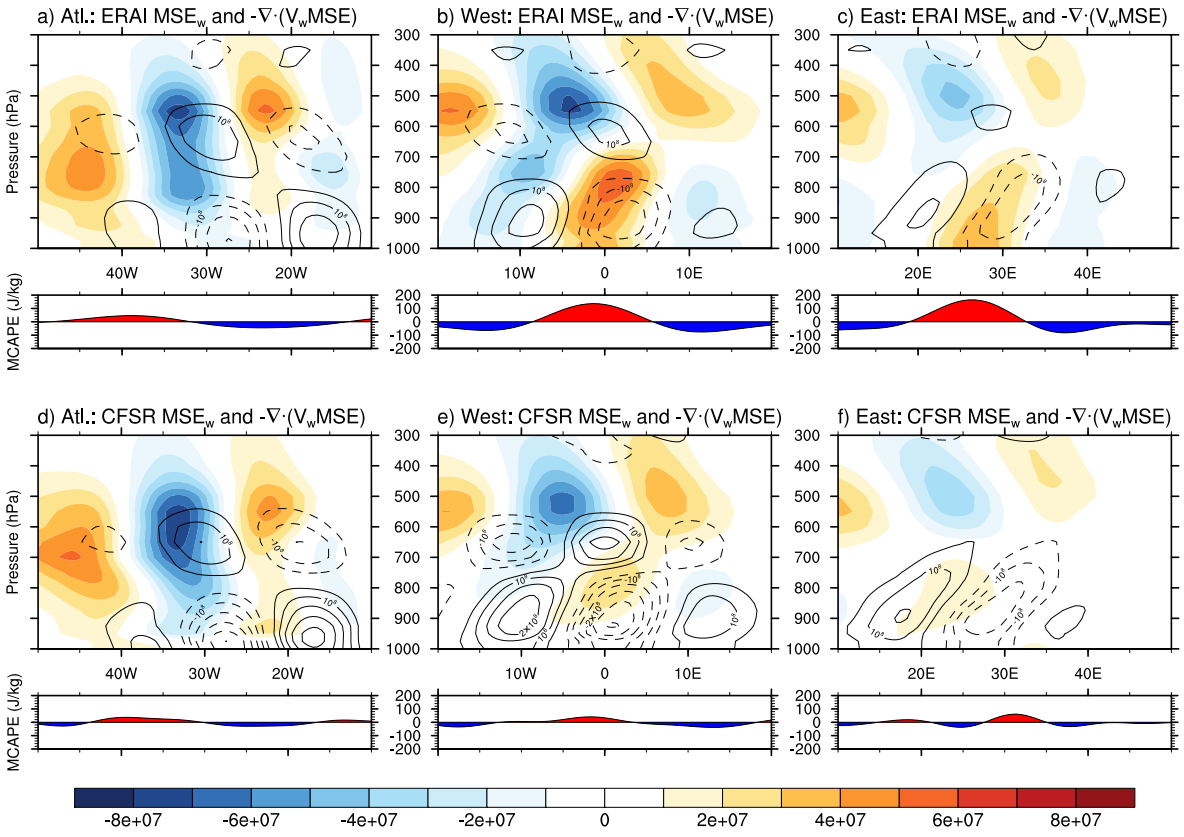

Figure 3.6: 5-15°N averaged vertical profiles of composite AEW-scale MSE (J; shades) and flux convergence of MSE due to AEW-scale winds (J day^{-1}; contours) for a-c) ERAI and d-f) CFSR. Base points are a,d) Atlantic, b,e) West Africa, and c,f) East Africa. The corresponding 5-15°N averaged AEW-scale MCAPE is also shown below each figure.

CAPE anomalies there. MSE anomalies also explain the increase in CIN, with higher MSE anomalies above the surface than at the surface. Thus CAPE, CIN, and moisture variations are all a product of the AEW and they may act to enhance moist convection.

3.5 Moist Convective Initiation in the AEW

In this section we discuss if and how the initiation of moist convection relates to the AEW. We investigate how the location and timing of CI relates to the AEW, what factors caused the CI for each MCS in our simulations, and what factors the AEW may have varied to influence the initiation of moist convection.

Figure 3.7 shows the local time of CI for all MCSs surveyed in the simulations. 13 of the 21 MCSs surveyed had CI occur between noon and 4pm, correlating with the peak heating. The other 8 MCSs surveyed had CI occur between 6pm and midnight locally. This indicates that MCSs only develop and CI only occurs in conjunction with the diurnal cycle. If the AEW were the main factor controlling the timing of CI, we would expect to see a wider distribution of CI times throughout the day. Thus the CI time is primarily coupled to the diurnal cycle, not the AEW.

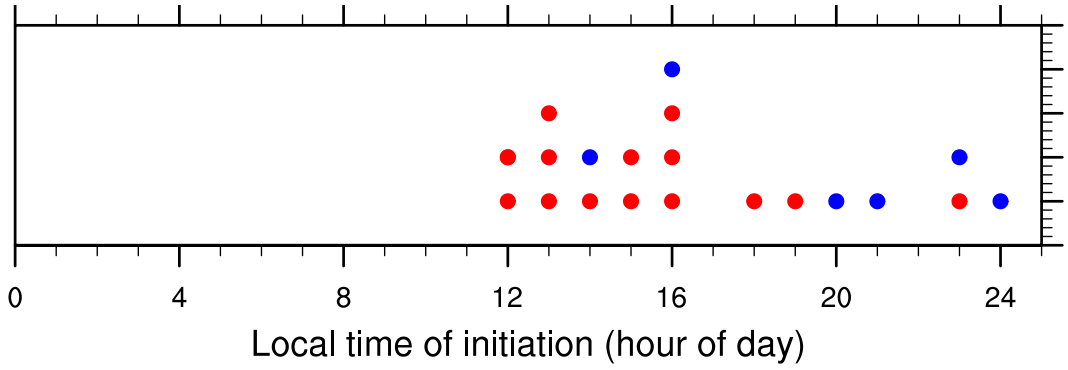

Figure 3.7: Local time of initiation (hour of the day) of MCSs documented in table 3.1. Red dots are MCSs from the 2007 simulation. Blue dots are MCSs from the 2010 simulation.

However, on examination of the AEW-relative location of CI, there is a clear preference for the northerlies and trough. Figures 3.8a and 3.8b show the relative location of MCS initiations in the 2007 and 2010 AEW simulations. It's clear that there is a higher density of MCS initiations in the northerlies and trough than in the southerlies or ridge. The only

exceptions to this are three MCSs that form in the southerlies of the 2007 AEW. The first of these is a disorganized MCS that formed in association with the Cameroon highlands (MCS 2007-7). An inspection of this case (Table 3.3) indicates that the only factor supporting moist convective initiation here was low-level ascent. Thus it's likely that CI here was associated with orographic lifting, and not a factor affected by the AEW. The other two MCSs form in the afternoon as CIN was overcome by surface warming and confluence at the edge of the Saharan air layer (SAL). Given the prevalence of other forcing mechanisms for CI, it's likely that these three cases are simply instances where the forcing mechanisms in question overcame suppressing factors such as drier air and descent brought on by the AEW.

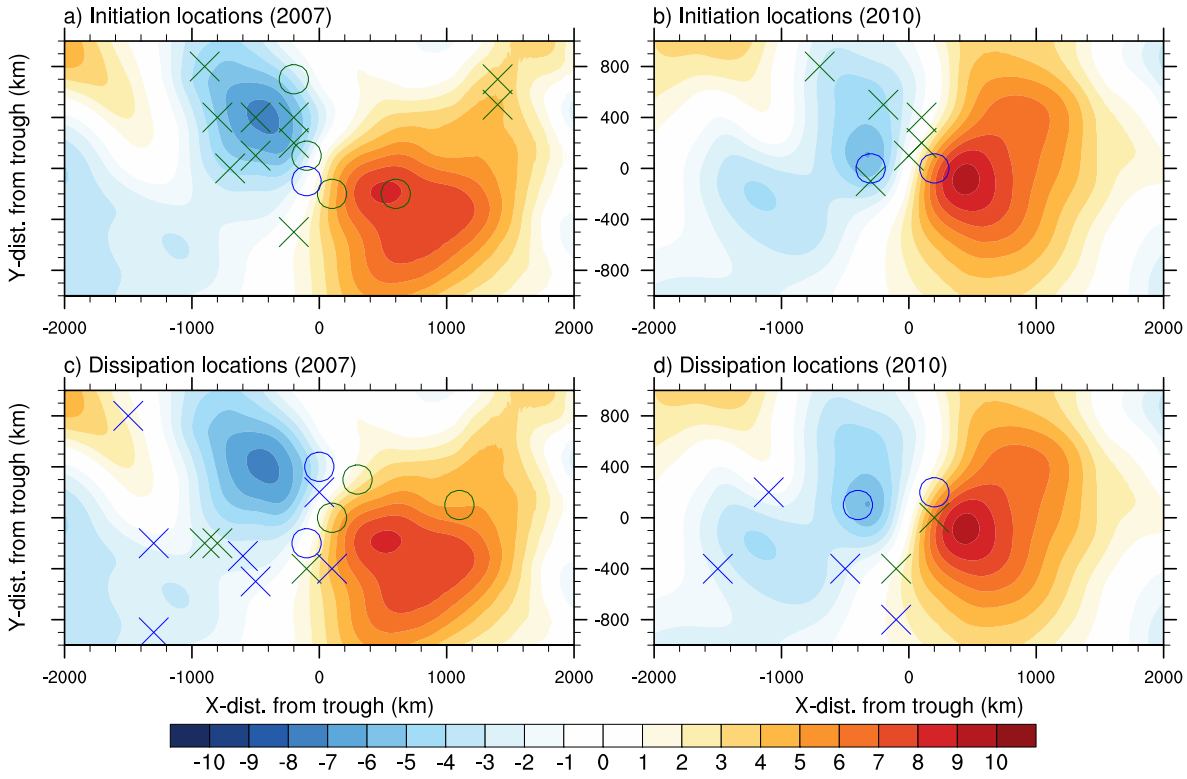

Figure 3.8: Cross-sections of AEW-relative average 650-hPa meridional winds (ms^{-1})with initiation and dissipation locations of MCSs overlaid. Crosses represent QLCSs, circles represent disorganized convection, green is over land, blue is over ocean.

To diagnose the specific factors involved in CI, a number of variables are averaged over a 2°x2° area surrounding the location of initial moist convective activity for each MCS. These variables include the 2 m temperature tendency, MCIN tendency, and the dew

point temperature tendency and vertical motion in the lowest five model levels. These are averaged over periods 6 hours prior to moist convective initiation to understand why moist convection initiated at that time. Further, maps of low-level temperature and dew point are examined and compared to the simulated maximum radar reflectivity to identify the presence of surface boundaries such as convective outflows from other MCSs or the edge of the Saharan Air Layer (SAL). Simulated maximum radar reflectivity is also compared to the terrain height (e.g. Figure 3.1) to identify if orographic lifting or an elevated heat source played a role. Finally, we examine average soundings in those 2x2° areas to verify the processes diagnosed using the maps and average tendencies. This combination of tools allows the diagnosis of a variety of factors involved in moist convective initiation.

To demonstrate this process we focus on MCS-4 from the 2007 simulation. The map at top-right of Figure 3.9 shows the terrain and simulated radar reflectivity as the moist convection associated with MCS-4 is initiating. This new moist convection can be seen between 11°N and 12°N, and 7°E and 8°E (the area encompassed by the red box). This is associated with the edge of high terrain near the Jos Plateau. Further, from a map of the 2m temperature field at the same time we can see that this also forms in association with the edge of the cold wake from MCS-1. Between 10°N and 12°N there is much colder air in the region when compared to other longitudes. Thus we can see that this MCS forms in association with both elevated terrain and outflow from a previous MCS.

On examination of the temperature and moisture profiles in the skew-T log-P diagrams in Figure 3.9, we can see that there has also been a moistening below 700 hPa relative to the day before. While this moistening may be partly due to the outflow from the previous MCS, this is also influenced by the moistening due to the AEW, since this is consistent with the typical moisture tendency in the northerlies (e.g. Figure 3.4). Finally, there is also some minor warming below 800hPa relative to the day before. Combined with the low-level moistening, this allows the parcel to overcome the capping inversion present at the same time the day before. Further, this combination lowers the LCL and LFC making it easier for moist convection to initiate. This examination of MCSs is repeated for 20 other MCSs to diagnose reasons for moist convective initiation.

Table 3.3 documents the factors likely to have supported initiation in the case of each MCS. In 13 of the 21 cases, surface warming (due to diurnal heating) overcoming the CIN was a primary factor in the initiation of moist convection. 8 cases exhibited notable moistening and 7 cases exhibited ascent; two of the main factors diagnosed in the previous section as having significant variability due to the AEW. Further, 19 of the 21 cases had either significant terrain or a surface boundary present. Terrain acted as either an elevated heat

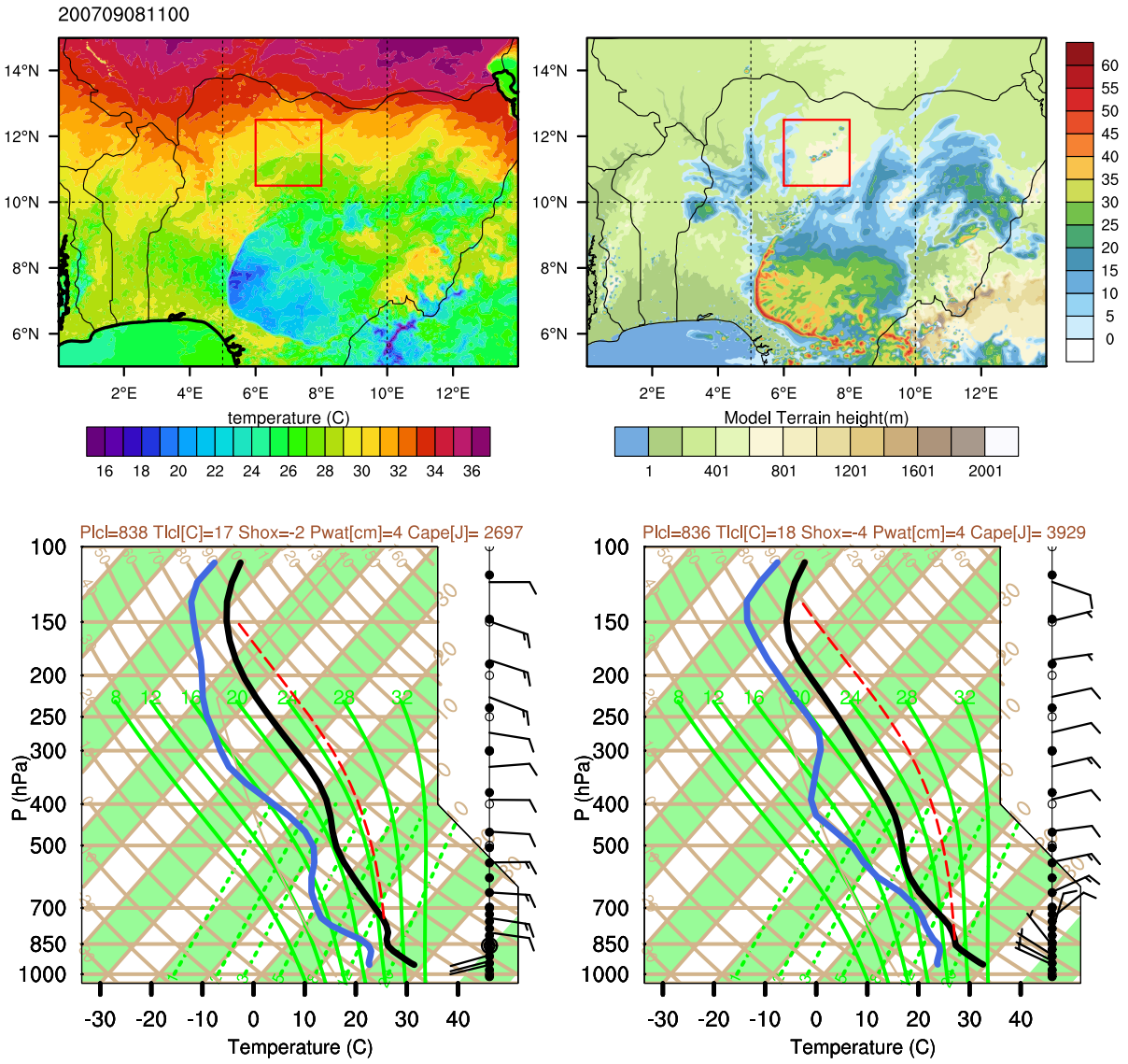

Figure 3.9: Maps and skew-T diagrams focusing on the initiation of MCS-4. Top-left shows the 2m temperature field at 2007/09/08 11UTC (the time of initiation). top-right shows the terrain and simulated radar reflectivity fields at the same time. The red box shows the region where CI is occurring. The two skew-T log-P diagrams show the environment in the red box 24 hours before initiation (bottom-left) and at the time of initiation (bottom-right).

source or as orographic lift, and was a factor in 8 cases. Previous MCS outflows were present in 7 cases, typically acting as a lifting mechanism to raise parcels to their LFC. The SAL boundary appeared to be a factor in a further 7 cases, acting similarly to a dry line (much like those in North America) by producing convergence that forced lifting of parcels. Of the two cases that did not have a boundary present, both were disorganized MCSs, associated with surface convergence aligned with the AEW trough.

What is clear from Figure 3.3 and from Table 3.3 is that for CI to occur, factors separate from the AEW are required. In fact, the clear requirement for some form of a lifting mechanism and the need for a peak of the diurnal cycle indicates that rising motion and/or priming of the temperature and moisture fields by the AEW alone are not sufficient to lift parcels to their LFC.

Despite the clear reliance on AEW-independent factors for the initiation of moist convection, it's clear that a region of preferred initiation is the northerlies of the AEW. To understand where the AEW may have supported the initiation of moist convection, we cross-examined the factors likely to have caused each MCS to initiate (those in Table 3.3) with the factors the AEW promoted (i.e. moistening, ascent, or CIN removal). These are shown in bold in Table 3.3. In 12 cases out of 21, factors that had a role to play in the initiation of moist convection were likely supported by AEW variability. In 7 of these cases, moistening was supporting initiation in a phase of the AEW where moistening typically occurs. In four cases ascent was observed supporting initiation where adiabatic ascent is typically observed in the AEW. Further, the magnitude of observed ascent was consistent with the typical magnitude of ω in that phase of the AEW. In one further case, capping-level temperatures were reduced in a phase of the AEW where CIN is being reduced. This highlights the fact that although the AEW is not the primary factor in initiating moist convection in most cases, the AEW is producing noticeable tendencies that likely supported the initiation.

3.6 Mechanisms Supporting the Maintenance of MCSs

As was shown in Section 3.2, MCSs in the northerly phase of our simulated AEWs have a duration that is longer than both the average diurnal cycle and an average duration of observed MCSs over West Africa given by Laing et al. (2008). This highlights the possibility that the environment in the northerlies is more favorable for the maintenance of MCSs. In this section we discuss a mechanism, hinted at by Janiga and Thorncroft (2016), for the improved maintenance of QLCSs in the northerlies. This theory invokes RKW theory

Table 3.3: Factors that influenced the initiation of MCSs. Factors in bold are those supported by the phase of the AEW (e.g. AEW was promoting moistening in area of initiation and moistening also had a role in initiation).

MCS	Positive Factors for MCS initiation	Terrain/Boundary Present
2007-1	Surface warming and **moistening** overcoming CIN	Mandara Mountains
2007-2	Surface warming overcoming CIN	SAL boundary
2007-3	Surface warming overcoming CIN	Cameroon Highlands Outflow from previous MCS
2007-4	Surface warming and **moistening** overcoming CIN	Jos Plateau Outflow from previous MCS
2007-5	Surface warming overcoming CIN CIN removal	Jos Plateau
2007-6	Surface warming overcoming CIN, **ascent**	SAL boundary
2007-7	Ascent	Cameroon Highlands
2007-8	Surface warming overcoming CIN	SAL boundary
2007-9	**Ascent**	Outflow from previous MCS
2007-10	Surface warming and moistening overcoming CIN, **CIN removal** ascent	SAL boundary Lake Chad - temperature gradient
2007-11	Surface warming overcoming CIN	
2007-12	Surface warming and **moistening** overcoming CIN, **ascent**	Guinea Highlands
2007-13	Surface warming and **moistening** overcoming CIN	Guinea Highlands
2007-14	Surface warming overcoming CIN	SAL boundary
2007-15	**CIN Removal**, ascent	
2010-3	Surface warming and **moistening** overcoming CIN	Jos Plateau
2010-4	**Ascent**	SAL boundary, Outflow Senegal River Valley
2010-5	None	SAL boundary
2010-6	None	Outflow from previous MCS
2010-7	**Moistening**	Outflow from previous MCS
2010-8	**Moistening**	Outflow from previous MCS

(Rotunno et al. 1988) by suggesting that, in the northerlies, cold pool circulation is better balanced by the background shear. This balance promotes a more upright updraft that we expect will lead to improved maintenance of QLCSs (Weisman and Rotunno 2004). While RKW theory has been criticized (e.g. Coniglio et al. 2012) it is generally regarded as the leading theory for QLCS intensity and has been tested more rigorously since it's inception (e.g. Bryan et al. 2006; Parker 2010). Here we will examine the background shear present in different AEW phases to see whether RKW theory predicts more intense and likely longer-lived QLCSs in the northerlies.

Figure 3.10 shows hodographs of the 1000–500-hPa winds averaged over the northerlies or southerlies in composite average ERAI and CFSR AEWs. The black lines in Figure 3.10 show the average speed and direction of the QLCSs in our simulations, relative to the AEW surface wind. Here, we assume that QLCS speed corresponds to the cold pool speed which is then used to represent the circulation in the QLCS cold pool. Here we have used only the QLCSs that are clearly cold pool driven. This is verified by a visual examination of surface temperature fields and reflectivity (not shown). We also assume that our population of simulated QLCSs is representative of observed QLCSs. Given that our distribution of simulated MCS speeds accurately compares to those observed in satellite observations by Laing et al. (2008), we believe the latter assumption to be an accurate assumption.

The shear in the northerlies is much larger and in a more southward direction than the shear in the southerlies. While the direction of shear in the southerlies better matches the direction of the QLCS motion, the magnitude of shear in the northerlies better matches the MCS motion. What matters for RKW theory is the magnitude of shear in the direction perpendicular to the cold pool (or in the direction of cold pool motion). The shear that matters is that over the depth of the cold pool. Thus, we project the 1000–7000-hPa shear (a depth typically slightly larger than that of the cold pool) in the direction of MCS motion. This shear is shown in the top-left of each sub figure. This is compared to the QLCS motion and a difference between the two is also given in the top-left. The closer this difference is to 0, the more balanced the cold pool circulation and shear are, and the more upright the updraft will be.

The shear in the direction of QLCS motion is much larger in the northerlies than in the southerlies. This leads to a much smaller difference between QLCS speed and shear in the northerlies than in the southerlies. In the northerlies the difference is 3.8 ms^{-1} using ERAI shear and 2.6 ms^{-1} using CFSR shear. Meanwhile the difference in the southerlies is nearly double that in the northerlies, with 7.4 ms^{-1} using ERAI shear and 4.8 ms^{-1} using CFSR shear. This shows us that no matter which dataset we use to estimate shear, the cold pool

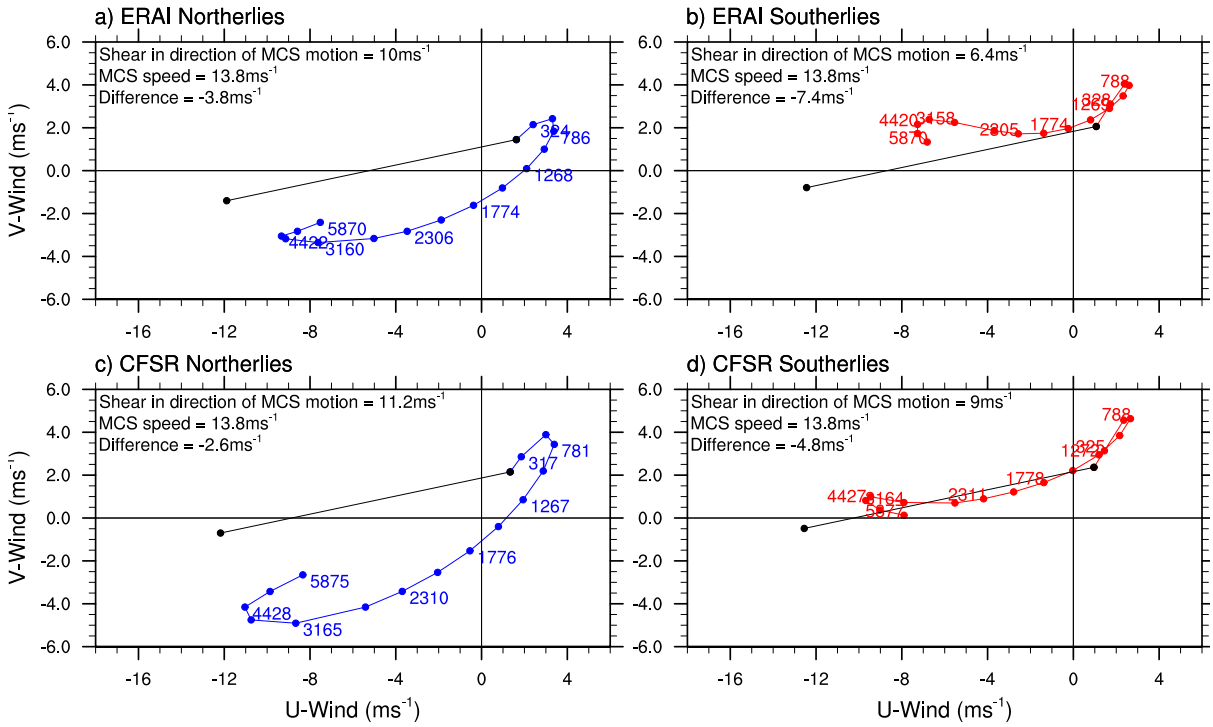

Figure 3.10: Hodographs of the 1000–500-hPa wind shear in composite average a,b) ERAI and c,d) CFSR waves. Average profiles are in the a,c) northerlies and b,d) southerlies. Colored numbers show geopotential height of the point. Black lines show the average speed and direction of the QLCS relative to the surface wind. Text shows shear projected in the direction of MCS motion, QCLS speed, and the difference between the two.

circulation is better matched by the shear in the northerlies. Thus we expect to see more intense and likely longer-lived QLCSs in the northerlies as result of the increased shear.

It should be emphasized here that this analysis utilizes many assumptions and should therefore be considered a first look at how shear affects QLCS maintenance. Thus it should only be considered as evidence for the idea that RKW theory predicts more upright and longer-lived updrafts and thus longer-lived QLCSs in the northerlies. A future study will investigate and quantify the circulation associated with the cold pools to assess whether the assumptions here are correct; specifically we will examine the assumption equating the QLCS speed to the cold pool circulation. Further examples, will compare an MCS in the northerlies with one in the southerlies in the context of RKW theory.

3.7 Role of Negative Convective Factors

While we have highlighted the role that ascent and moistening play in focusing CI in the northerlies, it's equally important to point out the role of descent and drying in the southerlies. As was shown in Figure 3.8, there is very little CI in the southerlies. Given the significant role that the diurnal cycle and orography play in CI (e.g. Figure 3.7), we might expect that CI would still occur regularly in the southerlies. However, as we showed in Figure 3.9 small margins can play a big role in CI over West Africa. In the skew-T diagram 24 hours before CI occurred, there was a vertical profile conducive for moist convection. Despite this, CI did not occur because the low-levels were slightly drier and the surface slightly cooler. Thus the drying and descent in the southerlies likely plays as important of a role in inhibiting CI as the moistening and ascent play in causing CI in the northerlies.

3.8 Summary and Discussion

In this Chapter we have shown that moist convection within the AEW typically takes the form of QLCSs over land and disorganized deep convection over ocean, with a few exceptions. Factors, driven by AEW dynamics, that will vary MCS activity include adiabatic ascent, moisture convergence, CAPE, CIN, and shear over land. Over ocean ascent and moisture seem to be the main drivers of moist convective organization. In nearly all cases examined, CI occurs in conjunction with the diurnal cycle and other factors such as orography and synoptic-scale and mesoscale surface boundaries. This causes CI to be independent of the AEW in time. However, factors such as moisture convergence, adiabatic ascent, and

CIN in the northerlies, along with suppressing factors such as moisture divergence and descent in the southerlies, cause CI to be focused in the northerlies and trough. Once mature, QLCSs are driven by their own dynamics resulting in a nonlinear coupling between the MCSs and AEW over land. However, by invoking RKW theory, we show that there is more favorable shear in the northerlies which likely leads to longer-lived more intense QLCSs there. Meanwhile, enhanced CAPE as a result of both the AEW dynamics, and CIN inhibiting CI in and behind the ridge, allow for a build-up of CAPE that also leads to more vigorous convective updrafts and likely longer-lived MCSs.

While the magnitude of AEW-scale factors supporting moist convection is typically not enough to cause CI alone, we argue that these small variations by the AEW can significantly vary moist convection, since the local afternoon environment over West Africa is already primed for CI. This process is depicted in Figure 3.11. Here, the curves represent a combination of convective factors that at any given time may represent the chance of CI occurring. The dashed line represents a threshold needed for CI to occur. Blue and red lines represent the fluctuation in these factors due to the AEW and diurnal cycles respectively. The black line represents a superposition of the diurnal cycle with the AEW cycle. This superposition then shows how CI may occur or be suppressed by the AEW fluctuations. The sensitivity of CI to small changes in the thermodynamics and moisture is therefore what allows the coupling of CI with the AEW. This process is what leads to no coupling of CI in time (e.g. Figure 3.7) but a clear coupling of CI in space (e.g. Figures 3.8a and 3.8b). While we have not definitively shown this process to be occurring, we have presented supporting evidence in Figure 3.7 and the various tables throughout this section. Future work should thus focus on building the evidence for this theory, preferably with observations.

Finally, these findings lead us to present the theory that the northerlies represent a region for the enhancement of moist convection. By this we mean that many factors come together to enhance moist convection here, not just one. This combines the ideas of Kiladis et al. (2006) and Tomassini et al. (2017) who argued that quasi-geostrophic ascent and moisture convergence respectively are the reason moist convection is focused in the northerlies. In fact, we show that while these are the leading two factors driven by the AEW and supporting CI (e.g. Table 3.3), other factors such as moisture divergence and descent in the southerlies, CIN, CAPE, and shear also vary CI and the intensity and longevity of the resulting MCSs. Thus it is this combination of factors that is important for convective coupling to the AEW.

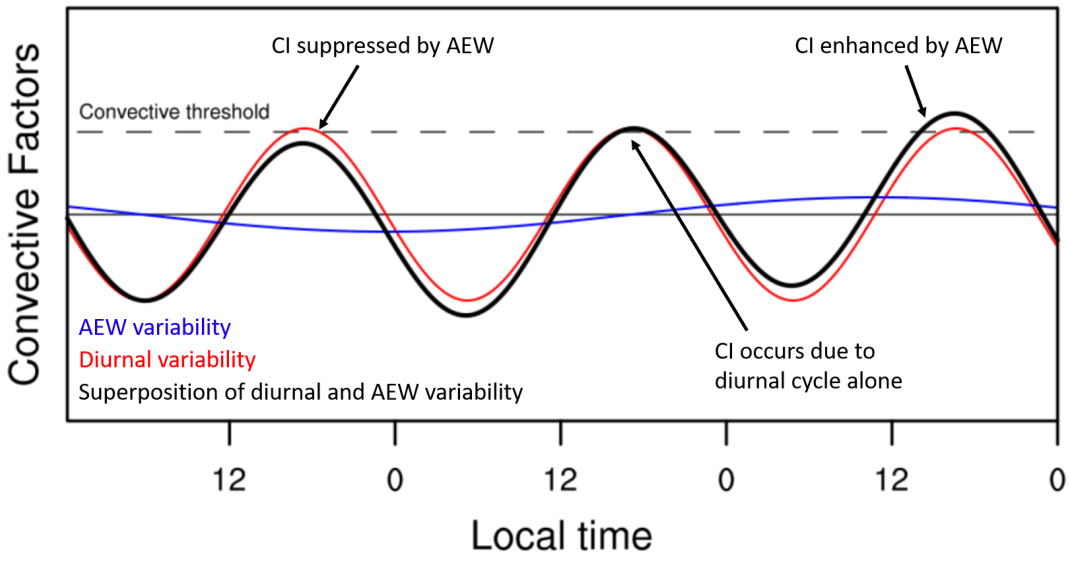

Figure 3.11: Idealized depiction of the super-position of the diurnal cycle with the AEW variability for enhanced and suppressed CI in different phases of the AEW.

CHAPTER

4

POTENTIAL VORTICITY STRUCTURE AND DYNAMICS

In this chapter we use ERAI and CFSR to document and investigate the PV within the AEW. Here, we will examine the structure of PV tendencies relative to the AEW with a particular focus on the diabatic components; research questions 1 and 2 in Section 1.7.2. To achieve this, we first review the time-mean and composite PV structure over the entire region where AEWs are present. This will help in the interpretation of the dynamics in later sections. We then examine the AEW-scale PV budget to gain insight into the dynamics of AEWs and it's interaction with moist convection, all from the perspective of PV. This Chapter will therefore provide a detailed examination of the large scale-features of AEWs, their PV, and their interaction with moist convection.

4.1 Balanced Dynamics in the AEW

4.1.1 Balanced Circulation

A key indicator of the utility of PV is whether a balanced circulation exists. Figure 4.1 shows composite average AEW-scale PV at 650 hPa (the level of peak anomalous winds) in ERAI. Shown in vectors is the composite average AEW-scale rotational wind (Figures 4.1a-c) and divergent winds (Figures 4.1d-f) at each base point. The rotational component of the flow is much stronger than the divergent component. Further, the rotational flow closely matches PV contours. Although not shown, the result for CFSR is qualitatively similar. In both reanalyses we can therefore expect a balanced flow around an AEW-scale PV anomaly.

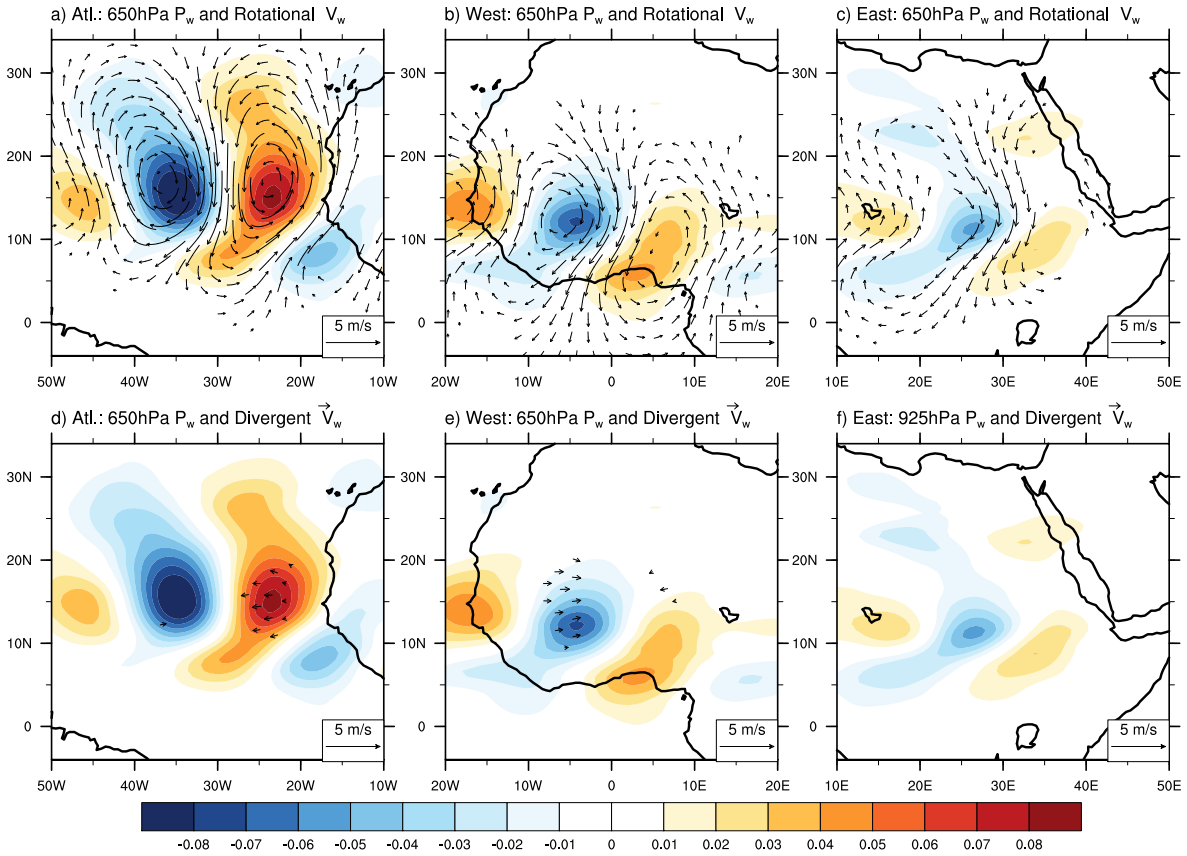

Figure 4.1: Composite average AEWs in ERAI showing the 650-hPa AEW-scale PV (PVU; shaded) with a,b,c) rotational and d,e,f) divergent wind vectors (ms^{-1}). Base points are a,d) Atlantic, b,e) West Africa, and c,f) East Africa.

4.1.2 AEW Stormtrack

Figure 2.4 shows the AEW storm-track as represented by the time-mean eddy kinetic energy (EKE) and the variance of AEW-scale PV. Both EKE and PV clearly show the two AEW storm-tracks on either side of the mean AEJ latitude. At 925 hPa, the low-level northern storm-track stretches from the Red Sea to the Atlantic along about 18°N. This track peaks at the West African coast before rapidly diminishing over the Atlantic. At 650 hPa along a mean latitude of 10°N, the southern track extends from 35°W (downstream of the Ethiopian highlands) to the eastern Atlantic. The track widens and shifts northward near the West African coast such that the two tracks merge over the eastern Atlantic. The similarity between EKE and PV distribution is indicative of a balanced kinematic response to variations of PV in AEWs. Both ERAI and CFSR are broadly consistent in their representation of the AEW storm-tracks.

4.2 Structure of the mean AEW environment

To understand the balanced dynamics of AEWs, we begin by reviewing the structure of the West African environment within the context of an unstable RW. Figure 4.2 shows the meridional PV gradient, time-mean zonal winds, and potential temperature in both ERAI and CFSR.

Over Africa and the eastern Atlantic, the PV gradient in the vicinity of the AEJ reverses sign both along the horizontal at 650 hPa (Figures 4.2a,b) and in the vertical, north of 10°N (Figures 4.2c,d). While we show the mean PV gradient on a constant 650-hPa pressure surface here, the interpretation is similar if we choose an isentropic level close to 650 hPa in Figure 4.2 (panels e,f) as is typically done when using Ertel PV. Together with the positive meridional gradient of surface temperature, the necessary conditions for Charney-Stern instability are met by the time-mean environment. At the jet-level, easterly zonal flow is positively correlated with the negative PV gradient (Figure 4.2c,d). Similarly, at the surface, westerly flow is positively correlated with the positive temperature gradient (Figure 4.2e,f). This satisfies the Fjortoft condition for instability (Fjørtoft 1950).

The instability of the mean environment can be be related to interactions of waves on these PV gradients. The opposing PV gradients promote counter-propagating phase-locked RWs that can mutually reinforce each other (Hoskins et al. 1985). Along the horizontal, the interaction occurs in the mid-troposphere between the waves on the positive PV gradient between 5° and 10°N, and negative PV gradient between 10° and 20°N. Along the vertical, interactions are possible between waves on the mid-tropospheric negative PV gradient

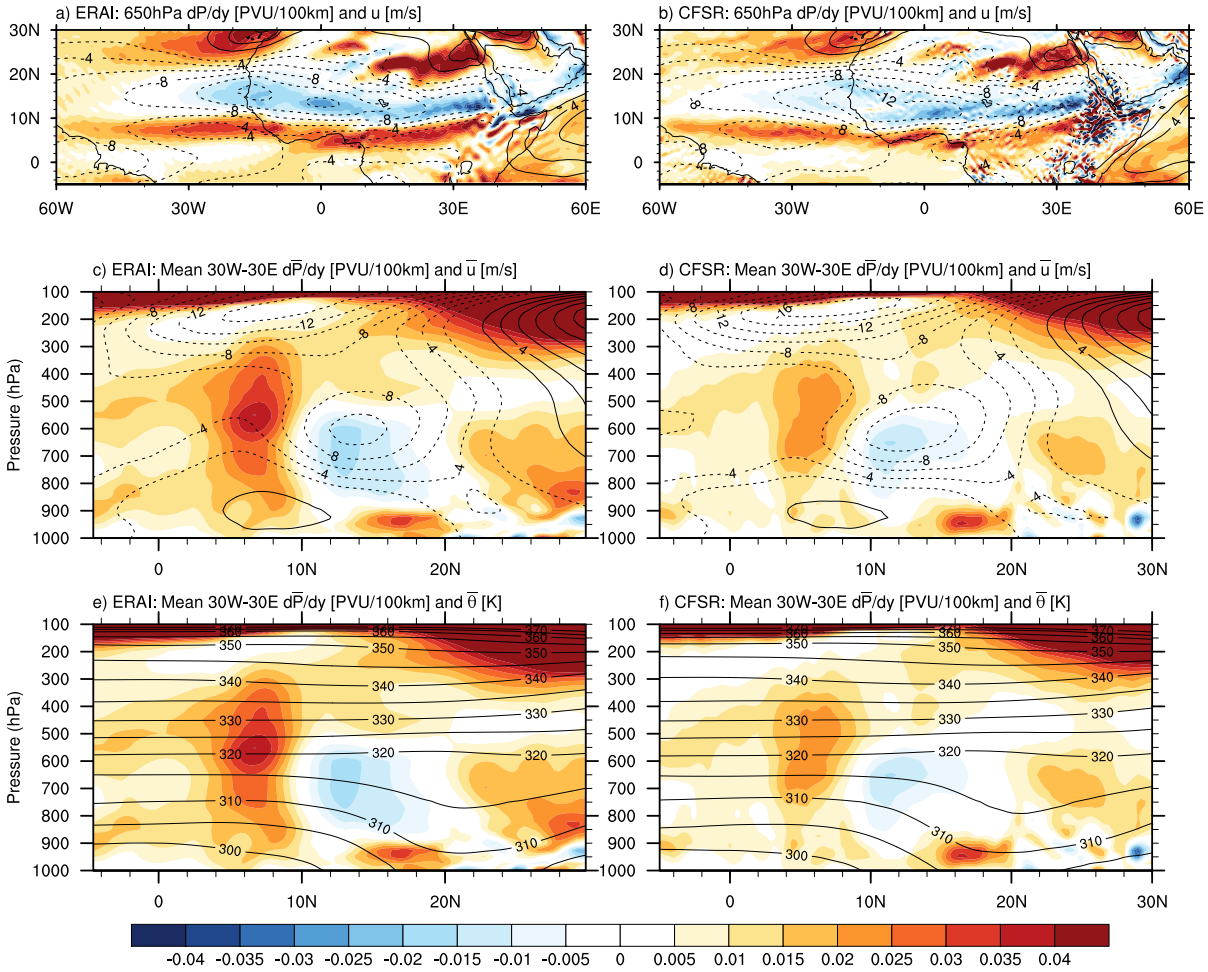

Figure 4.2: Meridional gradient in mean JAS PV (shaded) at a,b) 650 hPa, and c-f) for a 30°W-30°E average. Overlaid in contours is the time-mean JAS a-d) Zonal Wind with dashed contours negative and solid contours positive, and e-f) Potential Temperature. Contour spacing is 2 ms^{-1} and 5 K respectively.

with those on the positive PV gradients above and below, as well as on the positive surface temperature gradient (Thorncroft and Hoskins 1994). These interactions between RWs can promote growth of the overall AEW through combined barotropic-baroclinic instability (Burpee 1972).

The structure of the time-mean PV gradients is similar in the two reanalysis but of larger magnitude in ERAI. The AEJ, however, is stronger in CFSR. This implies that phase-locking of CRWs will be more likely in one reanalysis than the other and therefore we should expect a difference between the magnitude of barotropic-baroclinic instabilities between the two reanalyses.

4.3 The PV structure of AEWs

In this section we review the structure of AEW-scale PV and the attendant circulation within the context of dry instabilities. We also describe the relationship between PV, precipitation, and diabatic heating. While some of these topics have been examined by previous studies (e.g. Burpee 1972; Kiladis et al. 2006; Hsieh and Cook 2008; Janiga and Thorncroft 2016), this section brings all this work together in one place with modern reanalysis data.

4.3.1 AEW-Scale PV and circulation

Figures 4.3 and 4.4 show the composite AEW-scale winds and PV. The top two panels show horizontal sections at 650 hPa and 925 hPa respectively. The bottom two panels show vertical cross-sections averaged between 5°N and 15°N, and 12°N and 22°N latitudes. Mean zonal winds are shown as vectors on the right of each panel. These vectors help visualize the background horizontal and vertical shear profiles.

Horizontal Structure

At both 650 hPa and 925 hPa levels, positive and negative PV anomalies are associated with corresponding cyclonic and anticyclonic circulations (Figs. 4.3a-f and 4.4a-f). This indicates that a quasi-balanced circulation exists in association with the PV anomalies at these two levels, consistent with section 4.1.1. The core of the AEJ can be seen between 12°N and 15°N latitude. The AEW at 650 hPa is tilted upshear in the horizontal plane on both the north and south side of the jet. The PV anomalies peak close to the axis of the jet, within the negative background meridional PV gradient (c.f. figure 4.2). The circulations

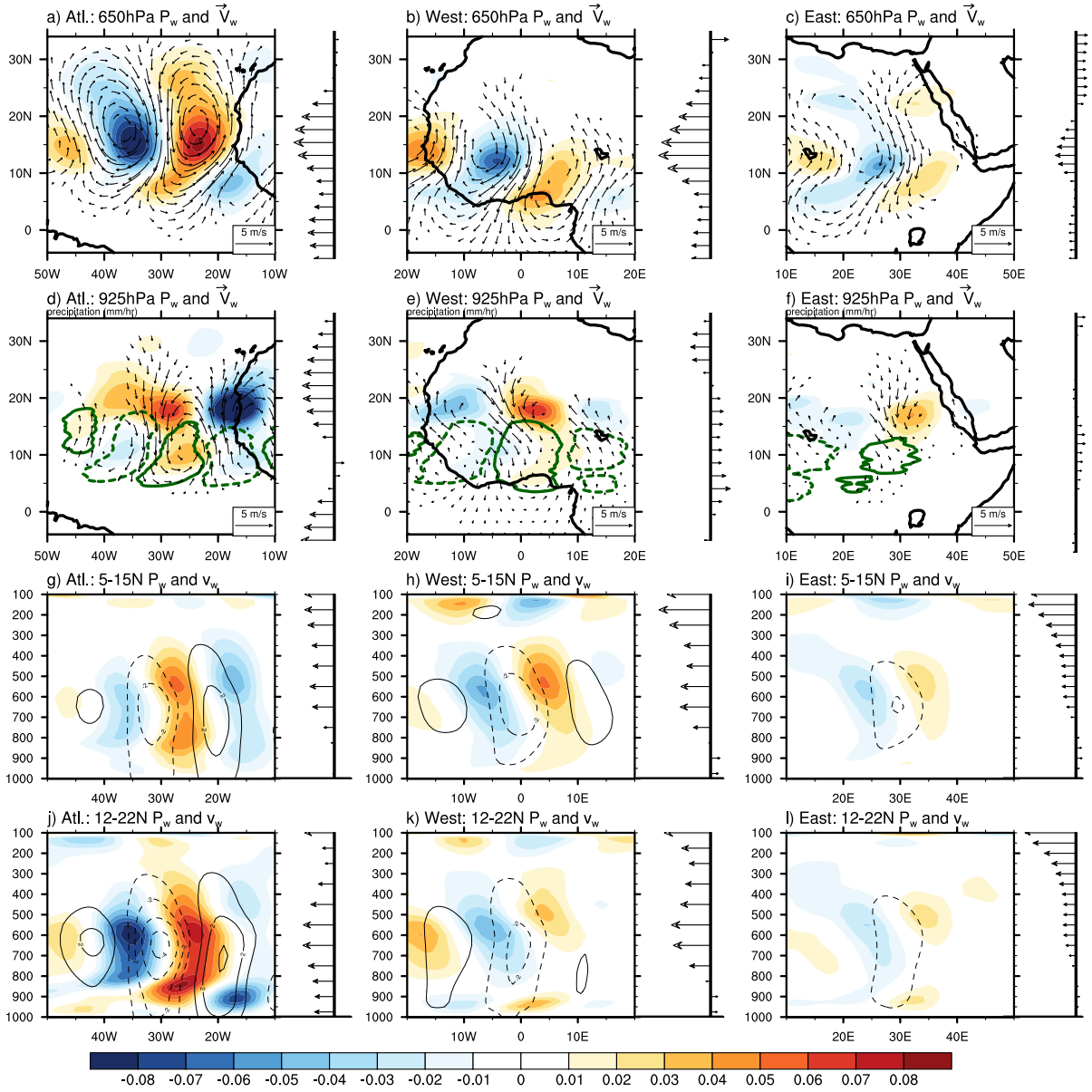

Figure 4.3: Composite-average ERAI a,b,c) latitude-longitude cross-sections of 650 hPa AEW-scale PV and winds, d,e,f) latitude-longitude cross-sections of 925 hPa AEW-scale PV and winds, as well as the 1 $mmhr^{-1}$ contour of AEW-scale TRMM precipitation (green contour), and g,h,i) pressure-longitude cross-sections at the composite latitude of AEW-scale PV and meridional winds (0.5m/s contour interval; negative values dashed; positive values solid). Only significant winds shown. Corresponding time-mean wind profiles are presented along right side of each plot. Units are PVU and ms^{-1}.

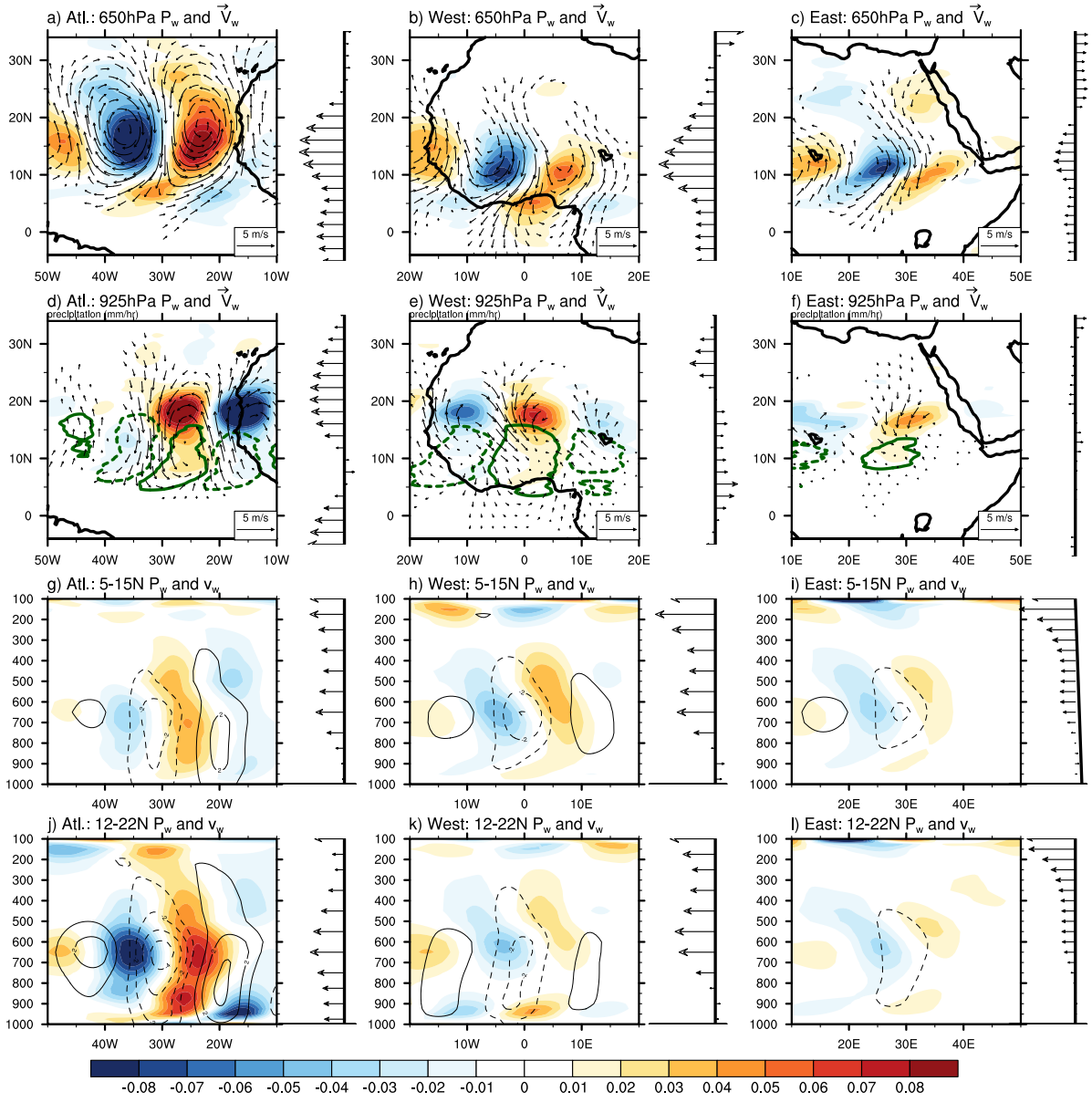

Figure 4.4: As in figure 4.3 but using CFSR.

extend across the jet into the positive meridional gradients on the northern and southern flank of the jet. This constitutes the southern track.

The PV anomalies of the wave at 925 hPa are predominantly located around 20°N and constitute the northern AEW storm-track. At this level, the wave does not have a consistent discernible tilt. Thus, the horizontal PV structure has a configuration consistent with barotropic instability that is only active at the 650 hPa level.

Vertical Structure

The existence of a quasi-balanced circulation associated with the AEW-scale PV can also be seen in the longitude-pressure cross-section of PV and meridional winds (Figures 4.3g-l and 4.4g-l). At nearly all levels, the meridional winds are in quadrature with the PV anomalies for both AEW tracks, indicating a balanced circulation that spans a deep column, again consistent with section 4.1.1.

Figures 4.3g-i and 4.4g-i also show that the composite southern track AEW is initially weak and confined to the mid-troposphere, between 500 and 600 hPa, over East Africa. It amplifies over West Africa and develops a secondary low-level maximum close to 800 hPa over the eastern Atlantic. This will be related to the effect of moist convection in subsequent sections. The cross-section for the northern track shows amplification of PV at the low levels as the waves travel from east to west Africa. Over the Atlantic, the merging of the two tracks and the northward shift of the southern track is evident in the deep PV column with maxima in the mid-troposphere and low-levels as noted above (Thorncroft and Hodges 2001).

Figures 4.3j-l and 4.4j-l show the vertical structure of the AEW averaged between 12°N and 22°N, a region representative of the northern track. Over East Africa, the vertical shear is weak but the upshear tilt in the PV anomalies between 600 hPa and 900 hPa is conducive for baroclinic growth. A similar situation is apparent over West Africa but with stronger shear and a greater upshear tilt. The reanalyses somewhat vary in their representation over the Atlantic, especially in the low-levels. ERAI has a strong tilt in the PV between 700 and 900 hPa but there is little shear in this region. Meanwhile CFSR has a more gradual upshear tilt in the PV anomalies between 600 and 1000 hPa and there is some shear present. The absence of moist-convection and attendant diabatic feedbacks in the northern track AEWs is evident from the lack of precipitation anomalies in this latitude band (Figures 4.3d-f and 4.4d-f). This confirms that baroclinic instability is the main mechanism that could destabilize the northern track AEWs.

Figures 4.3g-i and 4.4g-i show the vertical structure of AEWs between 5°N and 15°N, a region representative of the southern track. Over East Africa (Figs. 4.3i and 4.4i), the vertical shear is mainly easterly with the exception of a slight westerly shear around 600–500 hPa. Overall, the PV anomaly is tilted downshear above 500 hPa and upshear below. While the lower level PV anomaly is within weak easterly shear, it does have a configuration that is favorable for baroclinic conversions. Over West Africa, the PV column is tilted upshear both above and below the jet core. Over the Atlantic, the PV column is relatively upright below the jet while still tilted upshear above.

As noted in Figures 4.2c,d the background meridional PV gradient in this latitude range is positive throughout the troposphere. Simultaneously, the meridional temperature gradient at the surface is also positive (4.2e,f). This precludes dry baroclinic instability in this latitude band. However, previous studies (Berry and Thorncroft 2005, 2012) have proposed that some form of moist baroclinic instability may occur in this region. As emphasized by Cohen and Boos (2016), upshear tilt is a potential marker of moist baroclinic instability in the presence of diabatic sources of PV. We explore this further in subsequent sections.

Figure 4.5 shows cross-sections in latitude through the composite AEW troughs. Over East and West Africa the mid-level PV anomalies associated with the southern track AEWs are between 5°N and 18°N, and 500 and 850 hPa. The northern track AEW-scale PV anomaly is between 15°N and 20°N below 900 hPa. The northern track is clearly associated with the strong Sahara–Sahel surface temperature gradient while in the southern track, isentropes are mostly horizontal. The merger between the two is clear over the Atlantic where a deep PV column forms at 15°N in both reanalyses.

4.3.2 Interaction between the northern and southern stormtracks

While the existence of two distinct tracks of AEWs has been well documented (e.g. Carlson 1969; Kiladis et al. 2006), the dynamical connections between them have not been explored in detail. As noted earlier, based on purely dry-dynamics, the low-level northern track is typically attributed to baroclinic growth while the mid-level southern track to barotropic growth. As such, some studies have treated the two tracks as being independent of each other (Chang 1993; Chen 2006). This raises several questions: Do the waves in the two tracks evolve independently of each other or does one stormtrack seed the other? Figures 4.3d-f and 4.4d-f offer some clues. Recall that all composites are made relative to AEW activity at 650 hPa. These figures show AEW-scale PV anomalies at 925 hPa within the northern track that are associated with AEW activity at 650 hPa in the southern track. From this simple

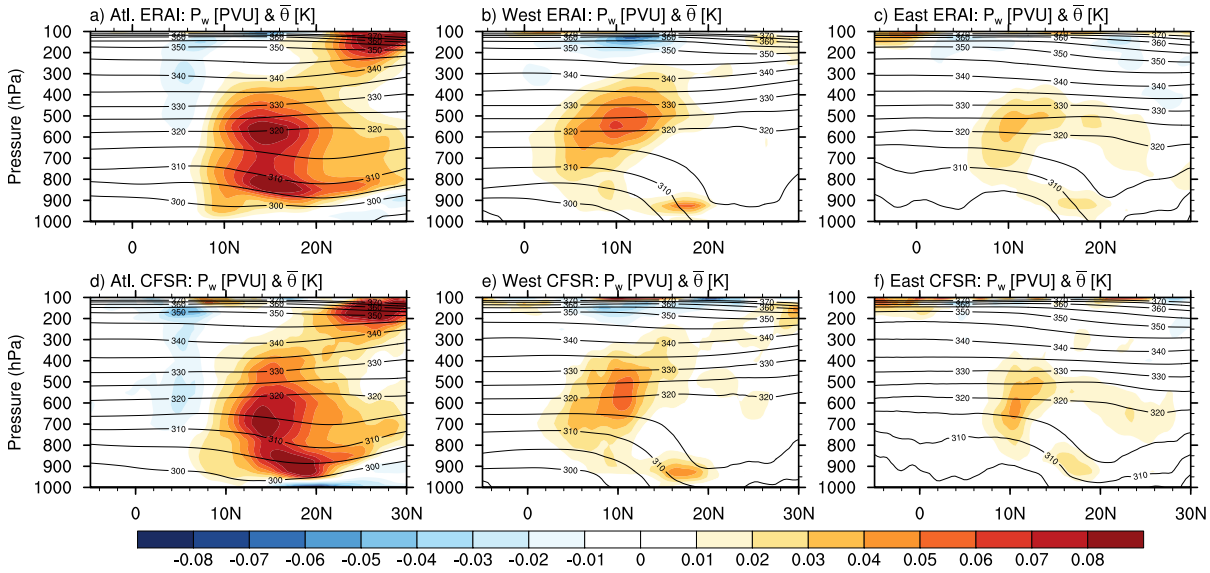

Figure 4.5: Latitude-height cross sections of AEW-scale PV and time-mean potential temperature through the composite average troughs at each base point. Base points a,d) Atlantic, b,e) West Africa, c,f) East Africa. Plots are shown for a,b,c) ERAI and d,e,f) CFSR.

analysis, it is evident that the waves in two tracks are likely dynamically interacting since northern track PV and wind anomalies are present at 925 hPa even when the composite base point is at 650 hPa. Further, the statistically significant circulations associated with the PV anomalies span a wide latitude range and can work to mutually reinforce PV or moisture anomalies. Additional work is needed to fully understand the implication of the interaction and to establish whether it has a destabilizing effect.

From here out, since our goal is to understand the relationship between AEWs and moist convection, and moist convection is mostly active south of 15°N (e.g. the green contour Figures 4.3d-f and 4.4d-f) all further analysis is focused on the southern track of AEWs.

4.3.3 AEW-Scale Diabatic Heating

The structure of diabatic heating is fundamental for the PV budget because it's gradient defines the magnitude and location of the non-conservative diabatic source term. Here we examine the structure of AEW-scale diabatic heating and compare the various means of representing it. Figure 4.6 shows longitude-pressure cross-sections of PV and diabatic heating associated with a composite AEW. Each row of plots represents diabatic heating via a different variable (ERAI Q_1, CFSR Q_1, CFSR H, or CFSR H_L).

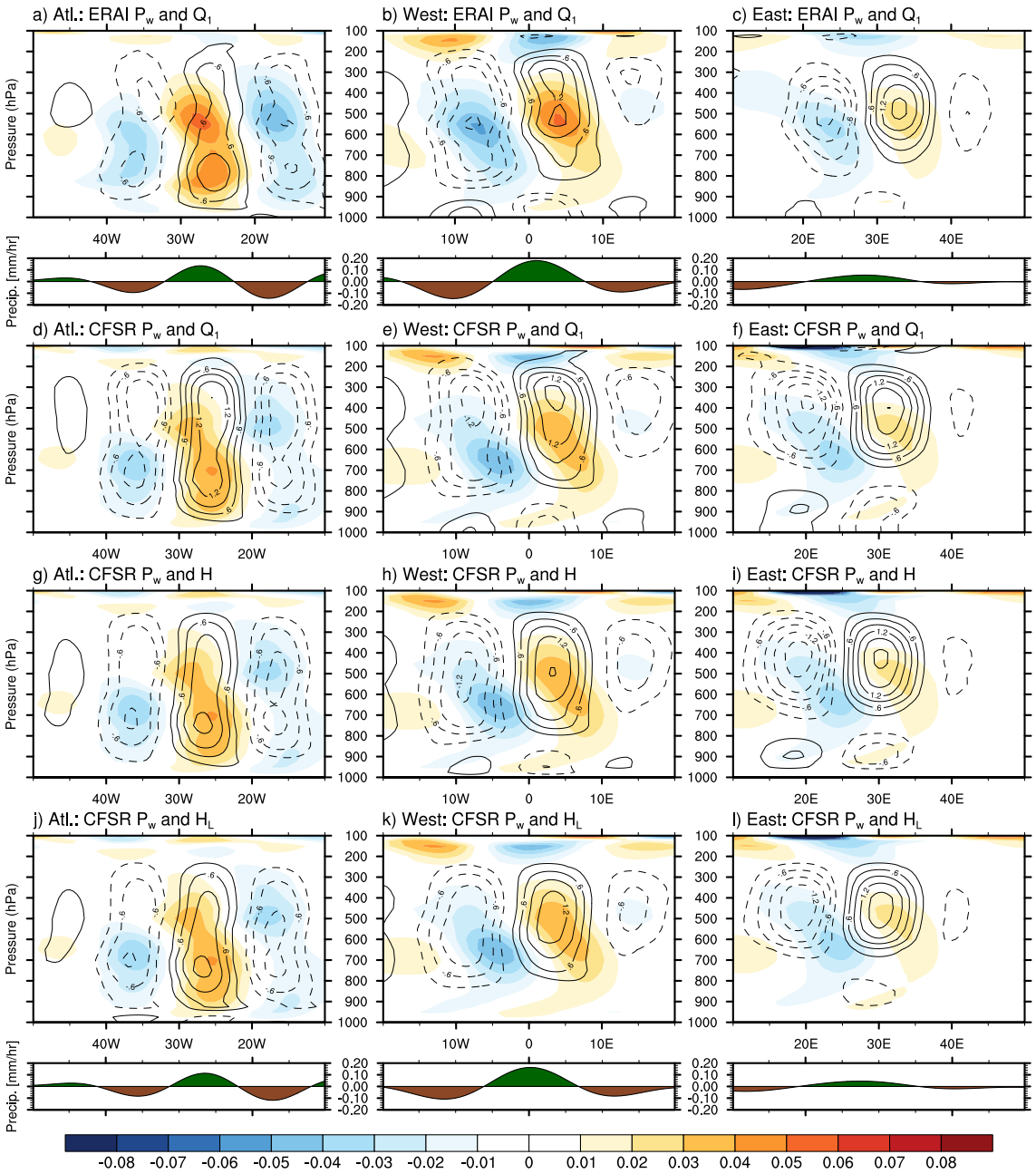

Figure 4.6: Longitude-height cross-sections of AEW-scale PV (shades, PVU) and AEW-scale diabatic heating (contours, K/day). Representations of diabatic heating are a-f) Q_1, g-i) H, and j-l) H_L. a-c) are for ERAI and d-i) are for CFSR. Composite AEWs are at the a,d,g) Atlantic, b,e,h) West Africa, and c,f,i) East Africa base points. Each cross-section is averaged between 5-15N. The green-brown line plots represent TRMM precipitation for the composite ERAI AEWs (top row) and the composite CFSR AEWs (bottom row).

At the East Africa base point, the structure of all of these are similar. The heating anomalies exhibit a dipole structure in the vertical with one peak at 450 hPa and a weaker, opposite-signed second peak at 900 hPa. This vertical structure of diabatic heating is typically representative of stratiform precipitation in the tropics (Schumacher et al. 2007). Diabatic heating at upper-levels and cooling at lower-levels occurs just to the west of the trough (positive PV anomaly). The opposite pattern occurs just to the west of the ridge (negative PV anomaly). The magnitude of the peak heating in the upper-levels is about 2.5–3.5 Kday^{-1}. The magnitude of the peak cooling at the lower-levels ranges between 0.5 and 1.5 Kday^{-1}.

TRMM precipitation rates are also shown in Figure 4.6. Composite precipitation using AEW events identified from ERAI is shown under the ERAI figures, and the same using the CFSR AEW events is shown under the CFSR figures. Precipitation typically peaks to the west of the heating over cooling anomalies. This suggests that the peak convective rainfall leads the strongest heating anomalies. This, coupled with the structure of diabatic heating anomalies points to stratiform precipitation dominating these heating rates at the East Africa base point.

At the West Africa base point, the heating anomalies are more top heavy with peak heating rates of 1.5-3 K day^{-1} centered at around 400 hPa, and the overall heating anomalies stretching downward to 750 hPa. Low-level cooling rates in ERAI have a similar structure but are slightly stronger than at the East Africa base point. In CFSR the cooling rates are somewhat similar for Q_1 and H although they are based slightly lower. Meanwhile for CFSR H_L there are no low-level cooling rates indicating that these are likely not driven by condensational processes linked to stratiform cloud. This leaves radiative and boundary layer processes as the cause of the low-level cooling anomaly. A cursory examination of these indicate that it is in fact the boundary layer processes driving this cooling (not shown). Exactly why the boundary layer drives this cooling in and ahead of the trough is still unclear.

At the Atlantic base point, the structure of heating is quite different. The heating anomalies are deep, single-signed and bottom-heavy. This suggests that AEW-scale heating is dominated by deep moist convection at the Atlantic base point. Heating and corresponding precipitation anomalies are nearly in phase with the PV anomalies, with increased precipitation in the trough and decreased precipitation in the ridge. As noted earlier, a secondary PV maximum is now in place around 800 hPa.

These results suggest that there is a transition from dominant stratiform cloud to deep convection as the AEW moves westward. This transition is most prominent around the West African coast as noted by other studies (e.g. Janiga and Thorncroft 2016). However, a deepening of the positive heating anomaly with a weak or non existent low-level cooling

anomaly – especially when measured with H_L – indicates that this transition begins well before the AEW reaches the coast.

Figure 4.6 shows that all three estimates of heating in CFSR (Q_1,H,H_L) produce similar spatial structures. This suggests that Q_1 is a reasonable estimate of the explicit diabatic heating (H) in AEWs. While the latter is preferred, it is not available for ERAI. For this reason, the following PV budgets will use H when calculating PV source terms using CFSR but Q_1 when using ERAI.

4.4 PV Sources in Composite AEWs

We now examine sources and sinks of AEW-scale PV from equation 2.31 in order to understand their structure relative to the AEW. Figure 4.7 shows the PV tendency (shaded) and the advection by the mean horizontal wind ($-\bar{V}\cdot\nabla P_w$, contours). In all three regions, horizontal advection by the mean flow dominates the PV tendency above 700 hPa but is very weak below. The PV tendency below 700 hPa is weak over East Africa and progressively amplifies westward. The PV tendency below 700 hPa also has a clear upshear tilt over West Africa and then becomes nearly upright over the Atlantic. This is consistent with the composite PV in Figure 4.6.

The non-advective sources of PV are shown in (Figures 4.8 and 4.9). The top panel in these two figures shows the PV anomaly (shaded) and the quasi-Lagrangian tendency (contours), which is defined as the difference between the local PV tendency and the advection by the mean flow (i.e. the difference between the two tendencies shown in Figure 4.7). In other words, it is the sum of source terms excluding the mean horizontal advection. As expected from 4.7 this is large below 700 hPa. A second region of large values can also be seen above 200 hPa. To understand the source of these non-advective PV tendencies, we now focus on the diabatic sources of PV.

The first diabatic source of note is that associated with AEW-scale diabatic heating ($-\bar{\eta}\partial Q_w/\partial p$). This is the imprint of wave-coupled moist convection on the background mean vorticity. As described in chapter 2.6.2 this term can be interpreted as arising due to an effective background PV gradient. Over East Africa (Figures 4.8f and 4.9f) this source has a dipole structure in the vertical consistent with the vertical gradients in AEW-scale diabatic heating shown in Figure 4.6. A positive PV source is present between 900 and 550hPa at, and ahead of the trough, and is maximized at 650hPa. Above this, there is a PV sink directly above the AEW-scale PV anomaly. In and ahead of the ridge the opposite pattern occurs,

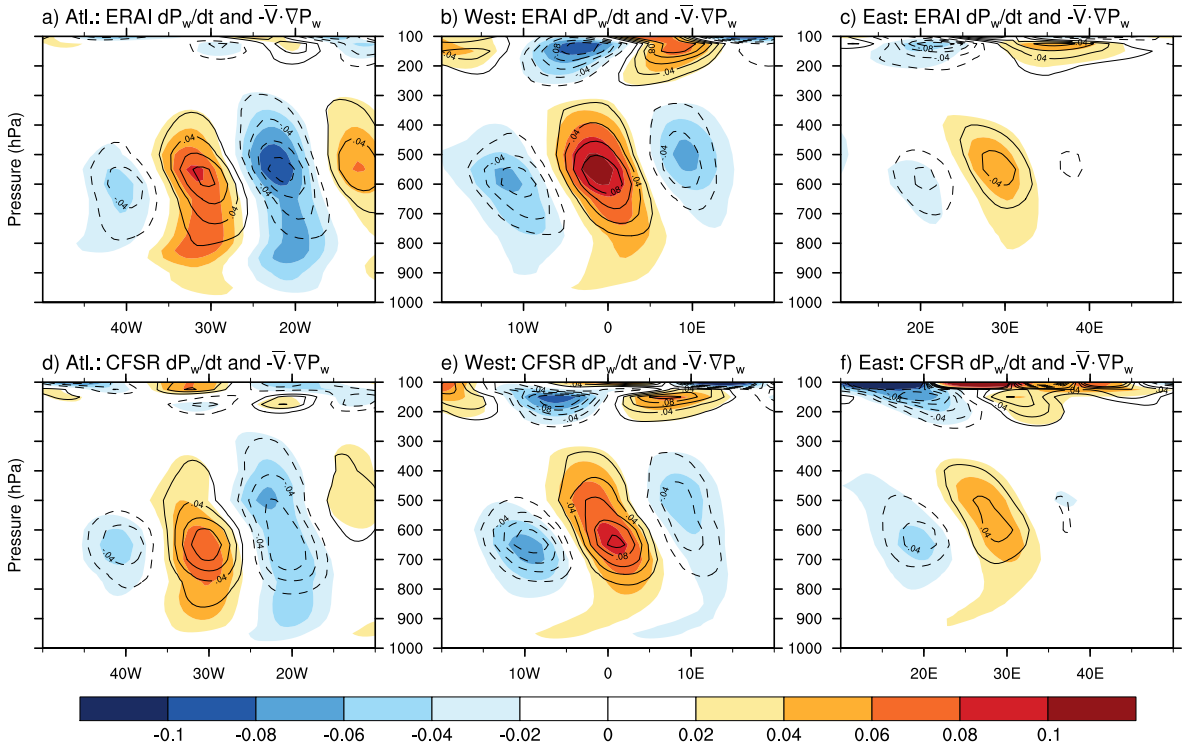

Figure 4.7: Longitude-height cross-sections through composite AEWs averaged between 5-15°N showing AEW-scale PV tendency (PVU/day; shades) and $\bar{V}\cdot\nabla P_w$ (PVU/day contours).

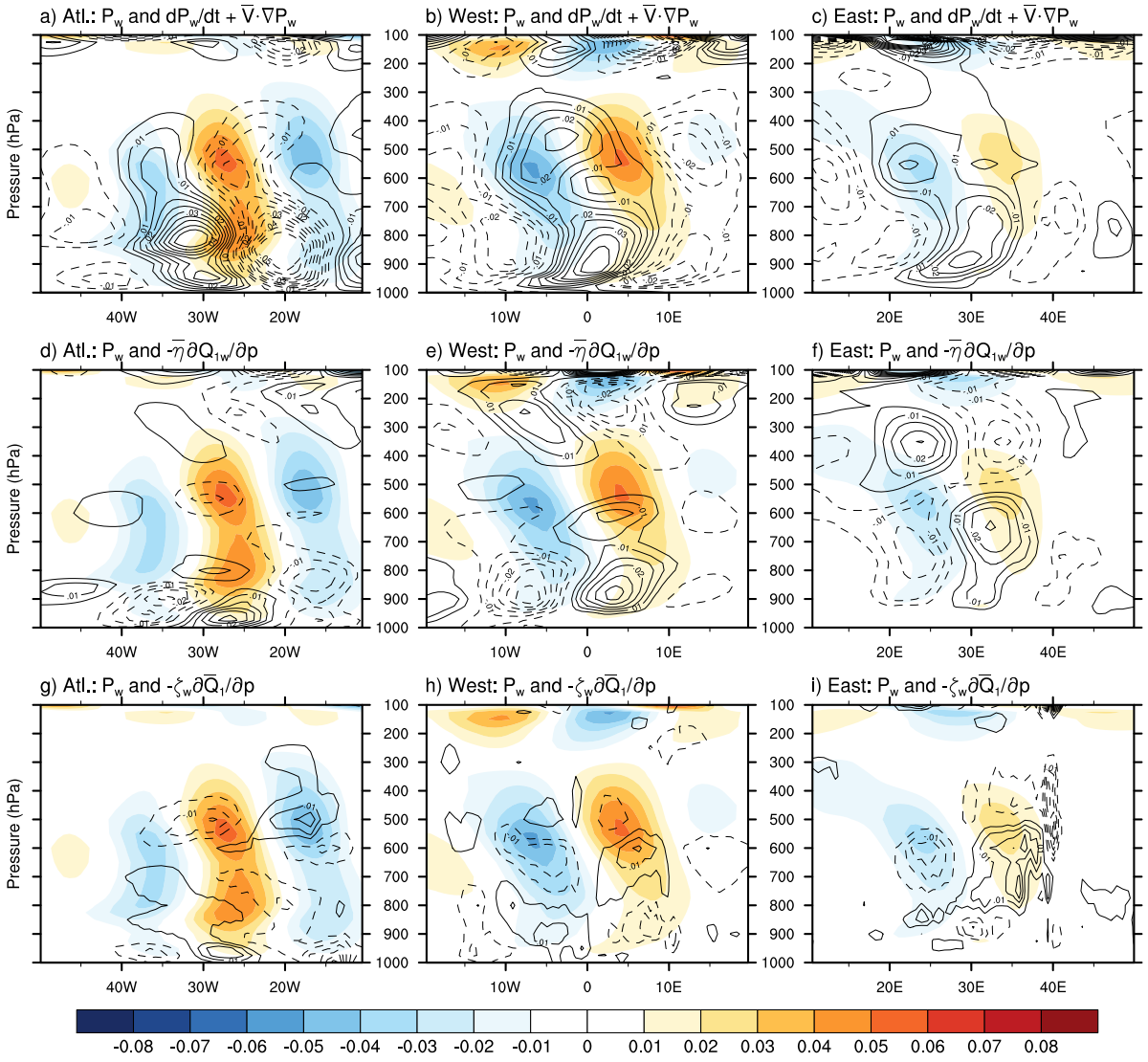

Figure 4.8: Longitude-height cross-sections through composite AEWs showing AEW-scale PV (shades, PVU) and selected source terms (contours, PVU/day). All variables are averaged between 5-15°N. Source terms are a,b,c) $\partial P_w/\partial t + \bar{V}\cdot\nabla P_w$, d,e,f) $\bar{\eta}\partial Q_{1w}/\partial p$, g,h,i) $\zeta_w \partial \bar{Q}_1/\partial p$. All contour intervals are 0.005PVU/day.

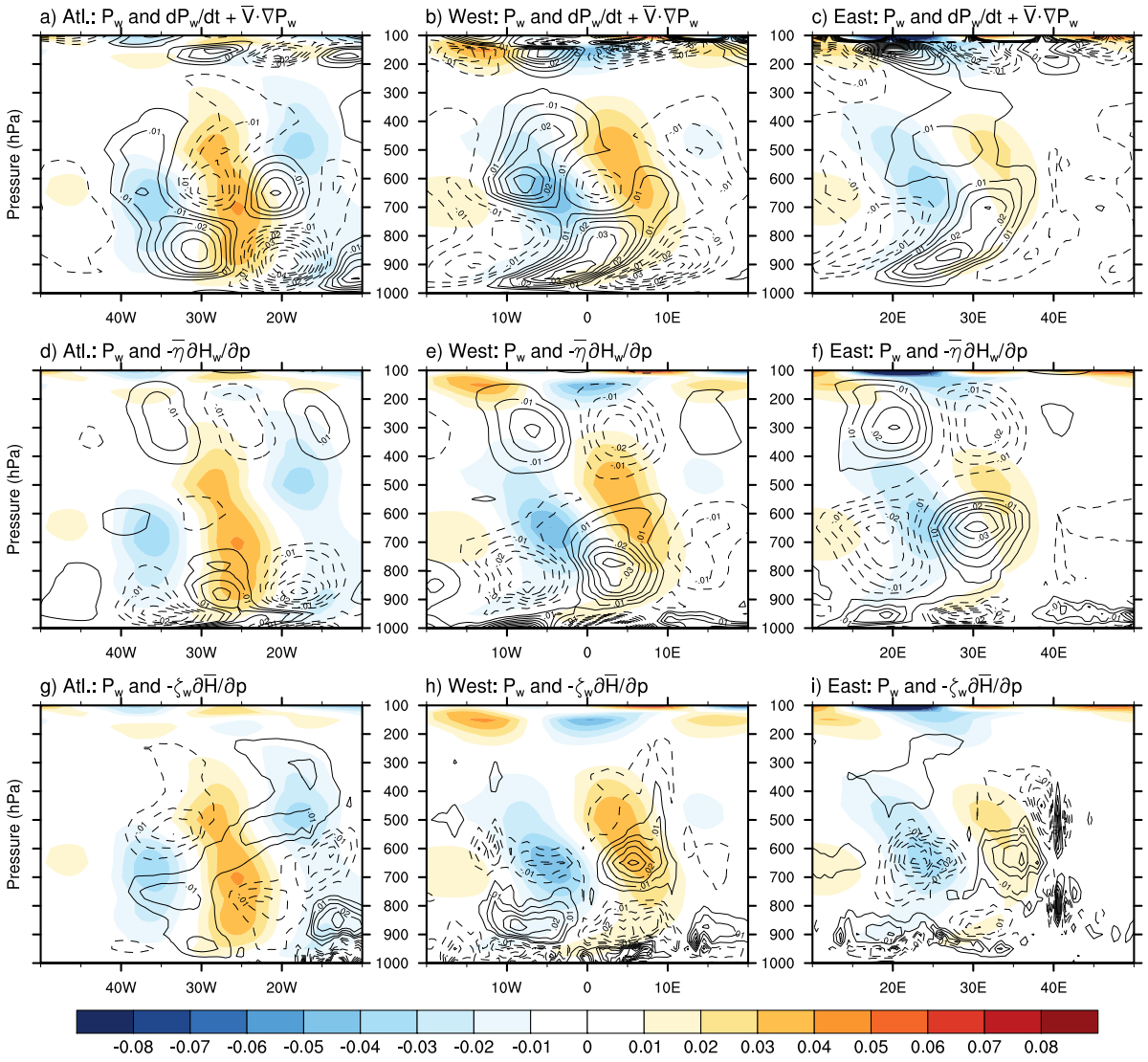

Figure 4.9: As in Figure 4.8 but for CFSR. Also the diabatic heating rates are H instead of Q_1.

with an AEW-scale PV sink in low-levels and a PV source in upper-levels.

As the AEW propagates into West Africa, there is a vertical shift in the production of the low-to-mid-level diabatic PV sources (Figures 4.8e and 4.9e). In ERAI there are two maxima in this source term; one at 600hPa and the other at approximately 850hPa. In CFSR there is only one distinct maxima at around 800hPa. In both datasets, the mid-to-low-level positive source is located at, and to the west of the AEW-scale PV anomaly. This indicates that, over land, it contributes to both growth and propagation of the AEW. This downward vertical shift in PV sources continues out over the ocean. In Figures 4.8d and 4.9d, the largest PV sources are all below 800hPa and in phase with the trough.

The AEW PV transitions from being predominantly a mid-level anomaly over East Africa to a deep column stretching to the low-levels over the Atlantic. This indicates that these diabatic sources associated with coupled moist convection play a role in the development of a low-level PV anomaly. This is of importance to tropical cyclogenesis from AEWs (Russell et al. 2017).

The other diabatic source of note is that associated with background heating but coupled to the AEW by the AEW-scale vorticity ($-\zeta_w \partial \bar{Q}/\partial p$). This represents the imprint of the AEW kinematics on the background heating in the region; mainly forced by the ITCZ. Over East Africa, this source is at it's largest magnitude (Figures 4.8i and 4.9i). Although not as large as the diabatic source associated with AEW-scale heating, it is for the most part, directly in phase with the AEW-scale PV anomaly, indicating it contributes mostly to growth of the AEW. Over West Africa, the two reanalyses diverge on the magnitude of this source. ERAI has only a weak mid-level source, while CFSR diagnoses a much stronger mid-level source of PV. Over the Atlantic both reanalyses indicate a significant low-level source of PV in phase with the AEW-scale PV anomaly. However this source is tilted relative to the AEW-scale PV anomaly such that at 750 hPa it is out of phase with the AEW-scale PV anomaly. These results suggest the importance of background diabatic heating to the growth of the AEW in mid-levels, especially over East Africa.

The final PV source of interest in this section is the advection of background PV by the AEW-scale winds ($-\vec{V}_w \cdot \nabla \bar{P}$). This term essentially represents RW dynamics. This source propagates a wave westward (eastward) when a wave is in a region of positive (negative) meridional PV gradient (Figure 4.2). From the perspective of RW growth, this source represents the combined effect of barotropic and baroclinic instabilities which occur when there is a reversal in the background PV gradient. As an example, if we think about baroclinic instability from the perspective of the 2-level Eady model (Eady 1949), growth of PV at the upper level occurs because the lower-level PV anomaly induces circulation at the

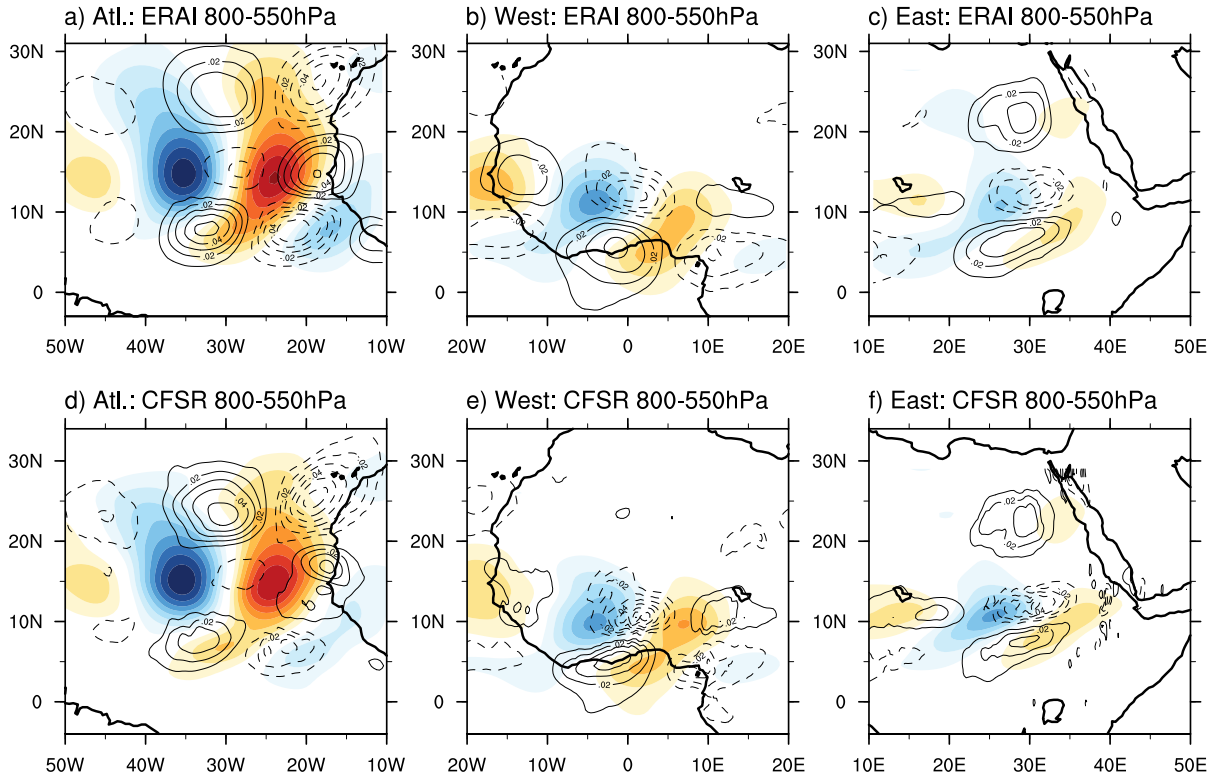

Figure 4.10: Horizontal cross-sections through composite AEWs showing 800-550hPa averaged AEW-scale PV (shades, PVU) and $-V_w \cdot \nabla \bar{P}$. a) and d) are for the Atlantic base point, b) and e) are for the West base point, and c) and f) are for the East base point. a,b,c) show ERAI and d,e,f) show CFSR.

upper-level. The induced circulation advects PV from the background PV 'reservoir' into the current PV anomaly at the upper-level, and therefore it enhances the upper-level PV anomaly. Barotropic instability can be thought of as the same process but in the horizontal.

Figure 4.10 shows horizontal plots of this source term averaged over 800–550 hPa; the layer where there is a reversal in the background PV gradient (c.f. Figure 4.2). At all locations and in both reanalyses there is a checkerboard pattern of PV sources. Over East Africa and the Atlantic there are three 'rows' of these since the background PV gradient is positive equatorward of 12°N, negative between 12°N and 20°N, and positive north of 20°N (Figure 4.2). Over West Africa there are only two 'rows' since the northernmost positive background PV gradient is weak over the Sahara (Figure 4.2). These PV tendencies indicate the presence of counter-propagating waves in the horizontal that give rise to barotropic instability.

4.5 Contributions of PV Sources to Propagation and Growth

The main intent in this section will be to identify the dominant sources of PV in the dynamics of AEWs, from those in Equation 2.31. Following Andersen and Kuang (2012) and Arnold et al. (2013), we diagnose the contribution of the source terms in the PV budget to AEW growth and propagation. For any individual source term Y, in equation 2.31, its contribution to growth must be in phase (positively correlated) with the AEW-scale PV anomaly and can be represented by:

$$Y_g = \langle Y \cdot P_w \rangle / \langle P_w \cdot P_w \rangle \tag{4.1}$$

where $\langle\rangle$ represents an average in longitude. Similarly, it's contribution to the propagation must be in phase with the AEW-scale PV tendency and can be represented as:

$$Y_p = \left\langle Y \cdot \frac{\partial P_w}{\partial t} \right\rangle \Big/ \left\langle \frac{\partial P_w}{\partial t} \cdot \frac{\partial P_w}{\partial t} \right\rangle . \tag{4.2}$$

For the intent here, we chose longitudes of 5–15°N as this encompasses the stormtrack of AEWs shown in Figure 2.4. Table 4.1 shows the contribution of each term in Equation 2.31 averaged over 400–700 hPa, 30°W–40°E, and in time. Additionally, specific terms are averaged in time and examined further in the cross-sections shown in Figures 4.11 and 4.12.

4.5.1 Propagation

From Table 4.1, horizontal advection is the primary driver of AEW propagation in a volume average sense. Of the terms that comprise this advection (c.f. Equation 2.31), the dominant source is $-\bar{V}\cdot\nabla P_w$ which represents advection of the AEW-scale PV by the time-mean basic state. The next largest contribution arises from the advection of the time-mean PV by the AEW-scale circulation ($-V_w\cdot\nabla\bar{P}$). This is the generalized β-effect that is the hallmark of Rossby waves. Some other advective processes are non-neglible in the volume averaged sense, but are small or simply add to one of the two main advective contributions when considering their spatial distribution. With the exception of $-\bar{\eta}\partial Q_w/\partial p$, most diabatic terms are negligible. Based on the results presented in Table 4.1, we now focus on the spatial structure of individual sources highlighted as important to propagation of the AEW-scale PV anomalies.

Figures 4.11a and 4.11b show the contribution from the advection of the AEW-scale PV anomalies by the horizontal time-mean flow ($-\bar{V}\cdot\nabla P_w$). Here positive shading indicates westward motion. As expected, this term is dominant above 700 hPa. As a result, it almost entirely accounts for the westward phase speed of AEWs. Averaging the zonal wind over this region gives a mean wind speed of 7 ms^{-1} in ERAI and 8 ms^{-1} in CFSR. Laing et al. (2008) reported that the phase speed of AEWs ranged between 5-11 ms^{-1} and the median value was about 7 ms^{-1}. Thus, this is consistent with past literature.

Near the surface, however, as a result of the westerly monsoonal flow, this term contributes to a weak eastward motion. Thus the advection of AEW-scale PV by the mean winds can be expected to shear the AEW-scale PV column. To maintain a deep PV column as seen in Figures 4.3g-i and 4.4g-i, there must be some other process contributing positively to low-level AEW-scale PV tendency.

On inspection of the various source terms, the largest contributor to AEW propagation at low-levels (below 750 hPa) is the AEW-scale diabatic heating ($-\bar{\eta}\partial Q_w/\partial p$). This is shown in Figures 4.11c and 4.11d. In both ERAI and CFSR, this diabatic term contributes to westward propagation along most of the AEW track east of 30°W. Therefore it seems that while the mean flow would act to tilt the PV anomaly down-shear, diabatic processes coupled to the AEW likely lead to the upshear tilt seen below 700 hPa (Figures 4.3 g–l, 4.4 g–l).

Further, this indicates that enhanced convection ahead of the AEW trough will reduce the low-to-mid level tilt of the AEW. This has implications for TCs since a more upright PV column with significant convection will more likely present the opportunity for TC genesis. In addition, although smaller, there are also contributions to propagation from this source

Table 4.1: Source terms from equation 2.31 contributing to propagation and growth of AEW-scale PV (calculated using equation 4.2) averaged in the volume encompassed by 400–700 hPa, 4–20°N, and 30°W-40°E. Anything with a fractional contribution of 0.01 (i.e. 1%) or less was deemed to be negligible and for presentation is represented by a -.

Source	Contribution to Propagation		Contribution to Growth (day^{-1})	
	ERAI	CFSR	ERAI	CFSR
$-\bar{V}\cdot\nabla P_w$	0.71	0.79	-	-
$-V_w\cdot\nabla\bar{P}$	0.12	0.06	0.09	0.06
$-V_w\cdot\nabla P_w$	-	-	-	-
$-V_w\cdot\nabla P_r$	0.04	0.03	-	-
$-V_r\cdot\nabla P_w$	0.03	0.03	-	-0.02
$-\bar{\omega}\partial P_w/\partial p$	-0.02	-0.02	-0.02	-
$-\omega_w\partial\bar{P}/\partial p$	-0.02	-0.02	-0.02	-
$-\omega_w\partial P_w/\partial p$	-	-	-	-
$-\omega_w\partial P_r/\partial p$	-	-	-	-
$-\omega_r\partial P_w/\partial p$	-	-	-	0.02
$-\bar{S}\cdot\nabla Q_w$	0.02	-	0.03	-
$-S_w\cdot\nabla\bar{Q}$	-	-	-	-
$-S_w\cdot\nabla Q_w$	-	-	-	-
$-S_w\cdot\nabla Q_r$	-	-	-	-
$-S_r\cdot\nabla Q_w$	-	-	-	-
$-\bar{\eta}\partial Q_w/\partial p$	0.03	0.04	0.06	0.05
$-\zeta_w\partial\bar{Q}/\partial p$	-	-	0.03	0.04
$-\zeta_w\partial Q_w/\partial p$	-	-	-	-
$-\zeta_w\partial Q_r/\partial p$	-	-	0.02	0.03
$-\zeta_r\partial Q_w/\partial p$	-	-	-	0.02

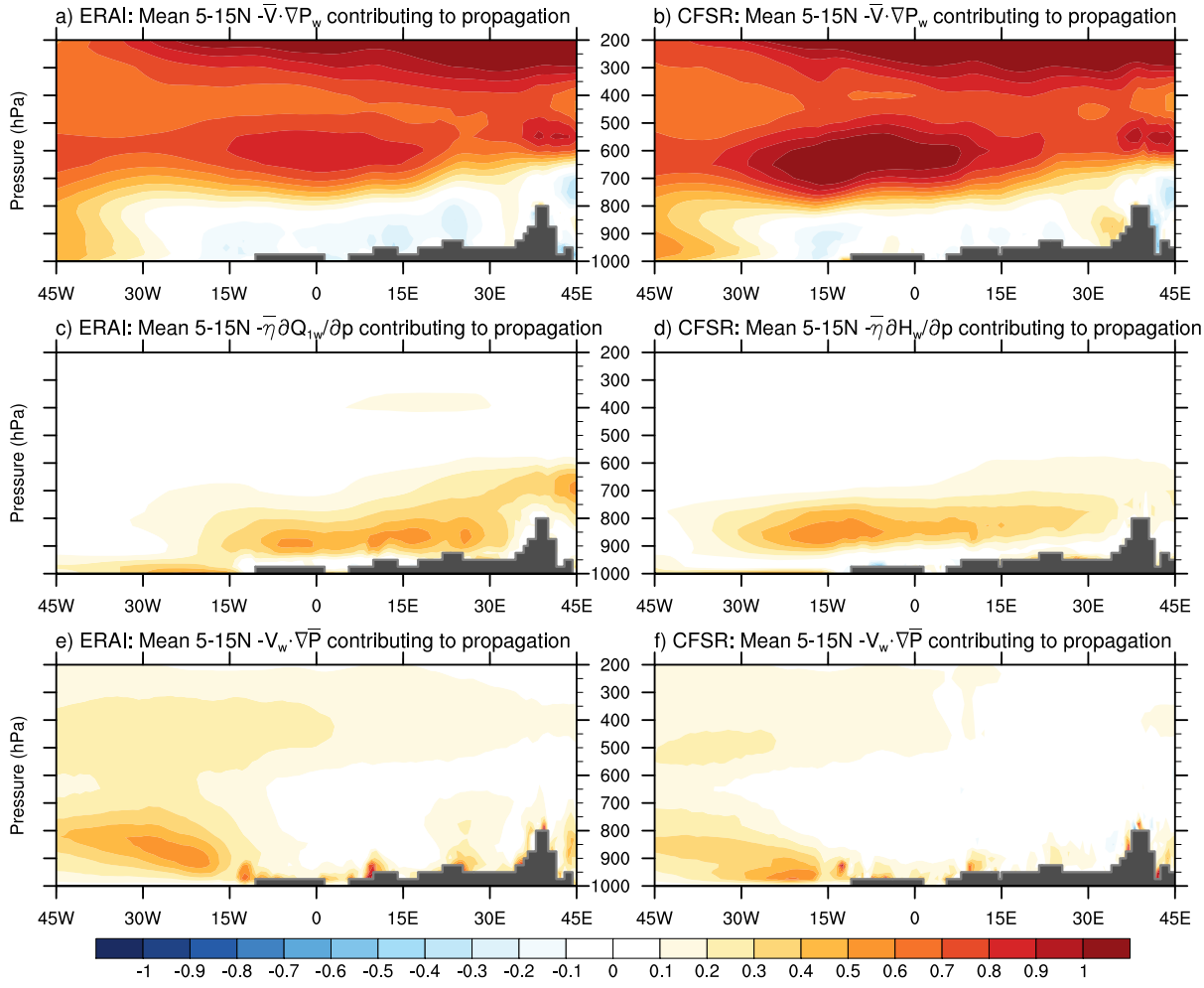

Figure 4.11: Longitude-pressure cross-sections showing the fractional contribution of various source terms from equation 2.31 averaged between 4–20°N for a,c,e,g) ERAI and b,d,f,h) CFSR. Source terms represented are a,b) $-\bar{V}\cdot\nabla P_w$, c) $-\bar{\eta}\partial Q_{1w}/\partial p$, d) $-\bar{\eta}\partial H_w/\partial p$, and e,f) $-V_w\cdot\nabla\bar{P}$. Grey areas show regions below ground.

between 800-600hPa, primarily east of the Greenwhich Meridian. This indicates that it also contributes some to propagation of the mid-level PV anomaly over East Africa.

As seen in Figures 4.6a, 4.6g, 4.8d, and 4.9d enhanced convection transitions into the trough over the Atlantic and therefore there is little contribution from diabatic processes once the AEW moves over ocean. This is corroborated by Figures 4.11c and 4.11d. At this point, the low-level background PV gradient gets stronger and RW propagation processes are more active. This is evident in Figures 4.11e and 4.11f where advection of mean PV by AEW-scale flow ($-V_w \cdot \nabla \bar{P}$) contributes a much larger proportion of the PV tendency west of 15°W, especially in the low-levels. Over land, the RW mechanism contributes little to mid-level AEW-scale PV tendency. This is primarily due to the reversal in the meridional background PV gradients here. Counter-propagating RWs, as shown in Figure 4.10, move in opposite directions and thus contribute little to the motion of the AEW in one way or the other. However, the RW mechanism does contribute to propagation of the AEW above 500hPa over land. These levels coincide with an area where there is no reversal in the background PV gradient and thus contribute to forward motion at these levels.

4.5.2 Growth

Table 4.1 shows that, in the volume average sense, growth is contributed by three main sources. The largest source is the advection of background PV by the AEW-scale winds ($-V_w \cdot \nabla \bar{P}$). The next two contributions are from the AEW-scale diabatic heating ($-\bar{\eta} \partial Q_w / \partial p$) and background heating ($-\zeta_w \partial (\bar{Q} + Q_r) / \partial p$). Other sources have negligible contributions in one or both reanalyses. Based on these results, we now focus on the spatial structure and interpretation of these three sources.

Figures 4.12a and 4.12b show longitude-height cross-sections of the contributions to growth by AEW-scale advection of the time-mean PV ($-V_w \cdot \nabla \bar{P}$) over Africa and the Eastern Atlantic. In both reanalyses, this produces contributions between 600 and 800 hPa of 0.1–0.2 day^{-1}. In addition there is a similar contribution to growth in the low-levels over the Atlantic.

Given that the AEW-scale PV has a quasi-balanced circulation, it is initially unclear how these winds advect background PV such that growth occurs. Conceptually, this may be best interpreted using a framework similar to the Eady model for baroclinic instability (Eady 1949). Here we assume that PV anomalies project a circulation over a larger area (horizontally and vertically) than their own signature. From this perspective, we can think of this term as representing the cross-advections of two phase-locked counter-propagating RWs. Given that we have tilts of the AEW-scale PV in both the horizontal and vertical,

AEW-scale advection of the background vorticity can enhance the AEW.

Assuming a fractional growth rate of 0.15 per day by $-V_w \cdot \nabla \bar{P}$ and beginning with a PV anomaly over East Africa of magnitude 0.015 PVU (e.g. Figures 4.3c and 4.4c), at or around the West African coast after approximately 7 days (5000 km at approximately 8 ms^{-1}) we can expect a PV anomaly of 0.04 PVU. This is only around half the magnitude of that shown in our composite AEWs near the West African coast (Figures 4.3a and 4.4a). Further, this does not explain the maximum in PV that occurs above 600 hPa. Thus, we must look to other sources to explain the total growth of AEW-scale PV.

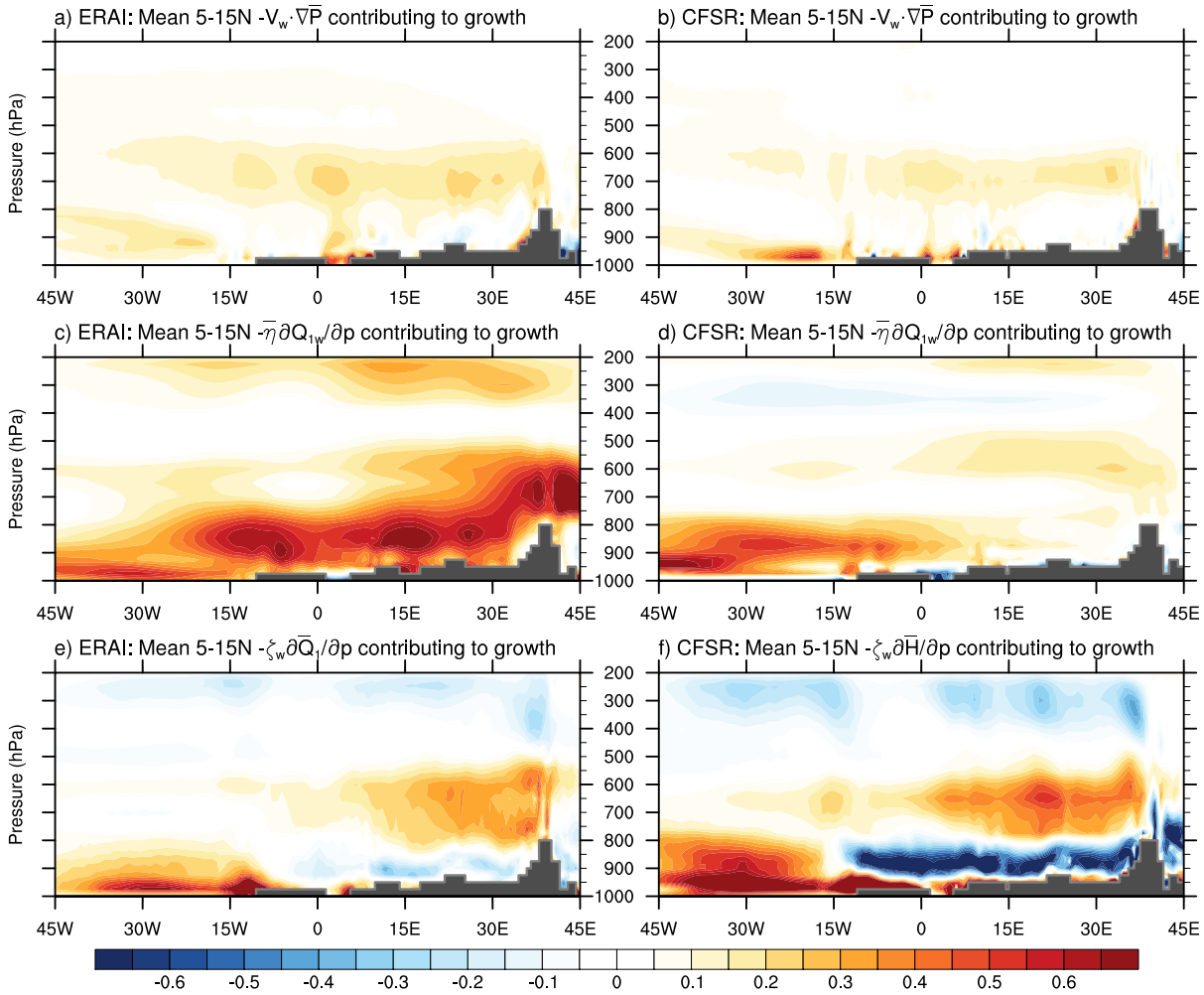

Figure 4.12: Longitude-pressure cross-sections as in Figure 4.11 but for fractional growth. a,c,e,g) are for ERAI and b,d,f,h) are for CFSR. a,b) show $-V_w \cdot \nabla \bar{P}$, c) shows $-\bar{\eta}\partial Q_{1w}/\partial p$, d) $-\bar{\eta}\partial H_w/\partial p$, e) shows $-\zeta_w \cdot \nabla \bar{Q}_1$, and f) shows $-\zeta_w \cdot \nabla \bar{H}$.

The contribution to growth associated with vertical gradients in AEW-scale diabatic heating ($-\bar{\eta}\partial Q_w/\partial p$) is shown in Figure 4.12c and 4.12d. In ERAI over East Africa there is a large contribution below 500 hPa of 0.4-0.7 day^{-1}. However, in CFSR this is only 0.1-0.2 day^{-1}. This quite considerable difference in growth highlights how small variations in the heating profile (Figure 4.6c and 4.6i) can vary the structure of the PV source (Figures 4.8f and 4.9f), and thus the magnitude of growth. Nonetheless, both suggest growth of the PV anomaly over eastern, and to a lesser extent central Africa, between 500 and 700 hPa, coincident with the maxima in the AEW-scale PV (e.g. Figures 4.3c and 4.4c).

In addition, the mid-level contribution to growth associated with vertical gradients in time-mean diabatic heating (-$\zeta_w \cdot \nabla\bar{Q}$) is associated with a growth of PV between 500 and 800 hPa of 0.2–0.35 day^{-1} (Figures 4.12e and 4.12f). Over East Africa, nearly every day during JAS there are large MCSs occurring and thus the background heating here is dominated by large regions of stratiform cloud - the predominant cloud type from MCSs on these scales. Thus heating is maximized between 400 and 500hPa and the generation of PV is positive below this maxima. This source represents stretching of the vorticity since both anticyclonic and cyclonic vorticity will be amplified when they come into contact with such time-mean heating gradients. While this source and the AEW-scale diabatic source diminish over West Africa, they account for the growth of PV observed between East and West Africa (e.g. compare Figures 4.6c and 4.6f with Figures 4.6b and 4.6e respectively).

In the low-levels, there are large contributions by gradients in the AEW-scale diabatic heating (Figures 4.12c and 4.12d). ERAI produces growth of between 0.5-0.7 day^{-1} centered at 850 hPa across a broad region from 30°W to 30°E. In CFSR, the growth of low-level AEW-scale PV by this source is shifted west of 15°E but also produces large contributions to growth, between 0.2–0.6. This implies that the growth of low-level AEW-scale PV is dominated by the AEW-scale diabatic heating.

Vertical gradients in the time-mean heating generate large contributions over the ocean below 800 hPa. This is associated with the high density of deep moist convection in the ITCZ over ocean. Thus both time-mean and AEW-scale diabatic heating support the growth of a low-level circulation over ocean. Over land, there is a negative contribution below 800 hPa by this source. This is likely associated with the low-level gradient in evaporative cooling below the time-mean stratiform cloud. This offsets the growth by AEW-scale heating that enhances the low-level PV anomaly attendant with the AEW.

4.6 Discussion

From the perspective of propagation there are two different regimes in the southern track AEW. One is in the mid and upper levels over land, and also over ocean, where the AEW propagates like a RW. Here the background flow and beta-effect are the dominant processes. The other is in the low-levels over land, where the AEW propagates via diabatic processes. Here the AEW-scale diabatic heating is the dominant process. An enhancement of PV in the low-levels is characteristic of deep moist convection (as opposed to trailing upper-level stratiform cloud). Since deep moist convection is coupled to the northerlies of the mid-level AEW (i.e. Chapter 3), this suggests that there is a coupling between a mid-level dry wave and a low-level moist wave.

The growth mechanisms for this system are somewhat more complicated. There are conducive upshear tilts of the AEW in the horizontal implying growth by barotropic instability between counter-propagating waves on the mid-level positive and negative PV gradients. In our PV budget, barotropic instability is represented by the growth via AEW-scale advection of the time-mean PV ($-V_w \cdot \nabla \bar{P}$). This process is described in the first row of Table 4.2.

Dry baroclinic instability is limited to the northern track AEWs since there are only conducive upshear tilts and PV gradients to the north. While the northern track is clearly coupled to the mid-level southern track, it is still unclear how they interact. Its likely that the projection of winds by the northern track PV anomaly will also contribute to growth via advection of the time-mean PV (represented by $-V_w \cdot \nabla \bar{P}$ in our PV budget). This interaction is highlighted in the second row of Table 4.2.

Some form of moist instability has also been proposed as a growth mechanism for AEWs (Berry and Thorncroft 2005). In our analysis we see evidence for interactions between moist and dry waves with favorable upshear tilts for instability. As discussed earlier, an upper-level dry wave is coupled to a lower-level moist wave in the southern track. The third row in Table 4.2 describes the potential interaction between these two. The upper-level dry wave generates moist convection to the west of its PV anomaly as discussed extensively in Chapter 3. This moist convection will enhance the low-level moist wave (e.g. Figures 4.12c and 4.12d) through diabatic generation of PV. In the PV budget, this process is represented by contributions via AEW-scale diabatic heating ($-\bar{\eta}\partial Q_w/\partial p$). Via the projection of the low-level moist waves flow on the upper-level dry wave, a horizontal advection will enhance the upper-level wave. In the PV budget this process will be represented by growth contributions via AEW-scale advection of the time mean PV ($-V_w \cdot \nabla \bar{P}$). Thus there may be a favorable interaction for growth between the low and mid levels of the southern track.

Table 4.2: Possible interactions between waves in the AEW. PV anomalies are denoted by P with ^{d} for dry waves and ^{m} for moist waves, and $_{low}$ for low-level waves and $_{mid}$ for mid-level waves. Q represents induced diabatic processes enhancing a moist wave and v represents an induced cross-advection enhancing a dry wave. PV gradients referred to are those shown in Figure 4.2.

Instability	Waves Involved	Interactions
Barotropic Instability	Two mid-level dry waves (positive and negative PV gradients)	$P^d_{mid} \rightarrow v \rightarrow P^d_{mid} \rightarrow v \rightarrow P^d_{mid}$
Dry Baroclinic Instability	Mid-level dry wave (negative PV gradient) and surface dry wave (northern track)	$P^d_{mid} \rightarrow v \rightarrow P^d_{low} \rightarrow v \rightarrow P^d_{mid}$
Moist Instability	Mid-level dry wave (negative PV gradient) and low-level moist wave (both southern track)	$P^d_{mid} \rightarrow Q \rightarrow P^m_{low} \rightarrow v \rightarrow P^d_{mid}$

Previous studies have suggested the applicability of the DRW conceptual model to AEWs. We argue that the AEW system does not resemble a canonical DRW even though in both cases the low-level moist wave is generated via diabatic heating. The difference is that in a canonical DRW, convection is coupled to isentropic ascent in a region of strong meridional temperature gradient. Although in Chapter 3 we showed that ascent plays a role in the organization of moist convection, other factors such as moisture, temperature, and shear are important. Further, the low-level moist wave in the southern track is not associated with strongly sloping isentropes. As shown by Hannah and Aiyyer (2017), the dynamical scaling for the southern track AEWs is more appropriately described by the weak temperature gradient (WTG) approximation. In addition, unless the northern track surface wave plays a role in organizing moist convection, there is no coupling between a surface dry wave and the low-level moist wave in the southern track. There is also no evidence of strong tilts between the surface northern track dry wave and the low-level southern track moist wave. Thus the growth mechanism for DRWs described by Cohen and Boos (2016) is likely not present in AEWs.

Finally, as we showed in the previous section, the contribution to growth by AEW-scale advection of the time-mean PV only accounts for around half of the total growth of the mid-level AEW and does not explain the growth of PV above 600 hPa. Further, other terms such as the AEW-scale and background heating contribute more strongly to growth of the

mid-level AEW, especially over East Africa. In the next chapter we will examine the details of moist convection to account for the latter processes.

4.7 Summary

In this Chapter we have evaluated the dynamics of AEWs from the perspective of PV. Our aim was to understand the structure of PV and PV sources relative to the AEW, with a focus on the role of diabatic processes; questions 1 and 2 in Section 1.7.2.

From the perspective of propagating RWs, the mid-level southern track of AEWs acts like a RW, whilst the low-level wave in the southern track propagate through diabatic processes. These waves are coupled to each other via the generation of moist convection in the northerlies of the mid-level AEW. Whilst the necessary environmental conditions and PV structure for barotropic and baroclinic instability exist, even when considering a form of moist instability, instabilities do not completely explain the growth of AEWs. Rather, vertical gradients in AEW-scale and background diabatic heating contribute most strongly to the growth of mid-level PV, especially over East Africa.

Moist convective coupling to the AEW is essential for the enhancement of low-level circulation. Without coupled moist convection, the background flow would tilt the PV column downshear due to the environmental shear between low-level monsoon westerlies and the AEJ. The continual generation of new PV by deep moist convection in the northerlies maintains a column with an upshear tilt. Further, the transition of moist convection from the northerlies over land, to the trough over ocean, is important for deepening and maintaining a more upright PV column after the AEW leaves the West African coast. There are significant implications here for the generation of TCs since a low-level circulation is positively correlated with TC genesis (Russell et al. 2017).

By analyzing an AEW-scale PV budget, we show that the dominant terms contributing to the dynamics of AEWs are $-\bar{V}\cdot\nabla P_w$, $-V_w\cdot\nabla\bar{P}$, $-\bar{\eta}\partial Q_w/\partial p$, and $-\zeta_w\partial\bar{Q}/\partial p$. Future work should focus on confirming that this system will represent AEWs. The dominant PV source terms might be used to represent AEWs in an idealized model. If the system described here sufficiently explains the dynamics of AEWs, we should be able recreate the main features of the AEW in such an idealized model. This will be discussed further in the last Chapter.

CHAPTER

5

ROLE OF MOIST CONVECTION

This chapter examines the two AEWs in the 2007 and 2010 simulations, with a focus on the role of the resolved moist convection in the dynamics of the AEWs. The analysis here will build on the previous chapter by examining how the structure of moist convection leads to an enhancement of mid-level rotation; research question 2 in Section 1.7.2. Further we will also assess the difference in the structure and dynamics of an AEW when no moist convection is present by using the sensitivity studies documented in Section 2.1.3; research question 3 in Section 1.7.2. Finally, we will aim to conclude by addressing which aspects of DRWs and stratiform instability are present in the AEW; the first research question posed in Section 1.7.3. PV and the corresponding budget are again utilized since these tools are strongly suited to diagnosing the effect of diabatic processes.

5.1 AEWs in Convection-Permitting Simulations

5.1.1 Dynamics of the AEWs

Figure 5.1 shows time-longitude diagrams of the 400–800 hPa and 5-20°N averaged perturbation PV and various perturbation PV source terms (Equation 2.24). We use a perturba-

tion PV budget since we do not have global data or a sufficiently long time-series to use space-time filtering. Here, the time-mean is defined as the simulation time-mean. For the time-longitude diagram, these levels are chosen since this is the range where perturbation PV is maximized in the AEW (see Figure 5.5). This range of latitudes is chosen since it encompasses the centroid of the AEW as shown by the tracks in Figure 2.1.

Figures 5.1a and 5.1b show the advection of perturbation PV by the time-mean (background) winds in the 2007-CTRL and 2010-CTRL simulations respectively. This source is in quadrature with the AEW indicating that it contributes most strongly to the propagation. Further it is also much larger than other sources indicating that it dominates the ground relative propagation of the AEW, as in the composite AEWs in Chapter 4. Horizontal advection of mean PV by perturbation flow (Figures 5.1c and 5.1d) produces a consistent negative PV source in and behind the trough in both simulations with a consistent positive PV source ahead of the AEW. This indicates that this source is also primarily contributing to forward propagation of the AEW.

Here we have shown the diabatic source as the total diabatic source added to the vertical advective source since the vertical advective source often counteracts diabatic sources in deep moist convection when in a non-isentropic framework. This issue with the non-isentropic PV tendency equations is discussed in depth in Tory et al. (2012) where they refer to it as the adiabatic-diabatic cancellation problem. In our simulations though, vertical advection is not as large as the diabatic contribution since we are examining variables smoothed over a larger scale than individual convective updrafts, and because PV generation at mid-levels, as we will show, is most often associated with stratiform cloud regions that exhibit weak vertical motions (not shown).

In both simulations there are positive diabatic sources in and ahead of the trough indicating that they may contribute to both growth and propagation. This source is notably larger than the horizontal advection by perturbation winds and at its largest, is of similar magnitude to the horizontal advection by mean winds. It is transient in nature, indicating that any growth or propagation of the AEW by diabatic sources is not a steady coherent process. If we examine the meridional winds in Figure 2.2d the AEW is strengthening east of 5°E. At the same time there is a strong diabatic source of PV. When the AEW is west of 0°, the meridional winds in the AEW are decaying. At the same time there is a negative diabatic source in the trough while there is a positive diabatic source of PV ahead of the trough. A similar situation occurs in the 2007-CTRL simulation between 10°W and 20°W. These examples tentatively indicate that the strength of the AEWs in the control simulations is coupled to the diabatic source of PV.

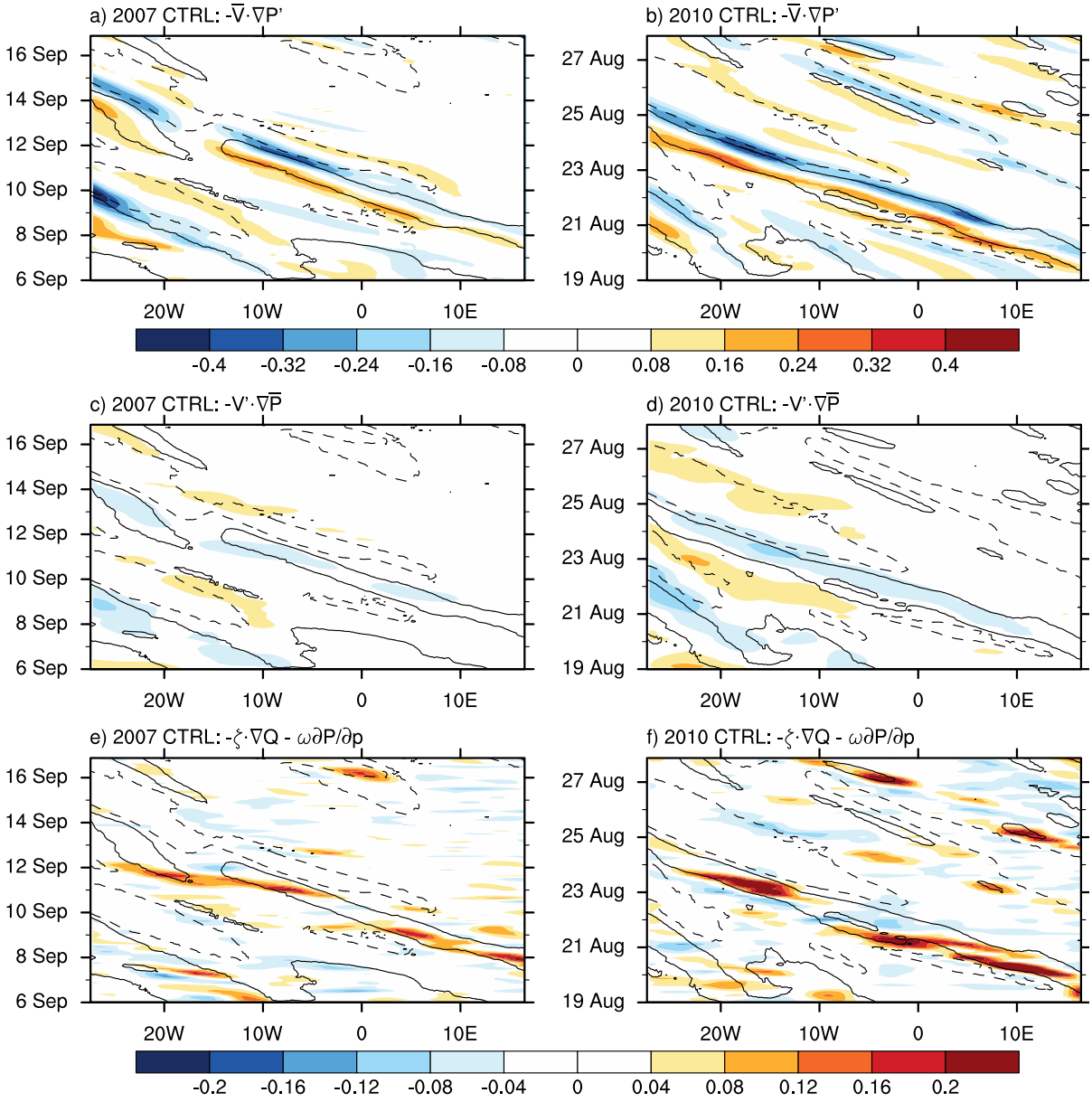

Figure 5.1: Time-longitude plots of 5-20°N and 400-800 hPa averaged perturbation PV (PVU, 0.05PVU solid contour and -0.05PVU dashed contour) and PV sources (PVU/day, shades) for the a,c,e) 2007-CTRL AEW and b,d,f) 2010-CTRL AEW. The sources represented are a,b) $-\bar{V}\cdot\nabla P'$, c,d) $-V'\cdot\nabla\bar{P}$, and e,f) $-\zeta\cdot\nabla Q+\omega\partial P/\partial p$.

To understand exactly how these sources are contributing to AEW dynamics we separate sources into those contributing to growth (or decay) and propagation of the perturbation PV. Similarly to Section 4.5, this is achieved by calculating a correlation of the source term with either the perturbation PV:

$$Y_g = \langle Y \cdot P' \rangle \Big/ \langle P' \cdot P' \rangle \tag{5.1}$$

or the time change in perturbation PV:

$$Y_p = \left\langle Y \cdot \frac{\partial P'}{\partial t} \right\rangle \Bigg/ \left\langle \frac{\partial P'}{\partial t} \cdot \frac{\partial P'}{\partial t} \right\rangle . \tag{5.2}$$

In this case the average, $\langle\rangle$, is over an area 3000km zonally by 2000km meridionally following the AEW troughs. This region is chosen as it encompasses the region where the PV perturbation for the AEW is largest. To examine the differences between AEW growth and propagation over land versus over ocean, we calculate one time average for times while the AEW is over land and a separate time average after the AEW propagates past the coast. For this analysis Y_g and Y_p are also averaged over 800-400 hPa where the PV in the AEW is largest. These are shown in Figure 5.2.

The growth of the AEW over land is strongly characterized by microphysical diabatic processes. Over the three days during which the AEW is over land, this process produces the largest average fractional contribution to growth; 0.24 per day in 2007-CTRL and 0.32 per day in 2010-CTRL. Other diabatic processes contribute little to the growth of the AEWs indicating that processes associated with clouds and precipitation are the dominant diabatic source of PV in Figure 5.1. Other contributors to growth include the advection of background PV by the mean wind; up to 0.1 per day. As discussed in Section 4.6 this source represents cross-advections associated with barotropic and baroclinic instability. Thus while these instabilities are present, they are clearly not the dominant processes enhancing AEWs in the CTRL simulations. Other processes including nonlinear advection and friction also produce small negative contributions to the PV; notably enough to offset the positive contribution via the perturbation advection of time-mean PV. These last two findings are consistent with the results of Hall et al. (2006) that baroclinic and barotropic instability cannot maintain an AEW in the presence of damping processes with typical observed magnitudes.

The propagation of the AEW over land is characterized by a number of different processes. The dominant process for propagation is the mean flow as discussed earlier and in Chapter 4. The fractional contribution is approximately 0.55 in 2007-CTRL and 0.5 in

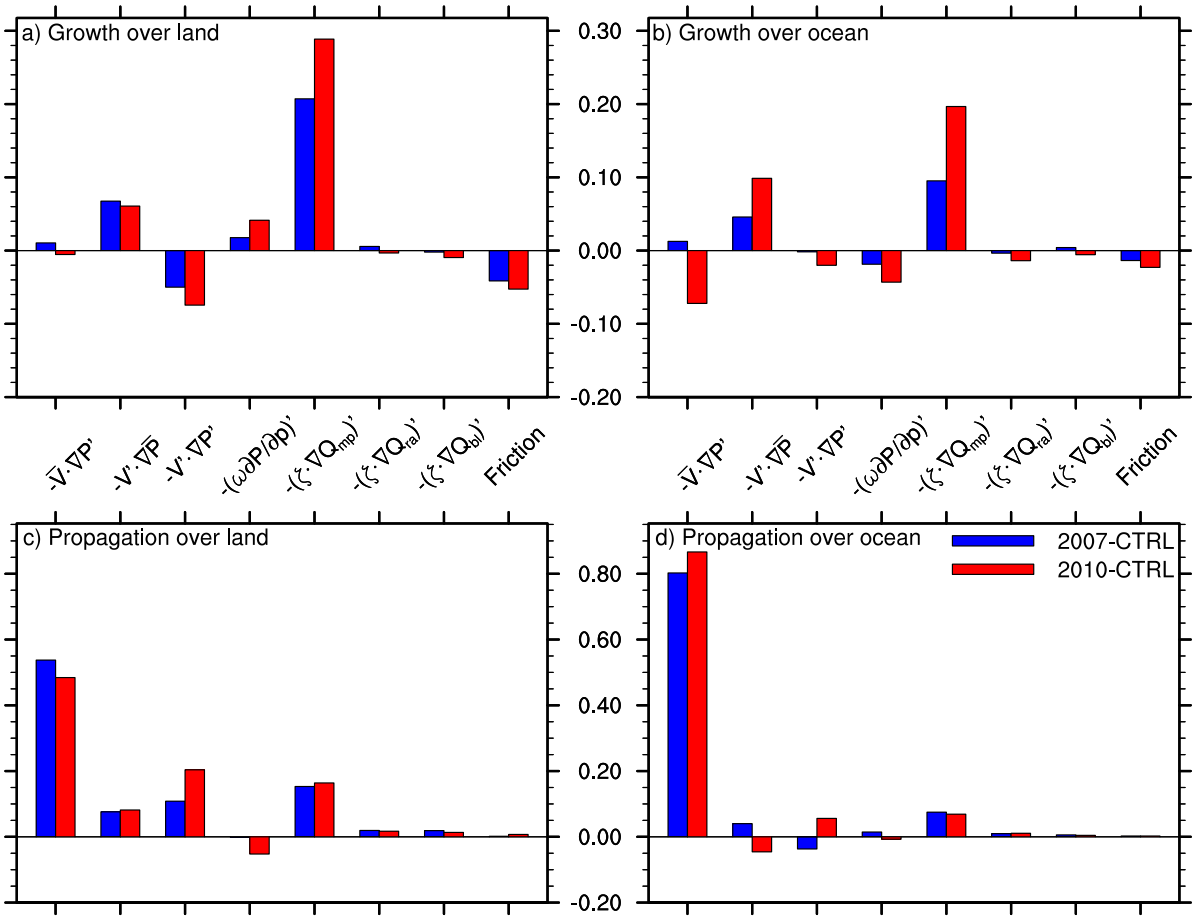

Figure 5.2: Bar charts showing the fractional contributions to a,b) growth (equation 4.1; per day) and c,d) propagation (equation 4.2; no units) by various PV sources. Sources are averaged over 800-400 hPa and in time. Averages in time are separated into when the wave center was over a,c) land and b,d) ocean. Blue bars are for the 2007-CTRL simulation and red bars are for the 2010-CTRL simulation.

2010-CTRL. In both AEWs, Rossby wave propagation, nonlinear advection, and microphysical diabatic processes account for the remainder of the propagation. Again, other diabatic processes are negligible. These results imply that the background-flow-relative phase speed of the AEWs is contributed by both diabatic and adiabatic processes.

Over ocean, the main contributions to growth of the AEWs are from instabilities of the background flow, which are of a similar magnitude to that over land, and microphysical diabatic processes, which are approximately double that of the contributions by instabilities. In both AEWs, diabatic processes contribute much less over ocean than over land. Similar to over land, there are a few processes contributing to decay of the AEWs. The propagation of the AEW is dominated by the background flow over the ocean, with the only other consistent contribution from microphysical diabatic processes at around 0.1.

A more in depth analysis of the growth of the AEWs is presented in Figure 5.3. Here we analyze the temporal and vertical distribution of fractional growth in the AEW. Close to the surface, there is large fractional growth by all the source terms shown. However, since the magnitude of the diurnal variation of PV is much stronger than the AEWs perturbation PV, this surface PV growth does not represent growth of the AEW. In Figures 5.3a and 5.3b the contribution to growth via perturbation advection of time-mean PV occurs between 800 and 600 hPa. This is consistent with contributions to growth by $-V_w \cdot \nabla \bar{P}$ in composite average AEWs shown in Chapter 4. In 2007 this is primarily over land while in 2010 this is primarily over ocean. These levels are where the background PV gradient reverses allowing for the term to contribute to growth (Charney and Stern 1962).

Nonlinear advective processes (Figures 5.3c and 5.3d) produce transient decay of the AEW, most notably on the 20th September in the 2010 simulation. This transience indicates that this is not a consistent feature of AEWs. Since it occurs most strongly at a time when there is strong convective activity in and around the AEW (Figure 5.4), it's possible that this decay occurs as a result of strong moist convection modifying the perturbation PV of the AEW at this time.

The largest contribution to growth as a result of microphysical diabatic processes (Figures 5.3e and 5.3f) occurs between 700-500 hPa, although at times this growth can stretch to the low-levels. This growth occurs in transient bursts on the diurnal time scale but is not accompanied by a diurnal damping. This diurnal pulsing is not surprising since MCS activity is often linked to the diurnal cycle (Laing et al. 2011). This indicates that growth of the AEW occurs in bursts related to the AEW-relative behavior of convective activity.

Figure 5.4 provides a similar analysis of the contributions to propagation of perturbation PV following the AEWs. Perturbation advection of mean PV contributes positively to

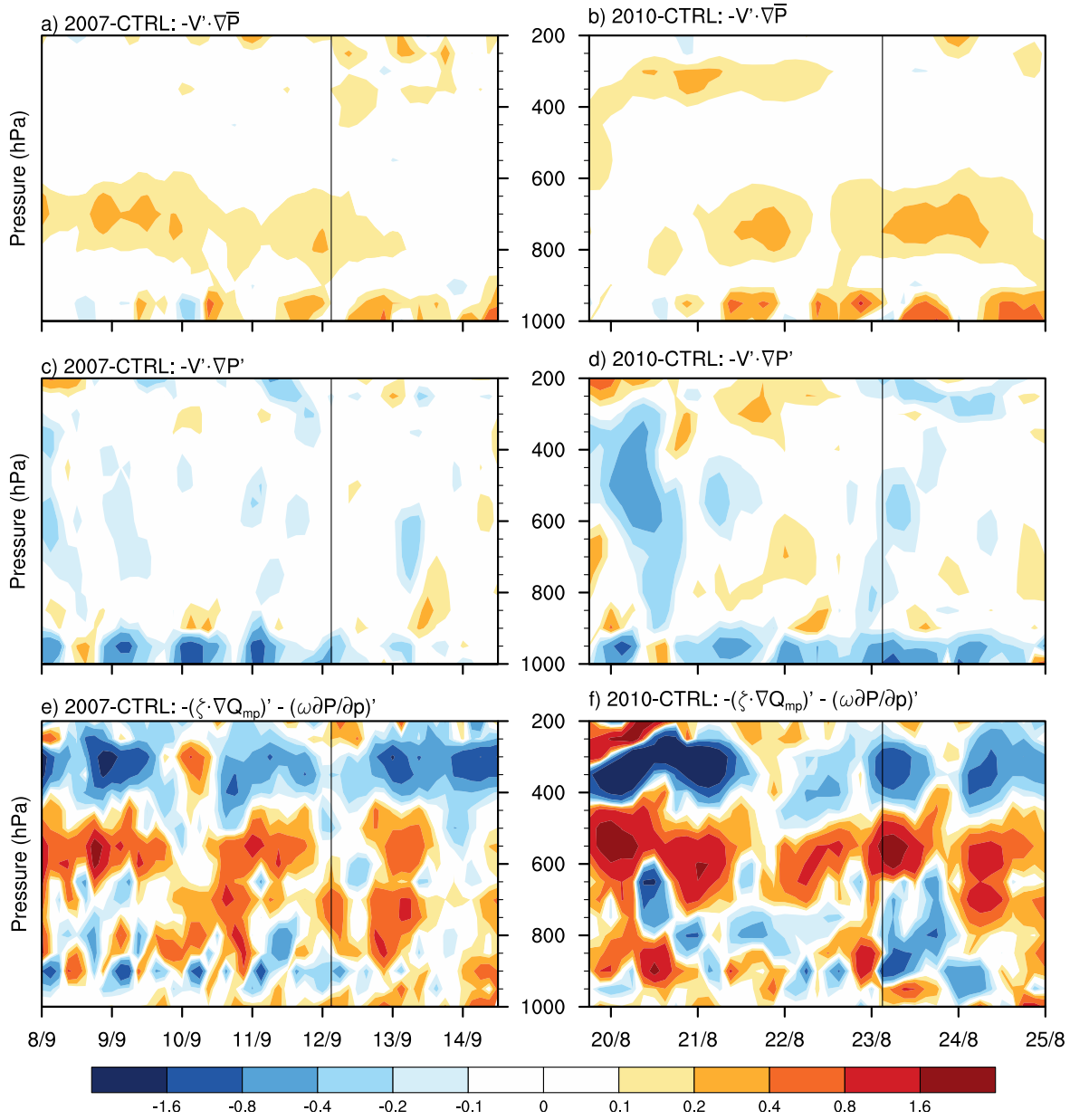

Figure 5.3: Fractional contribution to growth of perturbation PV (units of per day) by various perturbation PV sources. Plots are time-pressure cross-sections following the tracked AEW trough center for a,c,e) 2007-CTRL and b,d,f) 2010-CTRL. Sources shown are fractional contribution to growth by a,b) $V' \cdot \nabla \bar{P}$, c,d) $V' \cdot \nabla P'$, and e,f) $(\zeta \cdot \nabla Q_{mp})'$ (PU, contours). The individual vertical black lines indicate the point at which the trough passes the West African Coast. Note scale is not linear, scale doubles for each color.

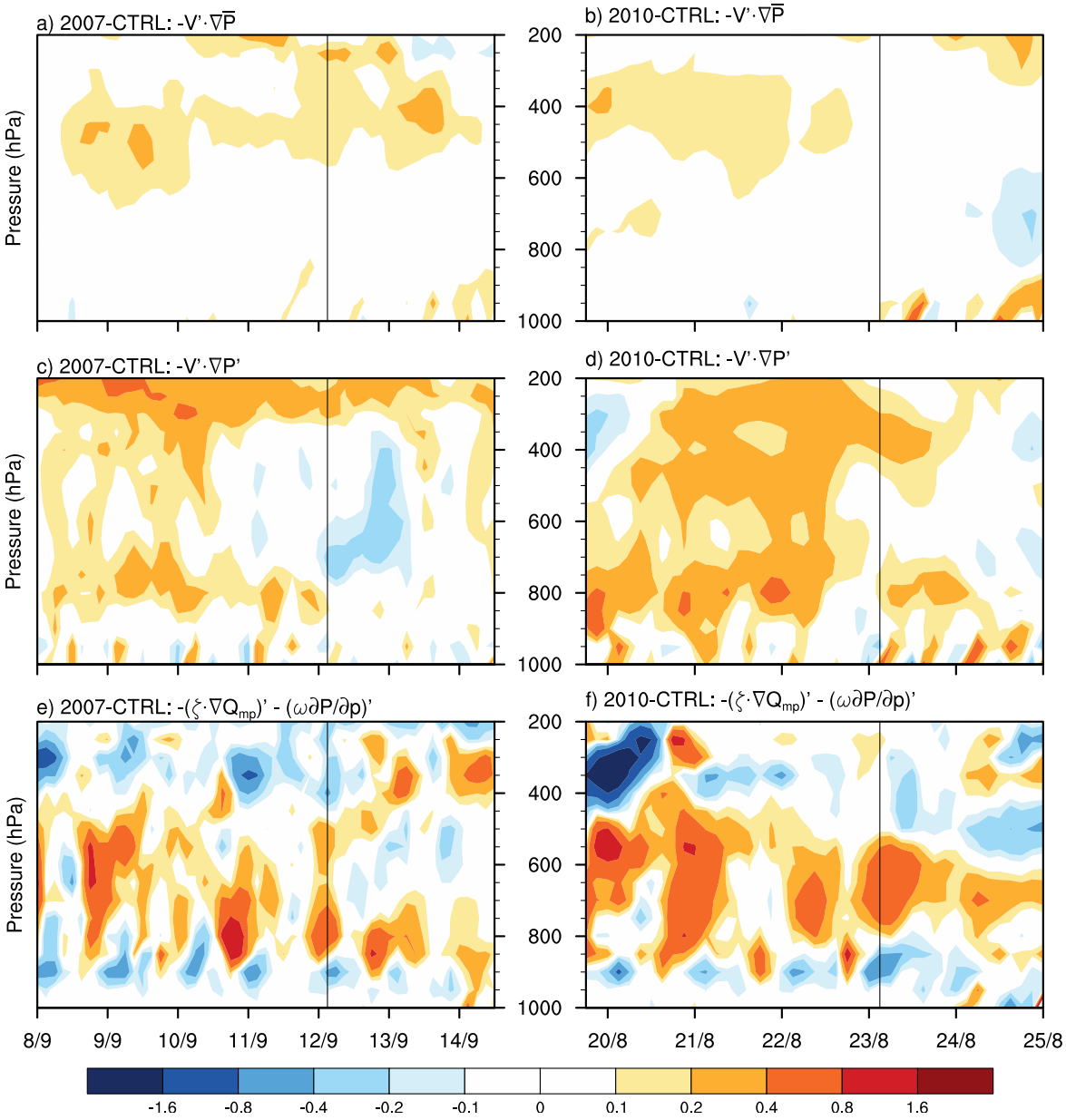

Figure 5.4: As in Figure 5.3 but for fractional contribution to propagation (no units).

propagation above 600 hPa, although again this term is relatively small in magnitude. At these levels the background PV gradient does not reverse which allows for this term to contribute to propagation rather than growth.

Over land, there are contributions to propagation by nonlinear advective processes. Fractional contributions are strongest at 800 hPa but are positive at most levels. This term contributes most in the 2010-CTRL simulation while it is relatively weaker in the 2007-CTRL simulation. Examination of the 2010-CTRL simulation shows that this term varies with the diurnal cycle. To a lesser extent the 2007-CTRL simulation also exhibits a diurnal cycle. This, and the fact it plays a much larger role in the 2010-CTRL simulation which exhibits stronger convective activity, indicates that this term may be related to deep convective activity.

Finally the largest contribution in magnitude is the diabatic source related to clouds and precipitation. This term contributes most between 800 and 500 hPa. The transience indicates that the perturbation PV anomaly will propagate forward in 'bursts'. In Figure 5.1e, there is a good example of this process. On the 12th September, there is a break in the PV at 15W and it reforms at the same time at 20W. This 'jump' in PV westward corresponds to a strong diabatic PV source. Examination of the perturbation PV anomaly in maps (not shown) also reveals this behavior.

5.1.2 Role of Moist Convection

The analysis in the previous section and in Chapter 4 revealed that the dominant PV source contributing to growth of AEWs, and in some cases to the propagation of AEWs, is diabatic processes associated with clouds and precipitation. Typically diabatic PV production by deep moist convection occurs at the location where the vertical gradient of diabatic heating is strongest; in deep moist convection this is usually in the low-levels near the surface. In DRWs, this process is often driven by low-level stratiform cloud regions forming as a result of isentropic lifting which then generates PV relatively close to the surface. However, we have seen here that these processes contribute to the growth of PV in the mid-levels, often between 800 and 400 hPa. This leaves the question of how processes associated with clouds and precipitation are enhancing PV in the mid-levels. In this section, we will investigate what is driving these mid-level diabatic PV sources.

Time-Averaged View

Figure 5.5 shows longitude-pressure cross-sections averaged over three days (while the AEW is over land) and over a latitudinal line 250 km either side of the tracked trough center.

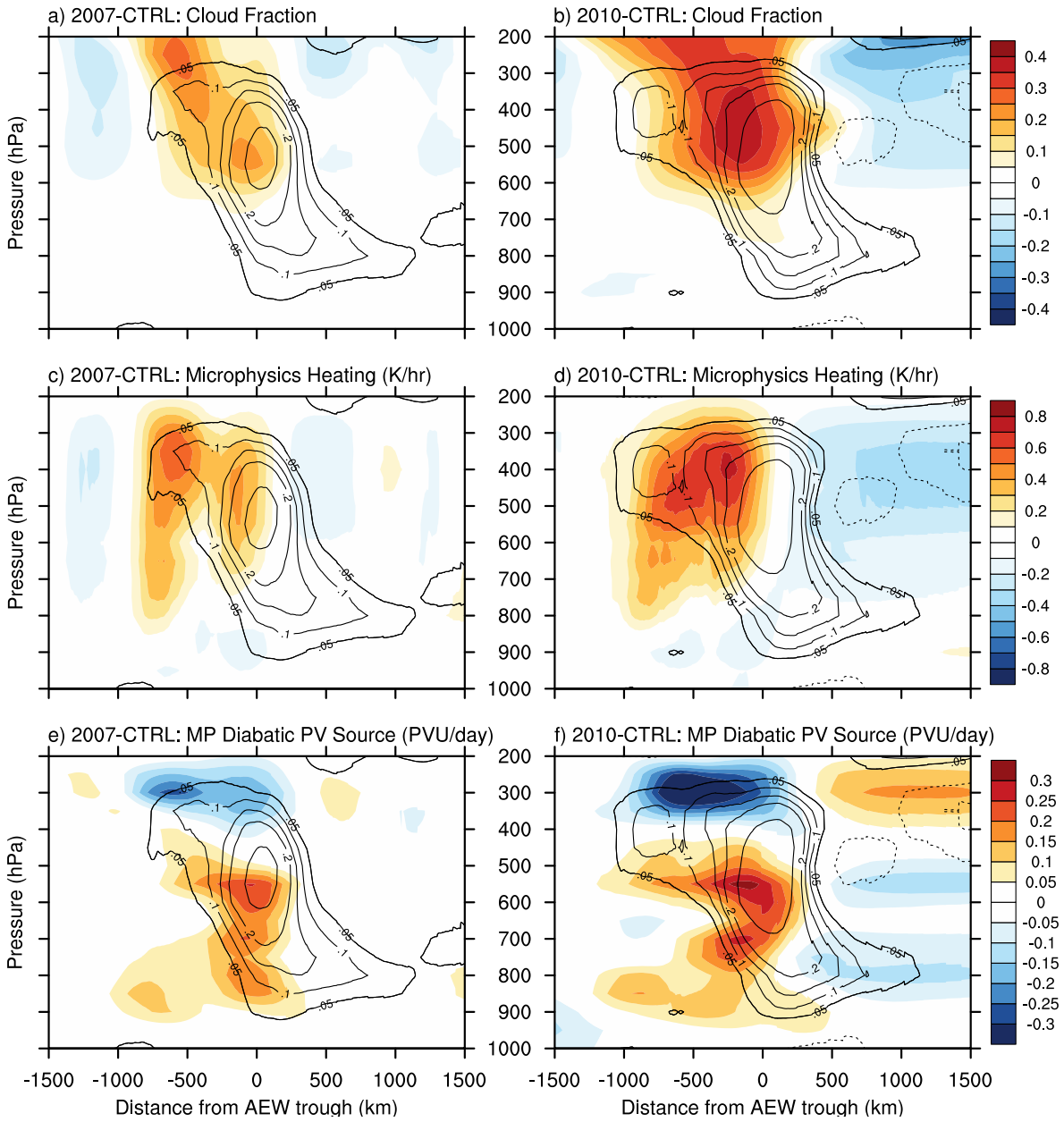

Figure 5.5: Longitude-pressure cross-sections following the tracked AEW trough center for a,c,e) 2007-CTRL and b,d,f) 2010-CTRL. Cross-sections are averaged over an area 250km north and south of the trough center and averaged over the 3 days while the AEWs are solely over land. Variables shown are perturbation PV (PU, contours) and a,b) perturbation cloud fraction, c,d) perturbation microphysical heating, and e,f) perturbation diabatic PV source using only microphysical heating.

The perturbation PV in both AEWs is tilted from east to west with height, with maximum PV between 700 and 400 hPa. This is consistent with the composite PV structure in Chapter 4 indicating that these AEWs are representative of the larger population of AEWs.

Figures 5.5a and 5.5b show the perturbation cloud fraction. In both simulations, cloud fractions are largest above 600 hPa and peak at and to the west of the strongest perturbation PV. This indicates that there is a preference for expansive regions of mid–upper level cloud in the trough and northerlies. Outside of this region there are negative perturbation cloud fractions indicating a suppression of mid–upper level cloud in the southerlies and ridge.

Figure 5.5c and 5.5d show the perturbation microphysics heating rates. Where there are negative perturbation cloud fractions there are negative perturbation microphysics heating rates, indicating more cooling than usual in these regions. This can be interpreted as a suppression of the mean moist convection typically present over the Sahel during these times. At and ahead of the AEW trough there is a deep column of perturbation heating between 800 and 300 hPa. This is top heavy, i.e. the strongest heating rates are above 500 hPa. Closer to the trough this column of heating gets shorter but remains top heavy.

We interpret these cloud and heating structures as follows. Ahead of the AEW in the northerlies there is a prevalence for deep moist convection. This manifests in the deep but top heavy heating profiles because there is a mix of deep moist convection and trailing stratiform cloud. In the trough, there is less deep-moist convection and more trailing stratiform cloud. Corroborating evidence for these interpretations includes the typical heating profiles of deep moist convection and stratiform clouds in tropical regions (e.g. Schumacher et al. 2007), as well as Janiga and Thorncroft (2013) who showed that stratiform cloud is more prominent in the trough of AEWs.

These prominent cloud structures manifest in the AEW-relative distributions of the diabatic PV source shown in Figures 5.5e and 5.5f. To the west of the trough there is weak, low-level diabatic PV production as a result of the prominence for deep moist convection. This likely contributes to the propagation of the AEW PV anomaly in the low-levels, as in the composite AEWs in Chapter 4. In the trough, where there is a stronger fraction of trailing stratiform cloud, there is stronger diabatic production of PV through a deeper column. This diabatic PV production peaks at and just to the west of where the PV is maximized in the mid-levels. This PV production by the heating associated with trailing stratiform cloud regions then contributes to growth of the AEW PV anomaly as shown in Figures 5.2a, 5.2b, 5.3e, and 5.3f. There is also production of negative diabatic PV at approximately 300 hPa, in association with the negative vertical gradient of heating. This production of negative PV atop the microphysics heating region contributes to the destruction of perturbation PV

(Figures 5.3e and 5.3f) and limits the AEW PV anomaly to levels below 300 hPa.

Snapshots

For both simulated AEWs, stratiform cloud regions appear to be important for the AEWs maintenance. In order to understand this process in more detail we examine cross-sections through the AEWs at various times. Figure 5.6 shows horizontal and vertical cross-sections from the 2007-CTRL simulation. Horizontal cross-sections on the left show perturbation PV (black contour) and maximum radar reflectivity (shades). Vertical cross-sections on the right show cloud fraction (shades) and the perturbation diabatic PV source averaged over the region of the perturbation PV contours.

At 12 UTC on the 8th September there is a broad region of positive perturbation PV associated with the AEW trough centered at approximately 10°E (Figure 5.6a). At this time, there is one strong bowing MCS approaching the Gulf of Guinea coast at the head of this region of positive PV, as shown by the maximum radar reflectivity. This is accompanied by convection to the south east in association with an earlier MCS, and a small amount of convection initiating to its north. Deep moist convection makes up a very small fraction of this region, as represented by the 40 dBZ and greater reflectivity. In contrast the strong MCS has an expansive region of trailing stratiform cloud as represented by the 20–40 dBZ areas trailing the deep moist convection. Further there are broad regions of remnant stratiform cloud left over by the previous days MCSs as represented by other regions of reflectivity with less than 20 dBZ.

The prevalence of trailing stratiform cloud is apparent in the latitudinally averaged cloud fractions shown in the longitude-pressure cross-section of Figure 5.6b, corresponding to the same time as in Figure 5.6a. The cloud fractions shown represent the main MCS present at the time. There is a deep column of low cloud fraction at around 5°E but the highest cloud fractions are predominantly trailing this column aloft between 600 and 150 hPa. The lower gradient of this trailing stratiform cloud is associated with diabatic PV generation of greater than 0.25PVU/day between 550 and 450 hPa and between 6°E and 10°E. This process is similar to those described in Fritsch et al. (1994) and Davis and Weisman (1994). Thus the generation of PV indicates an MCV formed in association with this MCS. There is also a similar region of diabatic PV generation between 950 and 850 hPa and between 4°E and 8°E that is connected with the low-level gradient in deep convective cloud fraction.

At 03 UTC on the 9th September (15 hours later; Figure 5.6c and 5.6d) the MCSs shown in Figure 5.6a have decayed leaving some light precipitation along the coast between

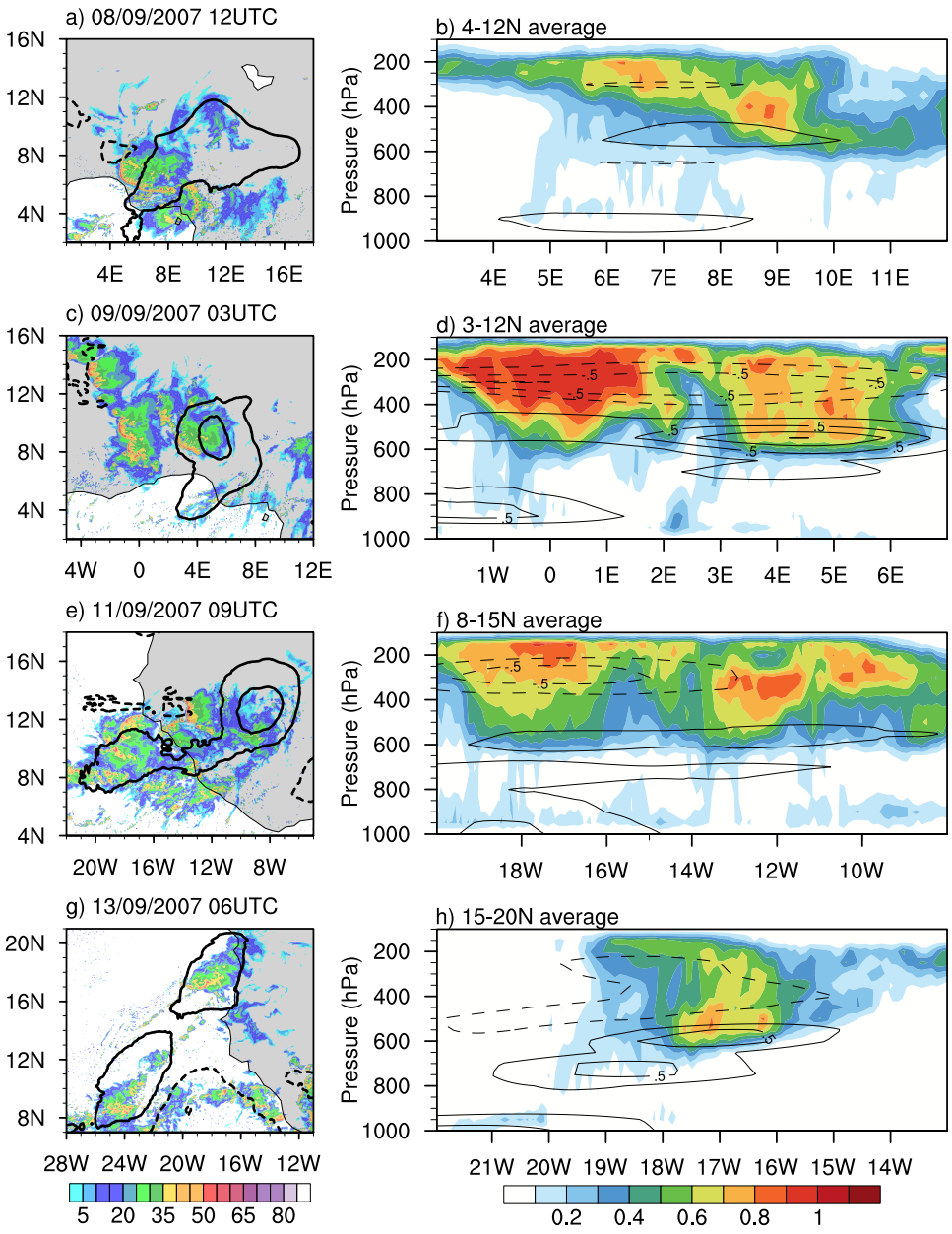

Figure 5.6: Cross-sections in the 2007-CTRL simulation at times when diabatic PV production is producing growth (Figure 5.3f). a,c,e,f) Horizontal cross sections of maximimum radar reflectivity (shades) and 400-800 hPa averaged perturbation PV (contours). PV contours are at intervals of 0.1 PVU. b,d,f,h) longitude-pressure cross-sections of cloud fraction (shades) and perturbation diabatic PV production by microphysical heating (contours) averaged over longitudes corresponding to the perturbation PV on the left. Diabatic PV source contours are at intervals of 0.25 PVU/day.

4°E and 8°E. The convection to the north is now an MCS with an expansive stratiform cloud region trailing back into the AEW trough. Further, an MCS has developed ahead in the northerlies with deep convection along 1°W. The perturbation PV near the coast has propagated westward about 5° while the northernmost perturbation PV is much stronger and has propagated westward much quicker to around the same longitude as that of the southernmost perturbation PV.

A cross-section through this region shows cloud fractions representing these MCSs. The trailing stratiform cloud region associated with the easternmost MCS is generating upwards of 0.25 PVU/day between 700 and 450 hPa and between 3-6°E; a region associated with the peak perturbation PV. The diabatic heating processes associated with the westernmost MCS are generating PV at these levels but to a smaller extent. Additionally, it generates PV in the low-levels below 800 hPa. The rapid propagation and growth of the northernmost PV during this 15 hour period is attributable to the diabatic PV production associated with these MCSs.

Two days later the AEW is approaching the West African coast as can be seen in perturbation PV in Figure 5.6e. At this time, the main perturbation PV associated with the AEW is at approximately 9°W with an MCS to the west and a large low-reflectivity region in and around the trough. Further the main PV is connected to another maximum in perturbation PV just off the coast making the overall AEW trough elongated in the longitudinal direction. This second maximum in PV is also co-located with an expansive region of reflectivity ahead of the trough associated with a decaying MCS. The vertical cross-section in Figure 5.6f indicates that PV is being generated by diabatic processes between 600 and 500 hPa throughout this region. High cloud fractions reveal that this is clearly associated with expansive upper-level cloud indicative of broad trailing stratiform cloud regions. At this time there is also diabatic PV generation at low-levels off the coast, likely due to the larger fractions of deep convection.

Another two days later (Figures 5.6g and 5.6h) the main PV has propagated northwest and is just off the West African coast while the secondary maximum remains to the south. Thus the elongated AEW trough has rotated into a more south-north orientation again. Now over the ocean, the strongest reflectivity is situated along the trough axis rather than ahead. Figure 5.6h shows a cross-section through the main northernmost perturbation PV anomaly at this time. Although there is not as extensive of a stratiform cloud region as at previous times, there is still notable diabatic generation of PV between 800-500 hPa in association with large cloud fractions above 600 hPa.

In Figure 5.7 we present similar snapshots of the 2010-CTRL simulation. At 00 UTC on

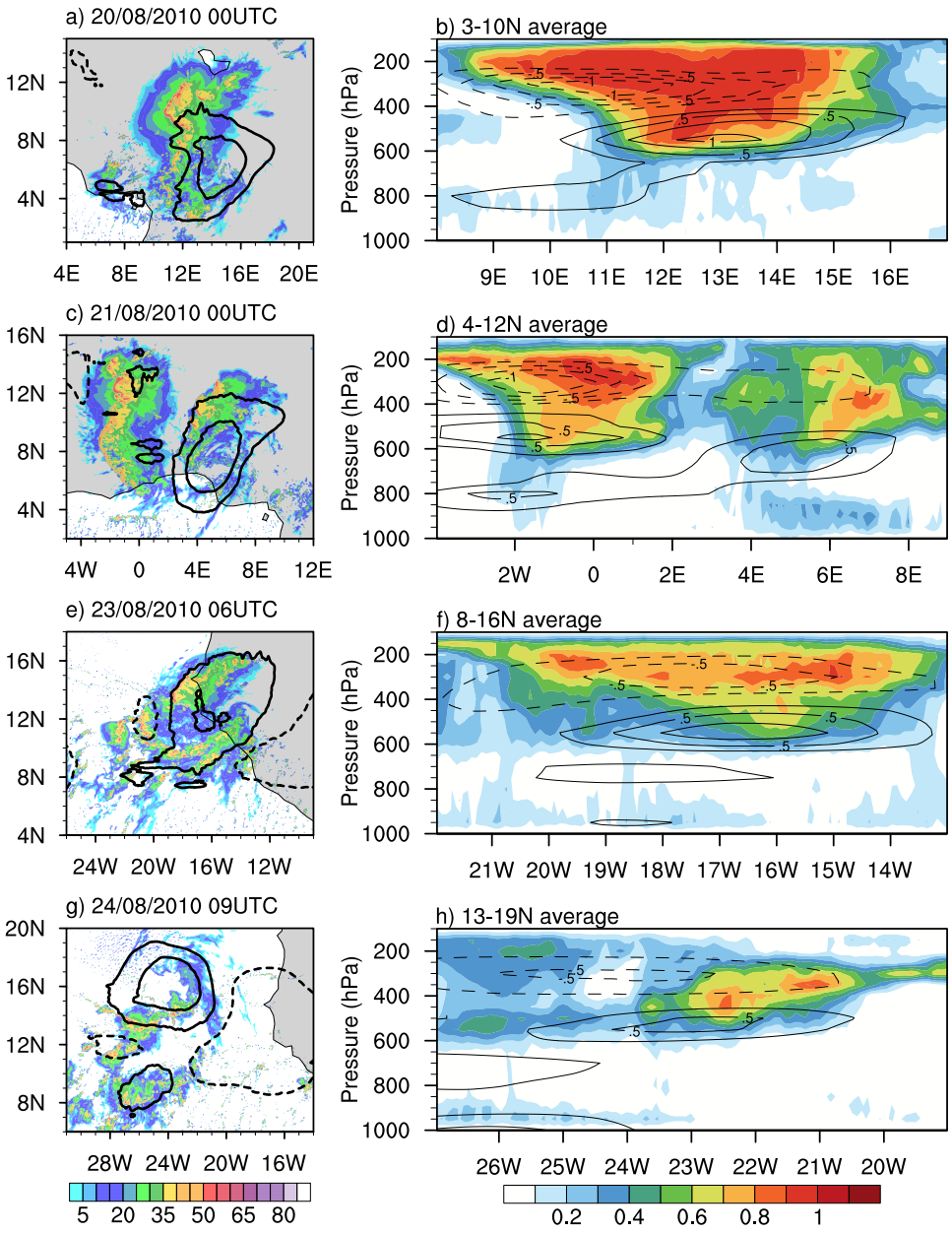

Figure 5.7: As in Figure 5.6 but for the 2010-CTRL simulation.

the 20th August the perturbation PV anomaly representing the AEW trough is centered at 15°N. At this time there is a single large MCS with deep convection along 12°E just ahead of the trough with an extensive stratiform cloud region trailing into the trough. Cross-sections (Figure 5.7b) show a deep column of cloud fraction between 10°E and 12°E indicating the edge of the leading convective line and large cloud fractions above 600 hPa indicating trailing stratiform cloud. The diabatic PV generation associated with this trailing stratiform cloud region is greater than 1 PVU/day in places and extends between 11°E and 16°E; the same region as the perturbation PV anomaly. Thus it appears that the MCV associated with the MCS is reinforcing the circulation of the AEW. Further there is also some diabatic generation of PV by the deep convection at 800 hPa between 8°E and 12°E. Thus at this time there is clear growth of the PV in the mid-levels via stratiform heating processes. This is corroborated by Figure 5.3f.

One day later (Figure 5.7c), the large MCS has propagated out ahead of the AEW and another has formed in its wake. Although weaker this MCS also has an expansive trailing stratiform cloud region that is generating PV at around 600 hPa. Further, the large MCS that propagated ahead of the AEW is also generating both mid- and low-level PV. This is acting to propagate the overall AEW westward as is corroborated by Figure 5.4f.

Two days later once the AEW trough has propagated to the West African coast (Figure 5.7e) the AEW PV anomaly has two MCSs associated with it. Both have significant stratiform cloud regions and as such, the AEW trough is nearly entirely filled with a broad stratiform cloud region. The resulting diabatic PV generation (Figure 5.7f) instigates another period of growth (as can be seen in Figure 5.3f).

Finally, a day later the AEW trough is now entirely over ocean (Figure 5.7g). There are now two maxima in positive perturbation PV, with the main AEW trough centered at 16°N and a smaller perturbation PV anomaly to the south centered at 9°N. The main perturbation PV anomaly is associated with scattered convection. According to Figure 5.7h this is associated with enough upper-level stratiform cloud to be generating PV in and around the trough. Much like in the 2007-CTRL simulation, convection is enhanced along an elongated axis associated with the main AEW trough. The secondary PV maxima is co-located with an enhanced region of convection associated with the AEW trough axis and the ITCZ. This leads to two perturbation PV maxima along the AEW trough axis; one which is the main perturbation PV of the AEW while over land, and one that develops in association with enhanced convection due to the AEW and ITCZ.

5.2 AEWs Without Moist Convection

In the previous section, as well as in Chapter 4, we showed that moist convection plays a significant role in AEW dynamics. Specifically, Figures 5.2a and 5.2b showed that the largest contribution to growth of PV in the AEW, primarily in the low and mid levels, is moist diabatic processes. Given these results, we hypothesize that when moist convection is switched off in simulations of the same AEWs, AEW anomalies including wind and PV, will begin to decay. Further, our work in Chapter 4 showed that the mid and upper level PV anomalies propagate forward via advection by the background flow, while the low-levels propagate forward via diabatic processes. Thus we expect that without moist convection, the AEW PV anomaly will shear apart and the low-levels will become decoupled from the mid and upper levels. We now test these theories with the sensitivity studies described in section 2.1.3.

Figure 5.8 shows the vertical structure of the AEW in all the simulations averaged after the time at which moist convection is shut off. Both of the simulations initialized with half of the moisture (HLFM) and the simulations run with no microphysics heating (NOMH) simulations produce a similar peak in PV and winds between 500 and 400 hPa, with much weaker PV than the control (CTRL) simulation below these levels. Both HLFM simulations, which are the more moderate of the sensitivity studies with some precipitation still present (not shown), have a downshear tilted PV column extending to 800 hPa with some weak surface PV anomalies. The 2007-NOMH simulation has weak mid-level PV anomalies but these are sheared apart from the main 500–400-hPa PV anomaly. The 2010-NOMH simulation has no notable PV anomalies below 550 hPa.

These results make it clear that moist convective processes are fundamental for maintaining the below-500-hPa level PV anomaly. While there are very little in the way of low-level PV anomalies in any of the sensitivity studies, there are some low-level perturbation meridional winds. Assuming PV may be inverted, these winds are likely the projection of the main 500–400-hPa PV anomaly down to the surface.

With the exception of 2007-NOMH, there are perturbation PV anomalies aloft above 300 hPa in the sensitivity studies that do not manifest in the CTRL simulations. This is associated with slightly stronger winds at these levels. From Figure 5.5 it was apparent that diabatic processes associated with trailing stratiform clouds act to produce negative perturbation PV above the region of maximum latent heating. This process is also apparent from Figures 5.6 and 5.7. Thus it is expected that the upper-level PV associated with the AEWs in the sensitivity studies would typically be present if not for the destruction of

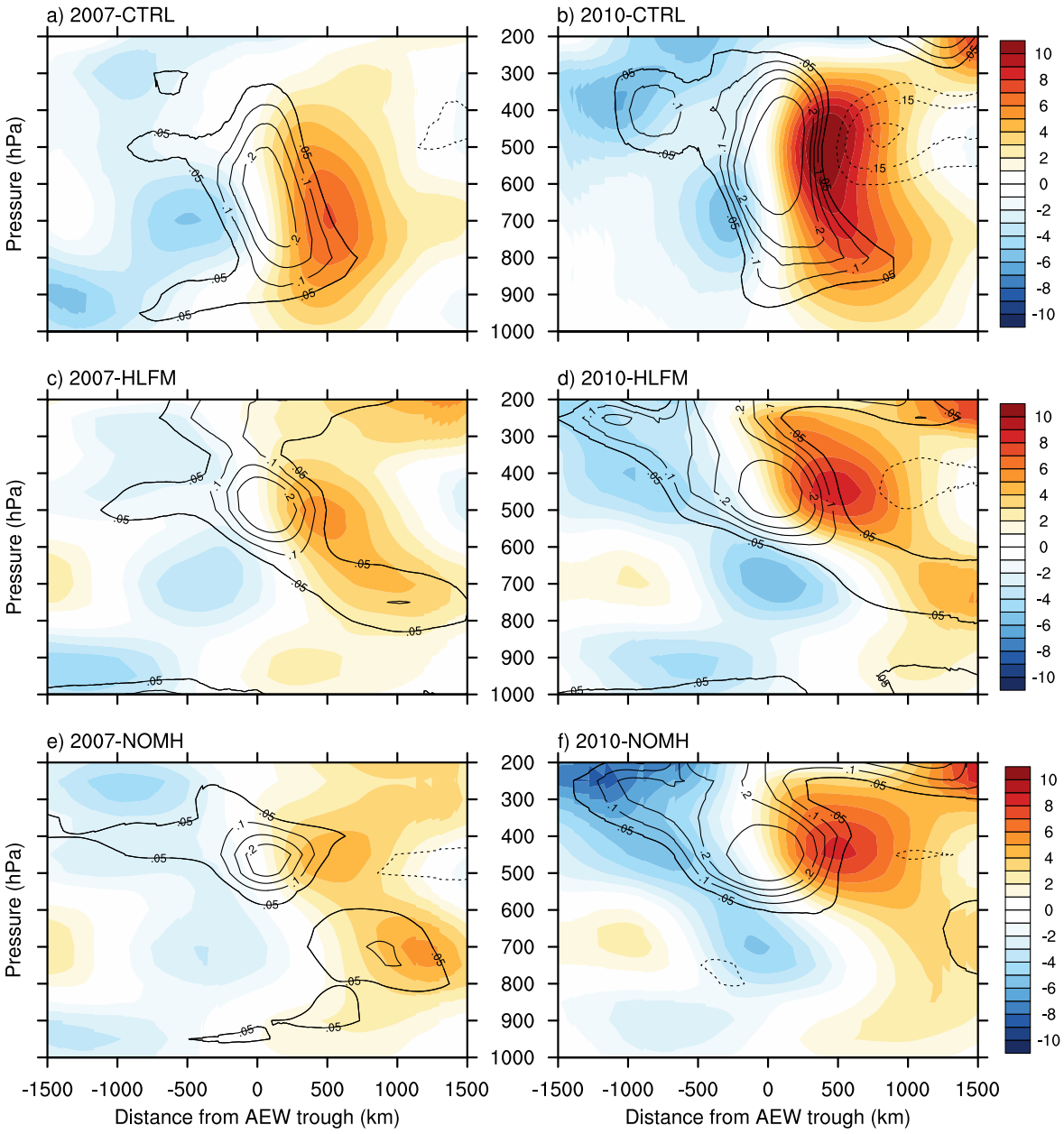

Figure 5.8: PV (contours; PVU) and meridional winds (shades; ms^{-1}) averaged 250 km north and south of the tracked AEW vorticity center, and then averaged over the simulation. Figures show different simulations; a) 2007-CTRL, b) 2010-CTRL, c) 2007-HLFM, d) 2010-HLFM, e) 2007-NOMH, and f) 2010-NOMH.

positive PV associated with diabatic processes. Therefore the action of moist convective processes is to decay the upper-levels of the AEW, and enhance the lower-levels of the AEW. Thus diabatic processes give rise to the deep column of PV and winds typically associated with AEWs.

Figure 5.9 shows the average 800–500-hPa PV and EKE in the AEW trough for all simulations. These levels represent the canonical core of the AEW that is not present in the sensitivity studies (Figure 5.8). In each sensitivity study (dashed for HLFM; dotted for NOMH), PV and EKE anomalies decrease after the moist convection is shut off. Meanwhile those variables in the CTRL simulations (solid) maintain themselves at a similar magnitude, albeit with significant variability. After one to two days this decay stops and the AEW maintains a much lower magnitude of perturbation PV or EKE. In the case of perturbation PV, this is close to zero, while in the case of EKE this is about half the original EKE before the moist convection was shut off. It is expected that the low-level EKE is not also zero because there is a projection of the still-present, upper-level PV anomaly onto the lower levels.

Notably toward the end of the sensitivity studies, EKE in the 2010 sensitivity studies (Figure 5.9d), is similar to that in the CTRL. Here EKE in the CTRL simulation also takes a significant drop, such that for around a day, the EKE in all simulations is approximately the same. This may be explained by the lack of moist convection close to the AEW trough at this time in the CTRL simulation. In Figure 2.2d the precipitation has moved ahead of the trough and the AEW trough is no longer associated with significant moist convection. Thus the similarity between the CTRL simulation and sensitivity studies may be because there was no moist convection in the CTRL simulation and the AEW was naturally decaying without the presence of moist convection. This highlights the fact that moist convection and its position relative to the trough is important for maintaining the low and mid level perturbations representative of the AEW.

Figure 5.10 shows time series of 500–300-hPa PV and EKE; the levels at which the PV anomaly is still present. In each sensitivity study there is an initial increase after moist convection is shut off, in response to the initial unphysical adjustment to the environment (HLFM) and physics (NOMH). After this, PV and EKE anomalies decrease at a steady rate. Thus, despite an AEW PV anomaly still being present as is clear from Figure 5.8, the PV at all levels is decaying. An examination of propagation statistics (not shown; similar to Figure 5.4) reveals that there is little difference in the mechanisms propagating them. Non-linear ($-V' \cdot \nabla P'$) and Rossby wave-like ($-V' \cdot \nabla \bar{P}$) mechanisms still contribute to propagation but the dominant mechanism is advection by the background flow ($-\bar{V} \cdot \nabla P'$). Thus the remaining 500–300-hPa PV anomalies are little more than a remnant of the AEW left over

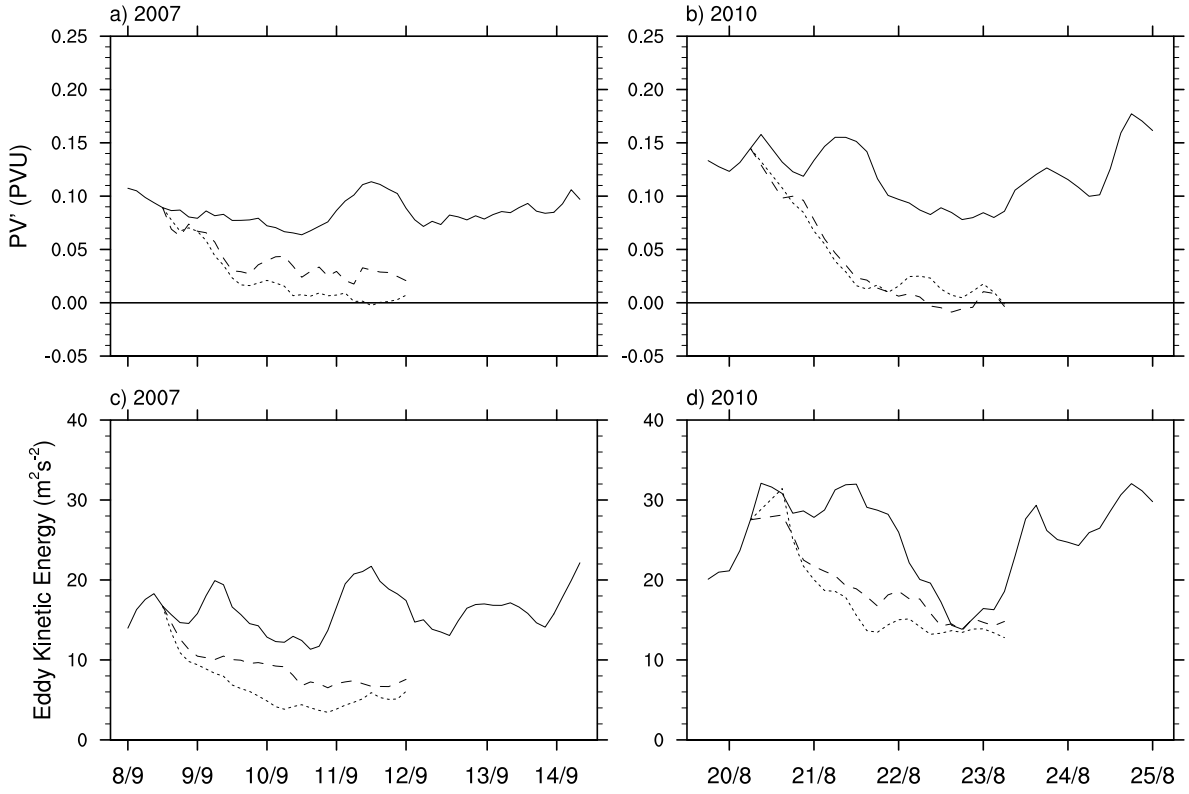

Figure 5.9: Time series of a,b) perturbation PV and c,d) EKE following the tracked a,c) 2007 and b,d) 2010 AEW troughs. Variables are averaged between 800-400 hPa and over a 1000km by 1000km area with the trough at it's center. Solid lines are for the CTRL simulations, dashed lines are for the HLFM simulations, and dotted lines are for the NOMH simulations.

from the PV anomaly in the initial conditions, that is being advected passively by the background flow.

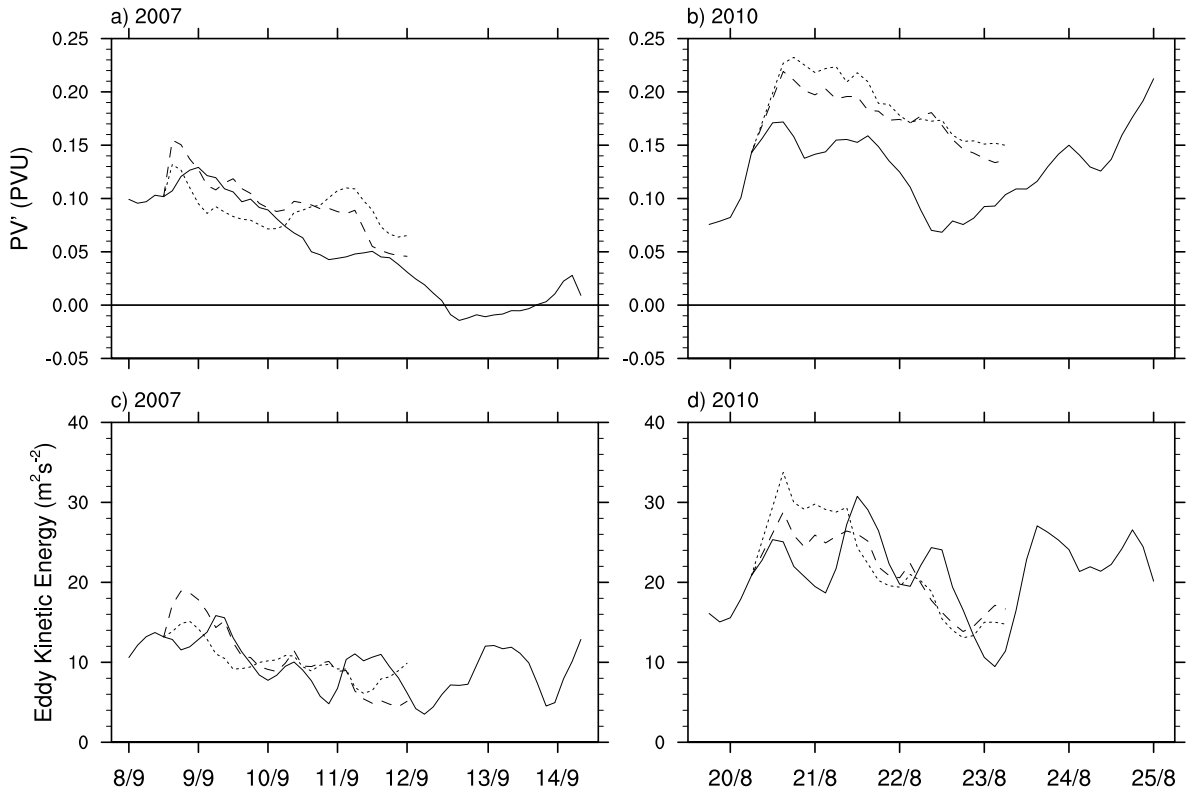

Figure 5.10: As in Figure 5.9 but for 500-300 hPa.

To understand why the AEW is decaying in the sensitivity studies, we examine growth mechanisms from the PV perspective. In the absence of moist convection, the only remaining processes that are of notable magnitude are the cross-advections ($-V' \cdot \nabla \bar{P}$) and frictional processes. Figure 5.11 compares these two processes averaged over 800–300-hPa across all simulations.

In the case of the CTRL simulations, although cross-advections contribute a fractional growth of 0.06-0.09 day^{-1} the decay by frictional processes is only 0.03–0.04 day^{-1}. Thus, although small, cross-advections contribute to growth. In the sensitivity studies, these cross-advections are smaller, contributing only 0.04–0.06 fractional growth per day. Thus in the absence of moist convection, these processes are smaller, possibly due to the absence of the contribution by moist waves. The fractional contributions to decay by frictional

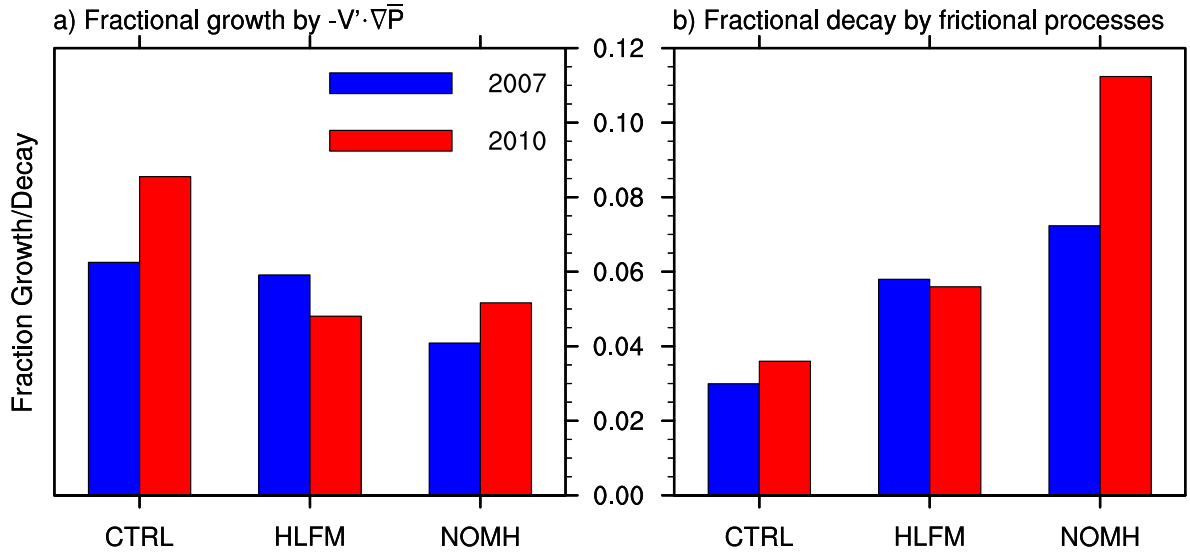

Figure 5.11: Average fractional contribution to growth/decay of 800–300-hPa perturbation PV following AEW (units of per day).

processes though are larger in the sensitivity studies and are enough to offset the effect of cross-advections. Thus in the absence of moist convection, the AEWs in the sensitivity studies decay at all levels as seen in Figures 5.9 and 5.10. This provides further evidence that without moist convection, AEWs cannot maintain themselves.

5.3 The Maintenance of AEWs by Moist Convection

Results in the previous sections and in Chapter 4 highlight the role that moist convection plays in the dynamics of AEWs. Here we compile the key findings of this Chapter, into a single conceptual framework describing the maintenance of AEWs. Figure 5.12 depicts a three-dimensional diagram of an idealized AEW with moist convection present.

The peak in perturbation PV is depicted on the 600-hPa surface with positive perturbation PV (red) representing the trough and negative perturbation PV (blue) representing the ridges. Deep moist convection initiates in the northerlies to the west of the trough. The resulting condensational heating from deep convection is associated with positive PV generation in the low-levels ahead of the trough. The action of the low-level diabatic PV generation is to counteract the role of low-level shear in disconnecting the peak mid-level PV from the low-level PV. Thus PV from deep moist convection maintains the typical column of PV associated with AEWs.

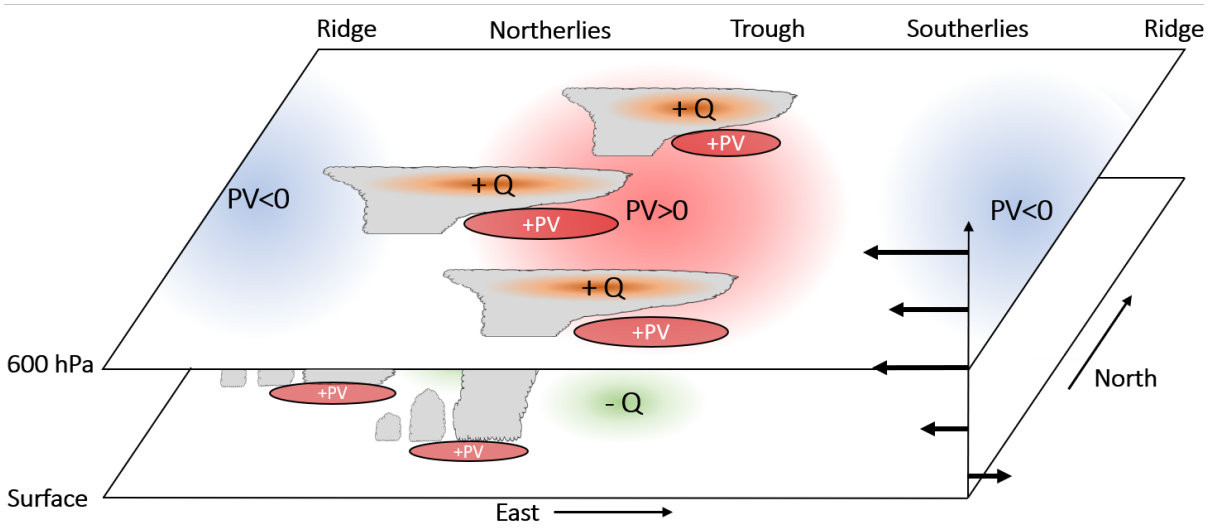

Figure 5.12: Three-dimensional conceptual diagram of the moist convective dynamics affecting AEWs. Diagram depicts 2 planes, one at the surface and one at the peak level for AEWs. Red and blue shades depict AEW perturbation PV. Orange and green shades indicate condensational heating and evaporative cooling respectively associated with the trailing stratiform cloud regions behind MCSs depicted as grey clouds. Generation of positive PV by diabatic processes is depicted by red circles with black outlines. Arrows represent the background zonal wind profile.

Once deep moist convection matures, large trailing stratiform cloud regions occupy much of the upper-levels in the region of the trough. The gradient in diabatic heating between upper-level condensational heating and low-level evaporative cooling is maximized in the mid-levels. This heating generates MCVs associated with the MCSs through the generation of positive PV. This positive PV generation coincides with the peak perturbation PV in the AEW, enhancing and maintaining the mid-level AEW circulation. These trailing stratiform cloud regions may be from one large MCS (i.e. Figures 5.7a and 5.7b) or from multiple smaller MCSs (i.e. Figures 5.6c, 5.6d, 5.7c, and 5.7d). Nonetheless, the addition of PV from one large MCS or multiple small MCSs is on the scale of the AEW PV anomaly and can therefore maintain the AEW.

As MCSs mature they often gain a ground-relative speed faster than the AEW (e.g. Figure 5.7c and Laing et al. 2008). Over the course of each MCSs life time, the MCSs trailing stratiform cloud can coincide with the AEW trough, which serves to enhance the AEW. As the MCS outpaces the propagation of the AEW, the generation of PV by the MCS serves to propagate the AEW westward. Thus, it is a combination of multiple MCSs that propagate and maintain the mid-level AEW.

When it comes to growth of the AEW, we have shown both here and in Chapter 4 that barotropic and baroclinic instabilities, which can include forms of moist instability, are often smaller than diabatic processes not associated with an instability. Rather, the AEW growth mechanism as described in this study better resembles that of stratiform instability Mapes (2000). Stratiform instability was developed for equatorial waves with little rotation, but is easily extendable to non-equatorial, rotating mid-level waves, such as AEWs, through the application of PV. In this instability, stratiform cloud regions associated with deep moist convection enhance the temperature anomalies via condensational heating and evaporative cooling. Here, PV is generated in the mid-levels by these same processes.

The role of multiple MCSs in the dynamics of the AEW presents an explanation as to how the MCSs with a spatial scale of 100 km, project on to the AEW with a spatial scale of 1000 km. This process is similar to the stretched building block theory presented by Mapes et al. (2006). We propose that the organization of moist convection by the AEW resembles stretched building blocks.

The 'building blocks' theory posits that an average or filter over multiple MCSs produces a progression of clouds with an MCS-like structure on the scale of the AEW (Mapes et al. 2006, Figure 11). This MCS-like structure is the progression from shallow convection, to deep convection, to trailing stratiform regions. Evidence for this progression in AEWs is shown in Figure 5.5 where we demonstrated that the perturbation cloud and heating structures

smoothed onto the AEW-scale progress from deep moist convection in the northerlies, to trailing stratiform cloud in the trough. As we see in Figures 3.1, 5.6, and 5.7, at any given time there are typically multiple MCSs present in the wave; these comprise the individual building blocks. The cloud structures here are corroborated by Janiga and Thorncroft (2016) who showed that there are higher fractions of shallow convection, deep convection, and stratiform cloud in the ridge, northerlies, and trough respectively.

The stretched building block theory posits that the duration or spatial width of individual cloud regimes (shallow, deep, and stratiform) is extended by the conditions in the overlying wave. Such structure is again clear from Figure 5.5 where the deep moist convective and stratiform cloud regimes are combined spread over a region of nearly 1500 km while most of the individual MCSs shown in Figures 3.1, 5.6, and 5.7 are only 3-4° in longitude (approximately 300–400 km). Further, in Chapter 3 we showed that the duration of MCSs in the northerlies and trough is typically longer than an observed average. This is supported by Laing et al. (2012) who stated that long-lived precipitation episodes which survived beyond a single diurnal cycle occurred only every 2-3 days; this implies an influence of synoptic scale patterns on MCS longevity. Finally in Chapter 3 we also showed that there are viable mechanisms, caused by the AEW (increased CAPE and low-level shear), that likely lead to longer-lived MCSs.

Thus the evidence supports a stretched building block theory for cloud structures in the AEW similar to that presented in Mapes et al. (2006) Figure 11. This theory explains how the MCSs and their associated MCVs on the order of 100 kms project onto the larger synoptic scale of the AEW.

5.4 Summary

In this chapter, we aimed to answer questions 2 and 3 in Section 1.7.2. The first question addressed how the structure of moist convection can generate PV coincident with the mid-level AEW trough. To answer this we examined MCSs, their structure, and their PV generation within two AEWs in convection-permitting simulations. The second question asked what happened to the AEW when moist convection is not present. A set of sensitivity studies based on these simulations was used to elucidate the differences between AEWs with and without moist convection present.

In the previous Chapter we showed that interactions between the various components of the AEW can account for around half of the growth in the mid-levels as the AEW moves

across Africa. At the same time, we showed that diabatic processes likely account for the rest of the growth. Propagation and growth mechanisms in the simulated AEWs are similar to those in the composite AEWs in Chapter 4 but with some differences. Diabatic processes and nonlinear processes also contribute to propagation in the mid-levels. Nonetheless, the overwhelmingly dominant process is still the advection by the background flow. In this Chapter, we build on those findings by showing exactly how the diabatic processes contribute to mid-level growth. The role of moist convection in the growth of AEWs can be summarized as follows.

Deep moist convection that typically forms in the northerlies of the AEW, and is associated with the leading line of MCSs, generates low-level PV ahead of the AEW trough. This maintains the AEW PV column against the affects of background shear. Without this, the AEW PV anomaly is limited to levels above-500-hPa as the below-500-hPa PV is sheared away and rapidly decays. This has implications for TC genesis once the AEW reaches the Atlantic.

Generation of PV by upper-level stratiform cloud regions is the dominant process governing growth and maintenance of the mid-level AEWs. This process involves trailing stratiform heating the upper-levels and cooling the lower-levels. This leads to the generation of positive PV (and MCVs) in the mid-levels. These stratiform cloud regions trail back into the trough behind the aforementioned MCSs, thus growing the positive PV of the AEW trough. This occurs through the action of multiple MCSs and their associated MCVs over the course of the AEWs lifetime. As each MCS matures they typically propagate faster than the AEW, and their stratiform cloud regions transition from generating PV in the trough of the AEW, to generating PV ahead of the AEW. Thus, the AEW grows and propagates in bursts dependent on the phasing of moist convective trailing stratiform cloud regions with the AEW trough.

We present the theory that this diabatic growth mechanism is similar to that of stratiform instability as presented by Mapes (2000) and Kuang (2008). While this theory has typically been presented for non-rotational waves, the PV-framework presented here provides an explanation for the development of rotation due to stratiform-like heating profiles. To remedy the scale-separation issue we argue that the MCSs project onto the AEW in a manner akin to Mapes et al. (2006) stretched building block theory.

CHAPTER

6

CONCLUSIONS

In this study, we have examined the interaction between AEWs and moist convection. This problem is approached from two directions; with composite average AEWs in two different reanalyses and with high resolution WRF simulations of individual case studies. This approach has allowed us to examine the broad synoptic-scale features of the AEW while also examining mesoscale characteristics of moist convection. Reconciling the processes spanning these two scales has been a key goal of this study. A novel aspect is the PV approach to analyzing AEWs. PV is a useful measure with which to understand the dynamics of AEWs for many reasons; it combines thermodynamic and kinematic quantities into one variable, it represents the balanced flow, and its sources can be directly attributed to diabatic processes. While PV has been used before, it has not been thoroughly examined in the manner we present here. We now summarize the novel results of this study.

6.1 Summary of Results

6.1.1 The Influence of AEWs on Moist Convection

In Chapter 3 we aimed to answer the research questions in Section 1.7.1. Our first question was "What are the characteristics of moist convection within the AEW envelope and how do they relate to the AEW?". We showed that moist convection in the AEW typically occurs in the form of QLCSs over land and disorganized regions of deep moist convection over the ocean. QLCSs, exhibit distinct behavior that is independent of the AEW, moving faster than the AEW on average. This indicates that coupling of moist convection to the AEW is nonlinear, especially over land. Regions of deep moist convection are often associated with the AEW trough and therefore have a more linear coupling.

The second question was "Are the thermodynamics and moisture a result of the AEW or a biproduct of the convection?". There are five key factors that the AEW influences which will vary the initiation of moist convection and the strength and duration of the resulting MCSs; moisture, vertical motion, CAPE, CIN, and shear. We show that the MSE distribution is primarily governed by the AEW-scale horizontal advection. This indicates that the CAPE, CIN, and moisture distributions are a product of the AEW.

The third question in this section was "Which factors, influenced by the AEW, are important in initiating and maintaining moist convection?". CI varies with the AEW in space (CI typically occurs in the northerlies or trough) but not in time (the diurnal cycle controls timing). While variations in moisture, ascent, and CIN influence CI, it is surface warming associated with the diurnal cycle, orography, and surface boundaries that are the primary drivers of CI. Suppressing factors such as dry air and descent in the southerlies inhibit CI. A theory is presented that the superposition of the AEW cycle with the diurnal cycle is important for the variability of CI over West Africa. In the northerlies, higher shear in the average direction of motion of QLCSs better balances the cold pool circulation and will lead to more upright updrafts. This is explained by invoking RKW theory. Combined with enhanced CAPE, this leads to more intense and longer-lived MCSs in the northerlies.

These findings lead to the idea that the northerlies represent a a region where there is a superposition of moist convective ingredients. By this we mean that in the northerlies, multiple factors come together to enhance moist convection through different mechanisms; CI is enhanced by moisture convergence, ascent, and CIN, and MCSs are maintained for longer by increased CAPE and low-level shear.

6.1.2 The Influence of Moist Convection on the AEW

In Chapters 4 and 5 we aimed to answer the questions in Section 1.7.2, as well as the first question in Section 1.7.3. The first question was "What is the structure of diabatic PV tendencies relative to the AEW? And how do they compare to adiabatic PV tendencies?". AEW-scale diabatic heating transitions from stratiform cloud over East Africa to deep convection over the Atlantic. This leads to diabatic PV tendencies that transition from the mid-levels over East Africa to the low-levels over the Atlantic. We find that AEW dynamics can, to first order, be represented by the following equation:

$$\frac{\partial P_w}{\partial t} \approx -\underbrace{\bar{V}\cdot\nabla P_w}_{\text{A}} - \underbrace{V_w\cdot\nabla\bar{P}}_{\text{B}} - \underbrace{\bar{\eta}\frac{\partial Q_w}{\partial p}}_{\text{C}} - \underbrace{\zeta_w\frac{\partial\bar{Q}}{\partial p}}_{\text{D}} \tag{6.1}$$

Here the AEW-scale PV tendency is approximated by four terms; advection of the AEW PV by the background flow (source A), AEW-scale advection of the background PV (source B), vertical gradients in AEW-scale diabatic heating (source C), which is akin to an effective PV gradient (e.g. Cohen and Boos 2016), and a stretching of the AEW-scale vorticity by the background heating (source D).

The propagation of mid-level waves is dominated by advection via the background flow. The beta-effect also plays a role in the advection of individual waves on the aforementioned background PV gradients (Figure 4.10). Diabatic processes and non-linear advective processes can also influence the background-relative propagation by advecting or generating PV to the west of the AEWs PV anomaly. When diabatic processes are involved, this manifests in PV 'jumps' when MCSs generate PV in the northerlies. In contrast, in the lower-levels of the southern track PV column, the propagation is entirely driven by AEW-scale diabatic processes. These findings lead to the theory that the southern track can be separated into a mid-level dry wave and a low-level moist wave.

The growth of the AEW is characterized by AEW-scale advection of the time-mean PV, the vertical gradient in AEW-scale diabatic heating, and a stretching of the AEW-scale vorticity by the background diabatic heating. In Chapter 4 we reviewed the structure of anomalous and background PV. Over Africa and the Eastern Atlantic, the conditions are conducive for interactions between waves on various PV gradients that can grow via barotropic or baroclinic interactions. The reversal of background PV coincident with the AEJ is central to these interactions. Interactions between the dry waves on the various PV gradients and the low-level moist wave are summarized in Table 4.2. These include interactions between

the mid-level dry waves in the horizontal, between the mid-level dry wave on the negative PV gradient and the surface dry wave in the northern track, and between the low-level moist wave and mid-level dry waves in the southern track. Although the low-level moist wave grows and propagates entirely through AEW-scale diabatic processes, the mid-level dry waves cannot attain the magnitude of PV observed simply through these interactions. Rather, mid-level AEW-scale diabatic processes and the stretching of vorticity by time-mean heating contribute strongly in the mid-levels.

The second question was "How does the structure of convection lead to mid-level rotation on the scale of the AEW?". In Chapter 5 we examine the structure of moist convection relative to the AEW. Multiple MCSs result in broad regions of trailing upper-level stratiform cloud that are coincident with the trough and of a similar spatial coverage as the AEWs positive PV anomaly. The gradient between upper-level condensational heating and lower-level evaporative cooling result in mid-level PV growth that leads to MCVs.

The third question was "Does an AEW exist without convection present? And if so, what is the difference in AEW structure and why?". Propagation statistics in Section 4.5.1 and sensitivity studies in Section 5.2 highlight the fact that moist convective processes are essential for the maintenance of a deep PV column in the AEW. Without diabatic processes, the background flow shears the AEW PV column and the AEW PV anomaly is limited to levels above 500 hPa. The remaining PV anomaly in the sensitivity studies is simply a remnant of the PV anomaly previously present in the initial conditions, having been advected by the background flow and beta-effect. An analysis of growth processes suggests that the AEW is decaying without the presence of diabatic processes.

The final question addressed in this section is "What aspects of the DRW mechanism and/or stratiform instability are present in AEWs?". We argue that the system of PV anomalies in the southern track, where diabatic processes are prevalent, does not represent a DRW. First, baroclinicity in this region is insufficient for isentropic lift to drive moist convection alone; a central feature of the DRW. Second, the growth mechanism for DRWs described by Cohen and Boos (2016) does not occur in AEWs. However, the mid-level growth of PV by diabatic processes associated with trailing stratiform cloud regions strongly resembles stratiform instability (Mapes 2000; Kuang 2008). Although stratiform instability has typically been invoked for non-rotational waves (e.g., Kelvin Waves), PV represents a means through which to interpret it for a rotational wave. Further, the enhancement of MCSs in the northerlies via larger CAPE and more favorable shear, resembles Mapes et al. (2006) stretched building blocks theory. In this theory the MCSs constitute building blocks that, when filtered onto the AEW-scale, produce mostly deep convection in the northerlies and

stratiform cloud in the trough. The duration of deep moist convection and trailing stratiform clouds are modulated by the synoptic scale conditions to produce a life-cycle of cloud regimes over the AEW wavelength that resembles the life-cycle of an MCS.

6.2 Overarching Conclusions

6.2.1 A Conceptual Model for the AEW-Convection Interaction

The final research question was "Can we combine aspects of these processes into a model for the AEW-convection interaction?". Figure 6.1 shows cross-sections through an idealized AEW depicting a conceptual model for the AEW.

Other studies have argued for a single factor associated with the AEW, governing the AEW-relative distribution of moist convection; Tomassini et al. (2017) argued this is moisture convergence while Kiladis et al. (2006) argued this is adiabatic ascent. Here we argue that the coupling of moist convection with the AEW is more complex. In the northerlies (associated with the dry mid-level PV anomaly of the AEW trough in Figure 6.1), CI occurs because of the superposition of the diurnal cycle and lifting mechanisms such as outflow boundaries, the edge of the SAL, and terrain, with the AEWs moistening, ascent, and a reduction in CIN. This likely generates multiple MCSs that are more intense and longer-lived than usual due to enhanced CAPE and a more favorable interaction between MCS cold pools and the low-level shear. It is emphasized that the cloud shown in Figure 6.1 does not represent a single MCS on the scale of the AEW. Rather, it represents the dominant cloud regimes present in different phases of the AEW as a result of the projection of multiple MCSs onto the AEW-scale. This resembles the stretched building block theory of Mapes et al. (2006).

The projection of these MCSs on the AEW manifests in two ways. The northerlies are dominated by deep moist convection which generates positive PV in the low-levels. The trough is dominated by broad regions of trailing upper-level stratiform cloud that generate moist PV in the mid-levels. This mid-level moist PV superposes with the mid-level dry PV. This is the dominant process enhancing the mid-level PV and thus the main AEW circulation.

In Figure 6.1 we present the AEW as a system of interconnected moist and dry waves. Barotropic instability due to interactions between dry waves on the opposing mid-level PV gradients will enhance the mid-level waves. The interaction between the northern track surface dry wave and the mid-level dry wave on the negative PV gradient enhances the system through dry baroclinic instability. Finally, an interaction between the low-level moist

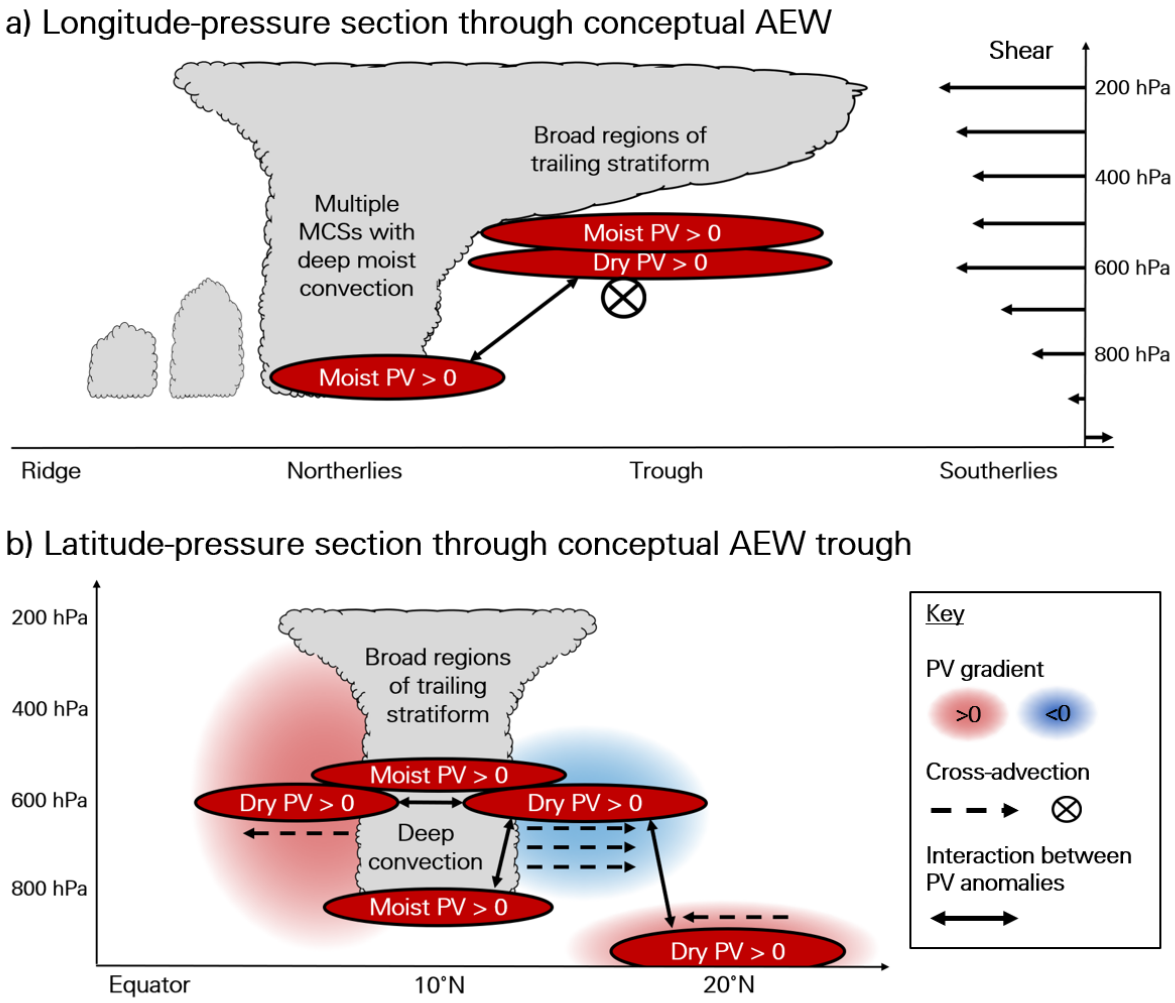

Figure 6.1: Conceptual cross-sections through a typical AEW from the PV perspective. Grey areas represent predominant regions of cloud. Red circles outlined in black represent typical regions of dry and moist PV anomalies. Shaded areas show meridional gradients in background PV. Two-ended solid arrows indicate an interaction between two PV anomalies. Dashed arrows and the circle with a cross represent the cross-advections enhancing dry PV anomalies. a) shows a longitude-height cross-section through a typical AEW at 10°N. The background wind profile is shown by the arrows on the right. b) shows a latitude-height cross-section through a typical AEW trough.

PV (generated by deep moist convection) and mid-level dry PV, may further enhance the AEW. These instabilities will account for a portion of the growth but, without the generation of mid-level PV by stratiform heating processes, the AEW would not be unstable.

Many of these conclusions are similar to others presented before. In particular, Mass (1979) based a number of similar conclusions on an analysis of a 10-layer linear model. This model parameterized the location of precipitation using mass and moisture convergence. The resultant latent heating was parameterized by a vertical profile with two peaks; one in the low-levels (which we now know represents deep convection) and one in the mid-levels (most likely a result of stratiform cloud). First, Mass (1979) found that the propagation of the AEW is affected little by the inclusion of latent heating and convective momentum adjustment. This is consistent with the results in Chapters 4 and 5 which show that the dominant process governing propagation is the advection by the background flow. Second, Mass (1979) found that the depth and vertical structure are heavily modulated by convective processes. This is also consistent with the results in Chapters 4 and 5, in particular those in Section 5.2. There, we showed that without deep moist convective processes, the AEW PV anomaly is limited to the mid–upper-levels. Further, Shapiro (1978) shows that vortex stretching by parameterized convective processes is important to obtain the correct magnitude of AEW perturbations. In Chapter 4 we showed that a dominant term in the PV budget of the AEW is the stretching of vorticity by background diabatic heating. Finally, Mass (1979) argued that the AEW is driven by dry instabilities before being modified by moist convection. In this section we have presented a similar conceptual model whereby the dry wave is enhanced and varied by moist processes. The important addition by our work is that the mid-level AEW is enhanced by stratiform cloud regions while the AEW structure is deepened by deep moist convection.

6.2.2 Reconciling Mesoscale and Synoptic Scale Views

Throughout this dissertation, we have used 4km grid-spacing simulations and $\geq 0.5^\circ$ grid spacing reanalyses in conjunction with each other. Through this method, we have assessed the processes occurring at both mesoscales and synoptic scales. In Chapter 3 we utilized this to our advantage. The mesoscale processes involved in CI were analyzed and compared back to the large scale features of AEWs represented by the composite averages. This allowed us to diagnose where and when synoptic scale features likely supported the mesoscale processes of CI. Further, in both Chapters 3 and 5 we were able to diagnose mesoscale features of the MCSs to help in diagnosing the stretched building block paradigm and the

role of this in growing the mid-level PV.

While results on both scales generally corroborate each other, there are some discrepancies between the two. Specifically, results in Chapter 4 suggest that diabatic processes are less dominant in mid-level AEW dynamics over West Africa than they are in Chapter 5. In Figure 4.8e there were two diabatic PV tendency maxima in phase with each other; one in the low-levels likely representing generation by deep moist convection and one in the mid-levels likely representing generation by stratiform. However, in Figure 5.5 we show that the deep convective and stratiform generation of PV are offset from one another; deep convective generation is in the northerlies while stratiform generation is in the trough. The former result in Chapter 4 relies on parameterization schemes to accurately represent the vertical heating. Clearly we see that the offset between these two is not represented by the parameterization scheme. Thus the results in Chapter 4 may underestimate the role of diabatic processes in the mid-levels. Nonetheless, they both corroborate that AEWs are dominated by diabatic processes and that instabilities cannot account for the total growth. This difference has clear implications for the use of reanalyses to represent diabatic processes. We will discuss this further in the next sections.

In the simulations, it is hard to make out the low-level moist wave associated with deep moist convection, despite there being notable generation of PV in the low-level northerlies (Figure 5.5). This PV anomaly is typically weak (as shown in the composite average AEWs; e.g. Figure 4.3). In this case we find that the diurnal processes in the simulations shroud the presence of the moist low-level PV. To clarify, through the use of a composite average and an AEW-scale budget in Chapter 4, diurnal signals are filtered out. However, in the simulations we do not have the means to avoid contamination by the diurnal cycle in our analysis. Thus any low-level anomalies are difficult to diagnose there. Nonetheless we see the same generation of low-level PV by deep moist convective processes in Chapter 5 that we do in Chapter 4, and on closer examination the moist PV anomaly is present in the simulations.

These results highlight the benefit of combining mesoscale and synoptic scale analyses where scale-interactions are key to the dynamics. Limitations in one or the other method may misrepresent or disguise features. Future work should use this two-pronged approach in diagnosing the dynamics in similar situations.

6.2.3 Forecasting Implications

There are significant implications of these findings for the modeling of AEWs and downstream systems such as tropical cyclones. In the previous section we highlighted the inability of modeling systems with non-convection-permitting resolution to accurately represent the phasing of stratiform heating with the AEW over West Africa. Most models providing forecasts for this region are global models that parameterize convection, often with similar schemes to those used in the reanalyses. An inability to capture the mid-level growth mechanism will lead to weaker waves overall due to the interconnectivity we have presented. Such forecast issues are corroborated by Elless and Torn (2018) who showed that an intensity bias in ECMWF forecasts was due to incorrectly represented convection. More generally Marsham et al. (2013) also highlighted the importance of resolving MCS structure in the West African Monsoon system.

Russell et al. (2017) showed that the low-levels of the southern track are most important for the generation of TCs from AEWs. In that study, we hypothesized that the correlation between low-level EKE and TC genesis numbers on a seasonal scale, may be connected to moist convective activity in the AEW. In this study, we have confirmed that the representation of moist convection is essential for the maintenance of a deep PV column, especially in the lower-levels. Thus, without accurate representation of the deep convection in the northerlies, TC genesis from AEWs is likely to be poorly represented. This highlights another situation where the representation of all components of the AEW system are essential for forecasts.

6.3 Future Work

In the previous section we discussed the issue of poorly represented moist convection for the forecasting of AEWs and subsequent Atlantic TC genesis. This highlights the need for improved representation of moist convection in models. Future work should address this issue through a number of means.

Improved parameterization of tropical convection and subsequent phasing with synoptic weather would help the community better forecast tropical systems. In Chapter 4 we highlighted how CI is significantly different from similar systems in the mid-latitudes (i.e. DRWs). Specifically, the availability of low-level moisture plays a much larger role over West Africa than in the mid-latitudes. Ma and Tan (2009) show that the inclusion of moisture controls on convective triggering in simulations of tropical cyclones is favorable for the

representation of moist convection. The inclusion of such modifications in cumulus parameterizations for forecast models may produce more favorable coupling between tropical synoptic scale systems and moist convection.

The implementation of a real-time mesoscale model over West Africa and the Atlantic would be advantageous for the forecasting of AEWs and subsequent tropical cyclones. Such a system would better represent the phasing between moist convection and AEWs. This would produce more accurate precipitation forecasts over West Africa, representation of AEWs, and TC genesis. Stored forecast data from this system would provide researchers a valuable dataset toward understanding West African weather and TC genesis.

In our discussions and conclusions, we have focused heavily on a model for the AEW while over land. We did however show that a number of processes change when the AEW reaches the coast. These include a switch from a mix of deep moist convection and stratiform cloud in the northerlies and trough, to mostly deep moist convection in the trough. The effect on the AEW is to build a deeper, less-tilted column of PV through more generation of low-level PV. This transition is central to the dynamics of the AEW over ocean. A more detailed examination of this transition and the structure and dynamics of AEWs over the ocean is required. This is also essential for the processes related to TC genesis.

In this study we have utilized reanalyses and high-resolution full-physics simulations to examine the interaction between AEWs and moist convection. These have provided a useful means to examine the dynamics of the interaction and develop a conceptual model governing the AEW-convection relationship. However, these theories need to be tested within a framework where we can isolate these mechanisms. Thus the most fundamental future work is a set of idealized modeling simulations where we test these theories and control for other variables.

In Section 6.1.2 we explained that the AEW may be approximated as in Equation 6.1. Future work will develop a simple two or three layer model based on this equation that can be used to represent the AEW. A simple convective parameterization can be developed which varies CI and the vertical distribution of diabatic heating with the phase of the AEW. If this simple model is able to accurately replicate the AEW, then we can confirm the model presented here. Eliminating source terms in the equation and varying the convective parameterization will highlight the role of various factors in the AEW.

To further examine the role of variable CAPE and shear in the AEW, on the longevity of MCSs, an idealized convective scale model such as George Bryan's CM1 (Bryan and Fritsch 2002) can be used. The simulations would be initialized using composite average soundings from West Africa. The wind profile could then be manipulated to represent the shear in

the northerlies and southerlies. Alternatively the temperature and moisture profiles could be manipulated to represent the differences in CAPE between northerlies and southerlies. MCSs in each simulation can be compared to examine whether the theories presented in Chapter 3 hold up.

Finally these theories need to be tested using observational data to understand whether the reanalyses and simulations are actually representing reality. Here we have done our best to make sure the simulations represent reality but these theories also need to be tested using observations that we know for a fact represent reality. To do this we might use the AMMA field campaign. During that campaign the ECMWF utilized their data assimilation system to produce a short reanalysis that incorporated all the AMMA field data. If we can prove our theories using case studies from the AMMA field campaign we may better be able to verify that the idea's here are representative of the actual dynamics of AEWs.

REFERENCES

Andersen, J. A. and Kuang, Z. (2012). Moist static energy budget of MJO-like disturbances in the atmosphere of a zonally symmetric aquaplanet. *J. Climate*, 25(8):2782–2804.

Arnold, N. P., Kuang, Z., and Tziperman, E. (2013). Enhanced MJO-like variability at high SST. *J. Climate*, 26(3):988–1001.

Avila, L. A. and Pasch, R. J. (1992). Atlantic tropical systems of 1991. *Mon. Wea. Rev.*, 120(11):2688–2696.

Avila, L. A., Pasch, R. J., and Jiing, J.-G. (2000). Atlantic tropical systems of 1996 and 1997: Years of contrast. *Mon. Wea. Rev.*, 128(10):3695–3706.

Berry, G. J. and Thorncroft, C. D. (2005). Case Study of an Intense African Easterly Wave. *Mon. Wea. Rev.*, 133:752–766.

Berry, G. J. and Thorncroft, C. D. (2012). African Easterly Wave Dynamics in a Mesoscale Numerical Model: The Upscale Role of Convection. *J. Atmos. Sci.*, 69:1267–1283.

Blake and Zelinsky (cited 2018). National Hurricane Center Tropical Cyclone Report: Hurricane Harvey. [Available online at https://www.nhc.noaa.gov/data/tcr/AL092017_Harvey.pdf].

Bryan, G. H. and Fritsch, J. M. (2002). A benchmark simulation for moist nonhydrostatic numerical models. *Mon. Wea. Rev.*, 130(12):2917–2928.

Bryan, G. H., Knievel, J. C., and Parker, M. D. (2006). A multimodel assessment of RKW theory's relevance to squall-line characteristics. *Mon. Wea. Rev.*, 134(10):2772–2792.

Bryan, G. H., Wyngaard, J. C., and Fritsch, J. M. (2003). Resolution requirements for the simulation of deep moist convection. *Mon. Wea. Rev.*, 131(10):2394–2416.

Burpee, R. W. (1972). The Origin and Structure of Easterly Waves in the Lower Troposphere of North Africa. *J. Atmos. Sci.*, 29:77–90.

Burpee, R. W. (1974). Characteristics of North African Easterly Waves During the Summers of 1968 and 1969. *J. Atmos. Sci.*, 31:1556–1570.

Cangialosi, Latto, and Berg (cited 2018). National Hurricane Center Tropical Cyclone Report: Hurricane Irma. [Available online at https://www.nhc.noaa.gov/data/tcr/AL112017_-Irma.pdf].

Carlson, T. N. (1969). Synoptic Histories of Three African Disturbances that Developed into Atlantic Hurricanes. *Mon. Wea. Rev.*, 97:256–276.

Chang, C.-B. (1993). Impact of desert environment on the genesis of African wave disturbances. *J. Atmos. Sci.*, 50(14):2137–2145.

Charney, J. G. and Stern, M. E. (1962). On the Stability of Internal Baroclinic Jets in a Rotating Atmosphere. *J. Atmos. Sci.*, 19:159–172.

Chen, T.-C. (2006). Characteristics of African easterly waves depicted by ECMWF reanalyses for 1991–2000. *Mon. Wea. Rev.*, 134(12):3539–3566.

Cifelli, R., Lang, T., Rutledge, S. A., Guy, N., Zipser, E. J., Zawislak, J., and Holzworth, R. (2010). Characteristics of an African easterly wave observed during NAMMA. *J. Atmos. Sci.*, 67(1):3–25.

Cohen, N. Y. and Boos, W. R. (2016). Perspectives on moist baroclinic instability: implications for the growth of monsoon depressions. *J. Atmos. Sci.*, 73(4):1767–1788.

Coniglio, M. C., Corfidi, S. F., and Kain, J. S. (2012). Views on applying RKW theory: An illustration using the 8 May 2009 derecho-producing convective system. *Mon. Wea. Rev.*, 140(3):1023–1043.

Crétat, J., Vizy, E. K., and Cook, K. H. (2015). The relationship between African easterly waves and daily rainfall over West Africa: observations and regional climate simulations. *Clim. Dynam.*, 44(1-2):385–404.

Davis, C. A. and Weisman, M. L. (1994). Balanced dynamics of mesoscale vortices produced in simulated convective systems. *J. Atmos. Sci.*, 51(14):2005–2030.

De Vries, H., Methven, J., Frame, T. H., and Hoskins, B. J. (2009). An interpretation of baroclinic initial value problems: Results for simple basic states with nonzero interior PV gradients. *J. Atmos. Sci.*, 66(4):864–882.

Dee, D. P., Uppala, S., Simmons, A., Berrisford, P., Poli, P., Kobayashi, S., Andrae, U., Balmaseda, M., Balsamo, G., Bauer, P., et al. (2011). The ERA-Interim reanalysis: Configuration and performance of the data assimilation system. *Quart. J. Roy. Meteor. Soc.*, 137(656):553–597.

Diedhiou, A., Janicot, S., Viltard, A., de Felice, P., and Laurent, H. (1999). Easterly wave regimes and associated convection over West Africa and tropical Atlantic: results from the NCEP/NCAR and ECMWF reanalyses. *Clim. Dynam.*, 15(11):795–822.

Duvel, J. P. (1990). Convection over tropical Africa and the Atlantic Ocean during northern summer. Part II: Modulation by easterly waves. *Mon. Wea. Rev.*, 118(9):1855–1868.

Eady, E. T. (1949). Long waves and cyclone waves. *Tellus*, 1(3):33–52.

Elless, T. J. and Torn, R. D. (2018). African easterly wave forecast verification and its relation to convective errors within the ecmwf ensemble prediction system. *Weather and Forecasting*, 33(2):461–477.

Fink, A. H. and Reiner, A. (2003). Spatiotemporal variability of the relation between African Easterly Waves and West African Squall Lines in 1998 and 1999. *J. Geophys. Res.*, 108:4332.

Fjørtoft, R. (1950). *Application of integral theorems in deriving criteria of stability for laminar flows and for the baroclinic circular vortex*. Grøndahl & søns boktr., I kommisjon hos Cammermeyers boghandel.

Fritsch, J., Murphy, J., and Kain, J. (1994). Warm core vortex amplification over land. *J. Atmos. Sci.*, 51(13):1780–1807.

Gu, G., Adler, R. F., Huffman, G. J., and Curtis, S. (2004). African easterly waves and their association with precipitation. *J. Geophys. Res.*, 109.

Hagos, S., Zhang, C., Tao, W.-K., Lang, S., Takayabu, Y. N., Shige, S., Katsumata, M., Olson, B., and L'Ecuyer, T. (2010). Estimates of tropical diabatic heating profiles: Commonalities and uncertainties. *J. Climate*, 23(3):542–558.

Hall, N. M., Kiladis, G. N., and Thorncroft, C. D. (2006). Three-dimensional structure and dynamics of African easterly waves. Part II: Dynamical modes. *J. Atmos. Sci.*, 63(9):2231–2245.

Hannah, W. M. and Aiyyer, A. (2017). Reduced african easterly wave activity with quadrupled co2 in the superparameterized cesm. *J. Climate*, 30(20):8253–8274.

Hayashi, Y. (1982). Space-time spectral analysis and its applications to atmospheric waves. *J. Meteor. Soc. Japan*, 60(1):156–171.

Hopsch, S. B., Thorncroft, C. D., and Tyle, K. R. (2010). Analysis of African Easterly Wave Structures and Their Role in Influencing Tropical Cyclogenesis. *Mon. Wea. Rev.*, 138:1399–1419.

Hoskins, B. J., McIntyre, M., and Robertson, A. W. (1985). On the use and significance of isentropic potential vorticity maps. *Quart. J. Roy. Meteor. Soc.*, 111(470):877–946.

Hsieh, J.-S. and Cook, K. (2005). Generation of African easterly wave disturbances: Relationship to the African easterly jet. *Mon. Wea. Rev.*, 133(5):1311–1327.

Hsieh, J.-S. and Cook, K. (2008). On the instability of the African easterly jet and the generation of African waves: Reversals of the potential vorticity gradient. *J. Atmos. Sci.*, 65(7):2130–2151.

Hsieh, J.-S. and Cook, K. H. (2007). A study of the energetics of African easterly waves using a regional climate model. *J. Atmos. Sci.*, 64(2):421–440.

Huffman, G. J., Bolvin, D. T., Nelkin, E. J., Wolff, D. B., Adler, R. F., Gu, G., Hong, Y., Bowman, K. P., and Stocker, E. F. (2007). The TRMM multisatellite precipitation analysis (TMPA): Quasi-global, multiyear, combined-sensor precipitation estimates at fine scales. *J. Hydrometeor.*, 8(1):38–55.

Janiga, M. A. and Thorncroft, C. D. (2013). Regional differences in the kinematic and thermodynamic structure of African easterly waves. *Quart. J. Roy. Meteor. Soc.*, 139(675):1598–1614.

Janiga, M. A. and Thorncroft, C. D. (2014). Convection over Tropical Africa and the East Atlantic during the West African Monsoon: Regional and Diurnal Variability. *J. Climate*, 27:4159–4188.

Janiga, M. A. and Thorncroft, C. D. (2016). The influence of African easterly waves on convection over tropical Africa and the East Atlantic. *Mon. Wea. Rev.*, 144(1):171–192.

Kiladis, G. N., Thorncroft, C. D., and Hall, N. M. (2006). Three-dimensional structure and dynamics of African easterly waves. Part I: Observations. *J. Atmos. Sci.*, 63(9):2212–2230.

Kuang, Z. (2008). A moisture-stratiform instability for convectively coupled waves. *J. Atmos. Sci.*, 65(3):834–854.

Kuo, H.-l. (1949). Dynamic instability of two-dimensional nondivergent flow in a barotropic atmosphere. *J. Meteor.*, 6(2):105–122.

Laing, A. G., Carbone, R., Levizzani, V., and Tuttle, J. (2008). The propagation and diurnal cycles of deep convection in northern tropical Africa. *Quart. J. Roy. Meteor. Soc.*, 134(630):93–110.

Laing, A. G., Carbone, R. E., and Levizzani, V. (2011). Cycles and propagation of deep convection over equatorial Africa. *Mon. Wea. Rev.*, 139(9):2832–2853.

Laing, A. G. and Fritsch, J. M. (1993). Mesoscale convective complexes in Africa. *Mon. Wea. Rev.*, 121(8):2254–2263.

Laing, A. G., Fritsch, J. M., and Negri, A. J. (1999). Contribution of mesoscale convective complexes to rainfall in Sahelian Africa: Estimates from geostationary infrared and passive microwave data. *J. Appl. Meteor.*, 38(7):957–964.

Laing, A. G., Trier, S. B., and Davis, C. A. (2012). Numerical simulation of episodes of organized convection in tropical northern Africa. *Mon. Wea. Rev.*, 140(9):2874–2886.

Landsea, C. W. (1993). A climatology of intense (or major) Atlantic hurricanes. *Mon. Wea. Rev.*, 121(6):1703–1713.

Ma, L.-M. and Tan, Z.-M. (2009). Improving the behavior of the cumulus parameterization for tropical cyclone prediction: Convection trigger. *Atmospheric Research*, 92(2):190–211.

Mapes, B., Tulich, S., Lin, J., and Zuidema, P. (2006). The mesoscale convection life cycle: Building block or prototype for large-scale tropical waves? *Dynamics of atmospheres and oceans*, 42(1-4):3–29.

Mapes, B. E. (2000). Convective inhibition, subgrid-scale triggering energy, and stratiform instability in a toy tropical wave model. *J. Atmos. Sci.*, 57(10):1515–1535.

Markowski, P. and Richardson, Y. (2011). *Mesoscale meteorology in midlatitudes*, volume 2. John Wiley & Sons.

Marsham, J. H., Dixon, N. S., Garcia-Carreras, L., Lister, G. M., Parker, D. J., Knippertz, P., and Birch, C. E. (2013). The role of moist convection in the west african monsoon system: Insights from continental-scale convection-permitting simulations. *Geophys. Res. Lett.*, 40(9):1843–1849.

Mass, C. (1979). A linear primitive equation model of african wave disturbances. *J. Atmos. Sci.*, 36(11):2075–2092.

Mathon, V., Laurent, H., and Lebel, T. (2002). Mesoscale convective system rainfall in the Sahel. *J. Appl. Meteor.*, 41(11):1081–1092.

McCrary, R. R., Randall, D. A., and Stan, C. (2014). Simulations of the West African Monsoon with a Superparameterized Climate Model. Part II: African Easterly Waves. *J. Climate*, 27(22):8323–8341.

Mekonnen, A., Thorncroft, C. D., and Aiyyer, A. R. (2006). Analysis of convection and its association with African easterly waves. *J. Climate*, 19(20):5405–5421.

Menard, R. D. and Fritsch, J. (1989). A mesoscale convective complex-generated inertially stable warm core vortex. *Mon. Wea. Rev.*, 117(6):1237–1261.

Molinari, J., Skubis, S., Vollaro, D., Alsheimer, F., and Willoughby, H. E. (1998). Potential vorticity analysis of tropical cyclone intensification. *J. Atmos. Sci.*, 55(16):2632–2644.

Molinari, J., Vollaro, D., Skubis, S., and Dickinson, M. (2000). Origins and mechanisms of eastern Pacific tropical cyclogenesis: A case study. *Mon. Wea. Rev.*, 128(1):125–139.

Moore, R. W. and Montgomery, M. T. (2005). Analysis of an idealized, three-dimensional diabatic Rossby vortex: A coherent structure of the moist baroclinic atmosphere. *J. Atmos. Sci.*, 62(8):2703–2725.

Norquist, D. C., Recker, E. E., and Reed, R. J. (1977). The Energetics of African Wave Disturbances as observed During Phase III of GATE. *Mon. Wea. Rev.*, 105:334–342.

Parker, D. J. and Thorpe, A. J. (1995). Conditional convective heating in a baroclinic atmosphere: A model of convective frontogenesis. *J. Atmos. Sci.*, 52(10):1699–1711.

Parker, M. D. (2010). Relationship between system slope and updraft intensity in squall lines. *Mon. Wea. Rev.*, 138(9):3572–3578.

Pasch, Penny, and Berg (cited 2018). National Hurricane Center Tropical Cyclone Report: Hurricane Maria. [Available online at https://www.nhc.noaa.gov/data/tcr/AL152017_-Maria.pdf].

Payne, S. W. and McGarry, M. M. (1977). The Relationship of Satellite Inferred Convective Activity to Easterly Waves Over West Africa and the Adjacent Ocean During Phase III of GATE. *Mon. Wea. Rev.*, 105:413–420.

Pearson, K., Lister, G., Birch, C., Allan, R., Hogan, R., and Woolnough, S. (2014). Modelling the diurnal cycle of tropical convection across the grey zone. *Quart. J. Roy. Meteor. Soc.*, 140(679):491–499.

Poan, D. E., Lafore, J.-P., Roehrig, R., and Couvreux, F. (2014). Internal processes within the African Easterly Wave system. *Quart. J. Roy. Meteor. Soc.*

Price, E., Mielikainen, J., Huang, M., Huang, B., Huang, H.-L. A., and Lee, T. (2014). GPU-accelerated longwave radiation scheme of the Rapid Radiative Transfer Model for General Circulation Models (RRTMG). *IEEE Journal of Selected Topics in Applied Earth Observations and Remote Sensing*, 7(8):3660–3667.

Raymond, D. J. and Jiang, H. (1990). A theory for long-lived mesoscale convective systems. *J. Atmos. Sci.*, 47(24):3067–3077.

Reed, R. J., Norquist, D. C., and Recker, E. E. (1977). The Structure and Properties of African Wave Disturbances as Observed During Phase III of GATE. *Mon. Wea. Rev.*, 105:317–333.

Rotunno, R., Klemp, J. B., and Weisman, M. L. (1988). A theory for strong, long-lived squall lines. *J. Atmos. Sci.*, 45(3):463–485.

Russell, J. O., Aiyyer, A., White, J. D., and Hannah, W. (2017). Revisiting the connection between African Easterly Waves and Atlantic tropical cyclogenesis. *Geophys. Res. Lett.*

Saha, S., Moorthi, S., Pan, H.-L., Wu, X., Wang, J., Nadiga, S., Tripp, P., Kistler, R., Woollen, J., Behringer, D., et al. (2010). The NCEP climate forecast system reanalysis. *Bull. Amer. Meteor. Soc.*, 91(8):1015–1058.

Schumacher, C., Zhang, M. H., and Ciesielski, P. E. (2007). Heating structures of the TRMM field campaigns. *J. Atmos. Sci.*, 64(7):2593–2610.

Schwendike, J. and Jones, S. C. (2010). Convection in an African Easterly Wave over West Africa and the eastern Atlantic: A model case study of Helene (2006). *Quart. J. Roy. Meteor. Soc.*, 136:364–396.

Shapiro, L. J. (1978). The vorticity budget of a composite African tropical wave disturbance. *Mon. Wea. Rev.*, 106(6):806–817.

Shih, N. (2012). Formation and Development of Diabatic Rossby Vortices in a 10-year Climatology. Master's thesis, Naval Postgraduate School. [Available online at: https://calhoun.nps.edu/handle/10945/7415].

Shin, H. H. and Hong, S.-Y. (2015). Representation of the subgrid-scale turbulent transport in convective boundary layers at gray-zone resolutions. *Monthly Weather Review*, 143(1):250–271.

Skamarock, W. C., Klemp, J. B., Dudhia, J., Gill, D. O., Barker, D. M., Wang, W., and Powers, J. G. (2005). A description of the advanced research WRF version 2. Technical report, National Center For Atmospheric Research, Boulder, CO, Mesoscale and Microscale Meteorology Div.

Skamarock, W. C., Weisman, M. L., and Klemp, J. B. (1994). Three-dimensional evolution of simulated long-lived squall lines. *J. Atmos. Sci.*, 51(17):2563–2584.

Skinner, C. B. and Diffenbaugh, N. S. (2013). The contribution of African easterly waves to monsoon precipitation in the CMIP3 ensemble. *J. Geophys. Res.*, 118(9):3590–3609.

Snyder, C. and Lindzen, R. S. (1991). Quasi-geostrophic wave-CISK in an unbounded baroclinic shear. *J. Atmos. Sci.*, 48(1):76–86.

Thorncroft, C. and Hodges, K. (2001). African Easterly Wave Variability and its Relationship to Atlantic Tropical Cyclone Activity. *J. Climate*, 14:1166–1179.

Thorncroft, C. and Hoskins, B. (1994). An idealized study of African easterly waves. I: A linear view. *Quart. J. Roy. Meteor. Soc.*, 120(518):953–982.

Tiedtke, M. (1989). A comprehensive mass flux scheme for cumulus parameterization in large-scale models. *Mon. Wea. Rev.*, 117(8):1779–1800.

Tomassini, L., Parker, D. J., Stirling, A., Bain, C., Senior, C., and Milton, S. (2017). The interaction between moist diabatic processes and the atmospheric circulation in African Easterly Wave propagation. *Quart. J. Roy. Meteor. Soc.*, 143(709):3207–3227.

Tory, K. J., Kepert, J., Sippel, J., and Nguyen, C. (2012). On the use of potential vorticity tendency equations for diagnosing atmospheric dynamics in numerical models. *J. Atmos. Sci.*, 69(3):942–960.

Vallis, G. K. (2006). *Atmospheric and oceanic fluid dynamics: Fundamentals and large-scale circulation*. Cambridge University Press.

Velasco, I. and Fritsch, J. M. (1987). Mesoscale convective complexes in the americas. *J. Atmos. Sci.*, 92(D8):9591–9613.

Weisman, M. L. and Rotunno, R. (2004). "A theory for strong long-lived squall lines" revisited. *J. Atmos. Sci.*, 61(4):361–382.

Weisman, M. L., Skamarock, W. C., and Klemp, J. B. (1997). The resolution dependence of explicitly modeled convective systems. *Mon. Wea. Rev.*, 125(4):527–548.

Wheeler, M. and Kiladis, G. N. (1999). Convectively coupled equatorial waves: Analysis of clouds and temperature in the wavenumber–frequency domain. *J. Atmos. Sci.*, 56(3):374–399.

Yanai, M., Esbensen, S., and Chu, J.-H. (1973). Determination of bulk properties of tropical cloud clusters from large-scale heat and moisture budgets. *J. Atmos. Sci.*, 30(4):611–627.

Zawislak, J. and Zipser, E. J. (2010). Observations of seven African easterly waves in the east Atlantic during 2006. *J. Atmos. Sci.*, 67(1):26–43.

Zhang, C., Wang, Y., and Hamilton, K. (2011). Improved representation of boundary layer clouds over the southeast Pacific in ARW-WRF using a modified Tiedtke cumulus parameterization scheme. *Mon. Wea. Rev.*, 139(11):3489–3513.

APPENDICES

APPENDIX

A

ACRONYMS

A summary of all acronyms is documented in Table A.1.

Table A.1: A summary of acronyms used in alphabetical order.

Acronym	Abbreviation
African Easterly Wave	AEW
African Easterly Jet	AEJ
African Monsoon Multidisciplinary Analysis	AMMA
Climate Forecasting System Reanalysis	CFSR
Contribution Fraction	CF
Contribution Number	CN
Convective Available Potential Energy	CAPE
Convectively Coupled Equatorial Waves	CCEW
Convective Inhibition	CIN
Convective Initiation	CI
Control	CTRL
Diabatic Rossby Wave	DRW
Diabatic Rossby Vortex	DRV

Dry Adiabatic Lapse Rate	DALR
European Centre for Medium Range Weather Forecasting	ECMWF
Eddy Kinetic Energy	EKE
ERA-Interim Reanalysis	ERAI
GARP Atlantic Tropical Experiment	GATE
Genesis Fraction	GF
Global Forecast System	GFS
Genesis Number	GN
Global Precipitation Mission	GPM
Half mixing ratio	HLFM
July, August, and September	JAS
Land Surface Model	LSM
Level of Free Convection	LFC
Lifting Condensation Level	LCL
Long Wave (Radiation)	LW
Maximum CAPE	MCAPE
Maximum CIN	MCIN
Mesoscale Convective System	MCS
Moist Adiabatic Lapse Rate	MALR
Moist Static Energy	MSE
National Aeronautical and Space Administration	NASA
National Center for Atmospheric Research	NCAR
National Center for Environmental Prediction	NCEP
National Hurricane Center	NHC
National Science Foundation	NSF
No Microphysics Heating	NOMH
Outgoing Longwave Radiation	OLR
Planetary Boundary Layer	PBL
Potential Vorticity	PV
Potential Vorticity Units	PVU
Precipitation	PCP
Rapid Radiative Transfer Model	RRTM
Saharan Air Layer	SAL
Short Wave (Radiation)	SW
Quasi-Geostrophic	QG

Quasi-Linear Convective System	QLCS
Rotunno et al. (1988)	RKW
Rossby Wave	RW
Tropical Cyclone	TC
TRMM Multi-Satellite Precipitation Analysis	TMPA
Tropical Rainfall Measurement Mission	TRMM
WRF Double Moment 6-Class Microphysics	WDM6
West African Monsoon	WAM
Weather Research and Forecasting Model	WRF
Weak Temperature Gradient	WTG

APPENDIX

B

VARIABLES

A summary of all variables is documented in Table B.1.

Table B.1: A summary of all variables and their abbreviations in alphabetical order.

Variable	Abbreviation
Arbitrary variable	X
Absolute vorticity vector	$\vec{\eta}$
Coriolis parameter	f
Diabatic heat	J
Diabatic heating rate	Q
Explicit diabatic heating	H
Explicit latent and convective heating	H_L
Explicit radiative heating	H_R
Explicit boundary layer heating	H_B
Frictional torque in meridional direction	F_y
Frictional torque in zonal direction	F_x
Frictional torque vector	$\vec{F}$
Gas constant for dry air	R

Geopotential	Φ
Geopotential height	Z
Generic PV source	Y
Gravitational accelleration	g
Horizontal wind vector	$\vec{V}$
Isobaric vertical motion	ω
Latent heat of vaporization	l_v
Meridional unit vector	$\hat{j}$
Meridional wind	v
Moist Static Energy	h
Potential temperature	θ
Potential vorticity	P
Pressure	p
Reference pressure (1000 hPa)	p_0
Relative vorticity vector	$\vec{\zeta}$
Shear vector (in isobaric coordinates)	$\vec{S}$
Specific density	α
Specific heat capacity at constant pressure	c_p
Specific humidity	q
Temperature	T
Time	t
Thermodynamic residual	Q_1
Three-dimensional wind vector	$\vec{U}$
Vertical absolute vorticity	η
Vertical unit vector	$\hat{k}$
Vertical relative vorticity	ζ
Zonal unit vector	$\hat{i}$
Zonal wind	u